

A SIMPLE PARAMETERIZATION COUPLING THE CONVECTIVE DAYTIME BOUNDARY
LAYER AND FAIR-WEATHER CUMULI

by

LARRY KEITH BERG

B.Sc., The Pennsylvania State University, 1993

M.Sc., The University of British Columbia, 1996

A THESIS SUBMITTED IN PARTIAL FULFILMENT OF
THE REQUIREMENTS FOR THE DEGREE OF

DOCTOR OF PHILOSOPHY

in

THE FACULTY OF GRADUATE STUDIES

Department of Earth and Ocean Sciences; Atmospheric Science Programme

We accept this thesis as conforming
to the required standard

THE UNIVERSITY OF BRITISH COLUMBIA

July 2002

© Larry Keith Berg

In presenting this thesis in partial fulfilment of the requirements for an advanced degree at the University of British Columbia, I agree that the Library shall make it freely available for reference and study. I further agree that permission for extensive copying of this thesis for scholarly purposes may be granted by the head of my department or by his or her representatives. It is understood that copying or publication of this thesis for financial gain shall not be allowed without my written permission.

Department of Earth & Ocean Science

The University of British Columbia
Vancouver, Canada

Date July, 19, 2002

Abstract

A new field experiment, named Boundary Layer Experiment 1996 (BLX96), was conducted to determine the formation of boundary-layer cumuli clouds over heterogeneous land surfaces. The resulting potential temperature (θ) and water-vapor mixing ratio (r) observations were compiled into Joint Frequency Distributions (JFDs) that represent the source region from which air rises up as thermals to form cumuli.

In order to predict sub-grid boundary-layer cumuli in a climate model, the JFD must be parameterized. Two classical methods to describe JFDs, one based on a statistical fit and another based on surface-layer processes, were found to be inadequate. A new method is devised, where boundary-layer air is divided into one of three groups: updrafts, downdrafts and environment. Separate JFDs are fit to each group and these sub-JFDs are added together to represent the boundary-layer JFD. This method did a good job representing the observed JFDs, but requires many free parameters. A second new method, which needs fewer free parameters, treats the JFD as a mixing diagram. In the absence of advection, the only source regions for air in the mixing diagram are the surface and the entrainment zone. Thus, the tilt of the JFD is caused by various mixtures from these two source regions.

The parameterized JFDs can be used with the mean temperature and humidity profile to predict the amount and size distribution of boundary-layer cloud cover. The result is named the Cumulus Potential (CuP) Model. This model considers the diversity of air parcels over a heterogeneous surface, and recognizes that some parcels indeed rise to their lifting condensation level, while others might rise as non-cloud updrafts. This model has several unique features: (1) cloud cover is determined from the boundary-layer JFD of θ vs. r , (2) cloud-base mass flux can be approximated from the mixed-layer JFD, (3) clear and cloudy thermals are allowed to exist at the same altitude, and (4) a range of cloud-base heights, cloud-top heights, and cloud thicknesses are predicted within any one cloud field, as observed.

Using data from BLX96, and a model intercomparison study using Large Eddy Simulation (LES) based on BOMEX, it is shown that the CuP model does a good job predicting cloud-base height and cloud-top height. The model also shows promise in predicting cloud cover, and is found to give better cloud-cover estimates than three classic cumulus parameterizations: one based on relative humidity, the classic statistical scheme proposed by Sommeria and Deardorff (1977), and a slab model proposed by Albrecht (1981).

Table of Contents

Abstract	ii
Table of Contents.....	iv
List of Tables.....	vi
List of Figures.....	vii
List of Symbols and Acronyms	ix
Preface.....	xiv
Acknowledgements.....	xv
Chapter 1 Introduction	1
Chapter 2 Boundary Layer Experiment 1996.....	4
2.1 Introduction and Motivation for a New Field Experiment	4
2.2 Boundary Layer Experiment 1996	4
2.3 Data Processing	9
2.4 An Investigation Into Some Suspect Flux Values.....	13
2.5 Net Data Available	18
Chapter 3 A New Moisture Scale for Convective Boundary Layers.....	22
3.1 Introduction	22
3.2 A New Scaling.....	25
3.4 Conclusions	26
Chapter 4 Properties of Coherent Drafts Observed During BLX96.....	28
4.1 Introduction	28
4.2 Fractional Coverage of Drafts	28
4.3 Updraft and Downdraft Properties	31
4.4 Comments on Convective Mass-Flux Parameterizations	32
4.5 Conclusions.....	34
Chapter 5 Observations and Models of Joint Frequency Distributions in the Daytime Convective Boundary Layer.....	36
5.1 Introduction	35
5.2 Definitions.....	37
5.3 Observations.....	38
5.4 Classical Methods.....	41
5.5 Two New Methods	44
5.6 Results.....	55
5.7 Conclusions	61
Chapter 6 Parameterization of JFDs of Potential Temperature and Water-Vapor Mixing Ratio.....	63
6.1 Introduction	63
6.2 Parameterization of JFD Tilt.....	65
6.3 Parameterization of JFD Spread.....	68
6.4 Verification Against Independent data	74
6.5 Conclusions and Recommendations.....	78
Chapter 7 Accuracy of Point and Line Measures of Boundary Layer Cloud Amount.....	79
7.1 Introduction and Motivation	79
7.2 Earth-Cover Observation Methods.....	81
7.3 Simulated Cloud Field Results and Applications.....	85
7.4 Observed BLX96 Results	92

	7.5	Conclusions	95
Chapter 8		A New Fair-Weather Cumuli Parameterization.	97
	8.1	Introduction	97
	8.2	An Overview of Cloud Entrainment and Detrainment Rates	100
	8.3	A new scheme: The cumuli potential model.....	102
	8.4	Calibration of Entrainment and Detrainment rates against BOMEX.....	110
	8.5	Alternate Methods of Predicting Cloud Cover.....	114
	8.6	Results of the CuP Model for BLX96.	115
	8.7	Conclusions	124
Chapter 9		Conclusions and Future Work	126
	9.1	Summary of Goals, Methods, and Findings.....	126
	9.2	Future Work	128
References		132
Appendix A		General Statistics for BLX96	147
Appendix B		BLX96 Sample Data.....	151
Appendix C		Slopes Used in the $B-\theta_f$ Method.....	153
Appendix D		Integration of c vs. m Distributions in θ vs. r Space	156
Appendix E		Correlation Introduced by Coordinate Transformation	160
Appendix F		BLX96 Cloud Field Statistics.....	162
Appendix G		Conditions Used for BOMEX Case.....	165

List of Tables

2.1	List of indicator variables used in different field studies	14
2.2	List of BLX96 case study days	19
5.1	Case, date, time, height, observed $\rho_{\theta,r}$ and predicted $\rho_{\theta,r}$ for the case study days were the observed $\rho_{\theta,r}$ and predicted $\rho_{\theta,r}$ were of different sign	61
6.1	Methods used to parameterize JFDs, the variables needed for the parameterization	64
6.2	Calibration subset of BLX96 case-study days	68
6.3	Verification subset of BLX96 case-study days	74
A.1	General Statistics for BLX96 General Statistics	147
F.1	Observed date, time, solar zenith angle, cloud base height, cloud top height, and boundary-layer cloud type	162
G.1	Mean environment profiles of p , θ_v , and r	166
G.2	Miscellaneous values used for the CuP simulation the BOMEX case	166

List of Figures

1.1	Sketch showing the relationships of different parts of this dissertation.....	2
2.1	ARM SGP CART location within North America	6
2.2	First half of the standard BLX96 flight pattern.....	7
2.3	Histogram of observed Bowen Ratio vs. count.....	15
2.4	Contours of 24 hour accumulated precipitation.....	18
3.1	Plot showing σ/r_* vs. z/z_i	27
4.1	Updraft or downdraft fraction vs. threshold multiplier	30
4.2	Fraction of the BLX96 flight legs covered by updrafts and downdrafts.....	30
4.3	Plot showing $\delta r_u/r_{*,new}$ and $\delta r_d/r_{*,new}$ vs. z/z_i	32
4.4	BLX96 mass-flux predicted flux vs. observed flux	33
4.5	Normalized mass-flux error vs. z/z_i	34
5.1	Correlation of θ and r for BLX96 flight legs vs. z/z_i	39
5.2	Sequence of three JFDs of θ vs. r at three different heights.....	40
5.3	Observed JFD and sample fits of the statistical method and the $B-\theta_F$ method.....	42
5.4	Maximum likelihood B axis slope vs. SSZ theoretical B axes slope and maximum likelihood θ_F axis slope vs. SSZ theoretical θ_F axis slope vs. for all BLX96 legs.....	43
5.5	Maximum likelihood B axis slope and maximum likelihood θ_F axis slope vs. observed surface B for all BLX96 near surface legs.....	44
5.6	Sketch showing parcel families.....	45
5.7	Plot showing updraft, downdraft and environment θ vs. r	46
5.8	Slope of the line through the updraft and the leg mean vs. slope of the line through the mean of the updraft and downdraft.....	47
5.9	Plot of f_u and f_d vs. z/z_i for all BLX96 case study days.....	48
5.10	Mixing diagrams for the three sequential soundings on 15 July.....	50
5.11	θ vs. r mixing diagram.....	51
5.12	Sequence of three JFDs of c vs. m at three different heights	53
5.13	Sketch of a case where the JFD is uncorrelated in θ vs. r but is correlated in c vs. m space because of the larger area contributing positive values	54
5.14	Sketch of two cases where a JFD is correlated in θ vs. r space, but is not correlated in c vs. m space, perfect fit and orthogonal surface and entrainment zone axes.....	54
5.15	Plot of observed and predicted JFDs.....	57
5.16	Error associated with a statistical fit with no tilt, error associated with the $B-\theta_F$ method, error associated with the sub-JFD method, and error associated with the surface-entrainment zone method vs. error associated with the statistical fit	58
5.17	Best-fit $\rho_{\theta,r}$ vs. observed $\rho_{\theta,r}$ for all BLX96 flight legs.....	59
5.18	Observed JFDs and best-fit surface-entrainment zone JFDs for the five cases where the observed $\rho_{\theta,r}$ had an opposite sign than the $\rho_{\theta,r}$ best-fit	60
6.1	Predicted surface axis inverse slope vs. observed surface axis inverse slope	67
6.2	Sorbjan's expression for σ_θ/θ_* and observed values of σ_θ/θ_* vs. z/z_i	69
6.3	Sorbjan's expression for $\sigma/r_{*,new}$ BLX96 data vs. z/z_i	70
6.4	The value of $\rho_{\theta,r}$ measured over the ocean during BLX96	71
6.5	Observed values σ_θ/θ_* , $\sigma/r_{*,new}$, and best-fit curves	72
6.6	Observed σ_c/θ_* and σ_m/θ_* on the BLX96 case study days	73

6.7	Observed and parameterized JFDs using Gaussian, $B-\theta_F$ and mixing diagram methods.....	75	
6.8	Errors associated with either the mixing-diagram method or $B-\theta_F$ vs. errors associated with the parameterized statistical JFD.....	76	
6.9	Mixing-diagram error range vs. statistical error range.....	78	
7.1	Sketch showing cloud geometry used to estimate the earth-cover error.....	83	
7.2	Earth cover fractional error vs. solar zenith angle.....	86	
7.3	Mean line sampled earth cover vs. true simulated earth cover.....	87	
7.4	Leg-to-leg standard deviation of the observed earth cover vs. leg length.....	87	
7.5	Simulated line-sampled vs. simulated swath-sampled earth cover.....	88	
7.6	Leg-to-leg standard deviation of sample earth cover vs. true earth cover.....	89	
7.7	Human-observed vs. pyranometer-observed earth-cover fraction for all BLX96 cloudy legs.....	93	
8.1	Sketch of a group of near-surface boundary-layer parcels.....	104	
8.2	Observed θ_v and z_{LCL} for individual parcels along with the mean profile.....	105	
8.3	Plot similar to 8.2, but with only a single parcel from sector 2 and a single parcel from sector 3.....	107	
8.4	Profiles of θ and r observed during BOMEX.....	110	
8.5	Parameterized JFD for the BOMEX case.....	111	
8.6	Total updraft fraction, cloudy updraft fraction and clear updraft fraction predicted by the CuP model for BOMEX.....	112	
8.7	Plot of θ_v vs. height and r vs. height for BOMEX.....	113	
8.8	Plot of the CuP predicted mode cloud-base height vs. observed cloud-base height.....	117	
8.9	Plot of CuP, Roeckner et al., Sommeria and Deardorff, and Albrecht predicted cloud-base height. vs. observed cloud-base height.....	118	
8.10	Plot of CuP, Roeckner et al., Sommeria and Deardorff, and Albrecht predicted cloud-top height vs. observed cloud-top height.....	118	
8.11	Total, cloudy and clear draft fraction vs. height for 27 July.....	120	
8.12	Cloudy draft fraction vs. height for 27 July.....	121	
8.13	Predicted cloud-cover fraction for all BLX96 case study days using the methods		of .
8.14	CuP predicted cloud-cover fraction vs. observed cloud-cover.....	123	
9.1	Sample θ distributions after mixing.....	129	
B.1	BLX96 sample profiles.....	151	
B.2	BLX96 sample time series.....	152	
C.1	After Schrieber et al. showing B and θ_F	154	
D.1	Sketch showing the coordinate transform converting a point (θ,r) to (c,m)	157	
D.2	Sketch showing some arbitrary shaded area in θ vs. r space.....	159	

List of Symbols and Acronyms

α_3	Fraction of parcels in sector 3 of the JFD
α_{cloud}	Cloud cover fraction
α_u	Fraction of boundary layer covered by updrafts
α_d	Fraction of boundary layer covered by downdrafts
δ	Detrainment rate
$\overline{\delta\psi_u}$	Difference between leg average ψ and updraft average ψ
$\overline{\delta\psi_d}$	Difference between leg average ψ and downdraft average ψ
ε	Entrainment rate
ϕ	Solar zenith angle
γ	Slope of JFD axes
θ	Potential temperature
θ_e	Equivalent potential temperature
θ_v	Virtual potential temperature
$\hat{\theta}$	Arbitrary observation of θ
θ_F	Solar forcing
θ_*	Temperature scale
ρ_{air}	Density of air
ρ_d	Density of downdrafts
ρ_u	Density of updrafts
$\rho_{\theta,r}$	Correlation between θ and r
$\sigma_{\pm\psi}^2$	Variance ψ calculated using only points greater than or less than the mean
σ_{ψ}^2	Variance of ψ
σ_{sfc}	Standard deviation along surface axis
σ_{ez}	Standard deviation along the EZ axis
σ_B	Standard deviation along B axis

σ_{θ_F}	Standard deviation along θ_F axis
σ_{cloud}	Standard deviation of cloud cover
ω	Mass flux convective velocity scale
ψ	An arbitrary variable
ψ_*	An arbitrary scale
ψ_{thresh}	Threshold value of an arbitrary variable
ψ_T	Updraft average ψ
ψ_{env}	Environment average ψ_{env}
$\bar{\psi}$	Time average value of ψ
A	Area covered by cloud shadow
AGL	Above ground level
AMTEX	Air Mass Transform Experiment
ASOS	Automated Surface Observing System
ARM	Atmospheric Radiation Measurement
B	Surface Bowen ratio
B_{sfc}	Surface Bowen ratio
B_z	Height dependant Bowen ratio
BLX96	Boundary Layer Experiment 1996
BOMEX	Barbados Oceanographic and Meteorological Experiment
c	Location in transformed coordinate space
c_2	Arbitrary constant
c_5	Arbitrary constant
C_p	Specific heat of dry air
CAPE	Convective Available Potential Energy
CART	Clouds and Radiation Testbed
Cb	Cumulonimbus

CuP	Cumulus Potential
D	Ratio of entrainment zone depth to z_i
DFT	Discrete Fourier transform
err_{flux}	Flux error
ER	Error range
EZ	Entrainment zone
f	An arbitrary function
\hat{f}	Observed or predicted frequency in a single JFD bin
\tilde{f}	Fraction of leg mean value contributed by updraft or downdraft air
FAA	Federal Aviation Administration
FFT	Fast Fourier transform
g	Acceleration due to gravity
HAPEX	Hydrologic-Atmospheric Pilot Experiment
JFD	Joint Frequency Distribution
l	Averaging length
L_v	Latent heat of vaporization
LES	Large Eddy Simulation
LNB	Level of neutral buoyancy
m	Location in transformed coordinate space
M_c	Cloud mass flux
MCC	Mesoscale Convective Complex
MSL	Mean Sea Level
m	Cloud mass
NEXRAD	Next Generation Radar
NOAA	National Oceanic and Atmospheric Administration
NSR	Noise to signal ratio

NWS	National Weather Service
p	Pressure
Q^*	Total net-flux
r	Water-vapor mixing ratio
\hat{r}	Arbitrary observation of r
r_{LCL}	Mixing ratio at lifting condensation level
r_s	Saturation mixing ratio
r_*	Moisture scale
$r_{*,new}$	A new moisture scale
R_ψ	Ball ratio of entrainment flux of ψ to surface flux of ψ
RH	Relative humidity
RMSE	Root Mean Squared Error
s	Normalized saturation deficit
sfc	Surface
SGP	Southern Great Plains
T	Temperature
T_v	Virtual temperature
t_*	Boundary layer time scale
UTC	Coordinated Universal Time
U	Horizontal wind speed
w	Vertical velocity
w_T	Turbulent transport velocity
w_*	Deardorff convective velocity scale
$w_{*,cloud}$	Velocity scale for clouds
w_{cloud}	Cloud updraft velocity
w_{thresh}	Threshold vertical velocity
$\overline{w\theta_v}_{sfc}$	Surface flux of θ_v

:

$\overline{w \psi}_{mf}$	Flux of ψ predicted by the mass-flux approximation
x_{offset}	Distance that horizontal flight legs were offset downwind from near surface leg
x_c	One-half cloud width
x_{tan}	Location where the sun's ray is tangent to cloud top
z	Height above ground
z_c	Cloud thickness
z_{LCL}	Lifting condensation level
z_i	Mixed layer depth
z_{tan}	Location where the sun's ray is tangent to cloud top

Acknowledgements

A number of individuals have played an important role in this dissertation. Prof. Roland Stull contributed an endless supply of both ideas and support for this work. In addition to his role as my advisor, he helped plan BLX96 and worked as one of the airborne scientists. Dr. Edi Santoso was a valuable sounding board for ideas, helped plan BLX96, served as an airborne scientist, and helped with data processing. Dr. Joshua Hacker served as an airborne scientist and was the lead weather forecaster during BLX96. Henryk Modzelewski has shared his insight and understanding of boundary-layer processes, as well as serving as computer guru. The staff and flight crew of the University of Wyoming King Air aircraft (sponsored by NSF) helped to make BLX96 a success. Profs. Philip Austin and Andy Black served on my supervisory committee, and their comments have greatly improved this dissertation. In addition to these individuals, my wife Jill has shown great patience and support throughout this process.

The University of British Columbia provided support through a University Graduate Fellowship. A number of government agencies have also supported this work. The BLX96 field program was funded by the National Science Foundation under Grant ATM-9411467. The Canadian Climate Research Network provided support through grants from the National Science and Engineering Research Council (NSERC), Meteorological Service of Canada, and the Canadian Foundation for Climate and Atmospheric Science. Additional support was provided by the Geophysical Disaster Computational Fluid Dynamics Centre, and grants from NSERC and Environment Canada.

Output from the Rapid Update Cycle Model was provided by the United States Department of Energy, Atmospheric Radiation Measurement program. Precipitation estimates from the NEXRAD network were provided by the Arkansas Red River Basin River Forecast Center.

Chapter 1: Introduction and Motivation

Fair-weather cumuli may seem to be a benign presence at the top of the convective boundary layer. However in certain instances these relatively small, innocuous clouds play an important role. They form a turbulent conduit allowing boundary-layer heat, moisture, momentum and pollutants to be transported to the free atmosphere. Clouds reduce the shortwave radiation absorbed at the surface under cloud shadows, but increase it elsewhere due to scattering of shortwave radiation off the sides of the clouds. Fair-weather cumuli have little effect on the longwave energy budget because they form relatively close to the surface and their temperature is close to the surface temperature. Both the transport out of the boundary layer, and changes in the surface energy budget influences daily growth and behavior of the convective boundary layer. Over longer time periods, these over land clouds reduce the amount of net radiation reaching the surface because the clouds over land exist during daylight but disappear at night. Over water, the clouds reduce the amount of net radiation reaching the surface during the day, but they persist during the night and increase the amount of net radiation at the surface

Ever since the first numerical weather prediction models were conceived in the early 1920s (Richardson 1922), the parameterization of subgrid scale processes, such as clouds, complex terrain, and turbulence has been an important issue. Unfortunately, these issues remain unresolved today. Historically, most cumuli parameterizations have not included fair-weather cumuli over land, but have focused on either deeper precipitating cumuli or maritime stratocumuli over a homogeneous surface. Recent efforts, such as those by Lappen and Randall (2001), attempt to couple the formation of cumuli to boundary-layer turbulence. Such an approach seems logical because the roots of the cumuli, even very deep precipitating cumuli are in the boundary layer (Pennell and LeMone 1974).

In this dissertation a simple parameterization to predict boundary-layer cumuli over a heterogeneous land surface is developed for climate and forecast models (Figure 1.1). The parameterization has two modules: one representing boundary-layer turbulence and surface

heterogeneity using Joint Frequency Distributions (JFDs) of potential temperature (θ) vs. water-vapor mixing ratio (r), the other module is a cloud model which represents cloud processes

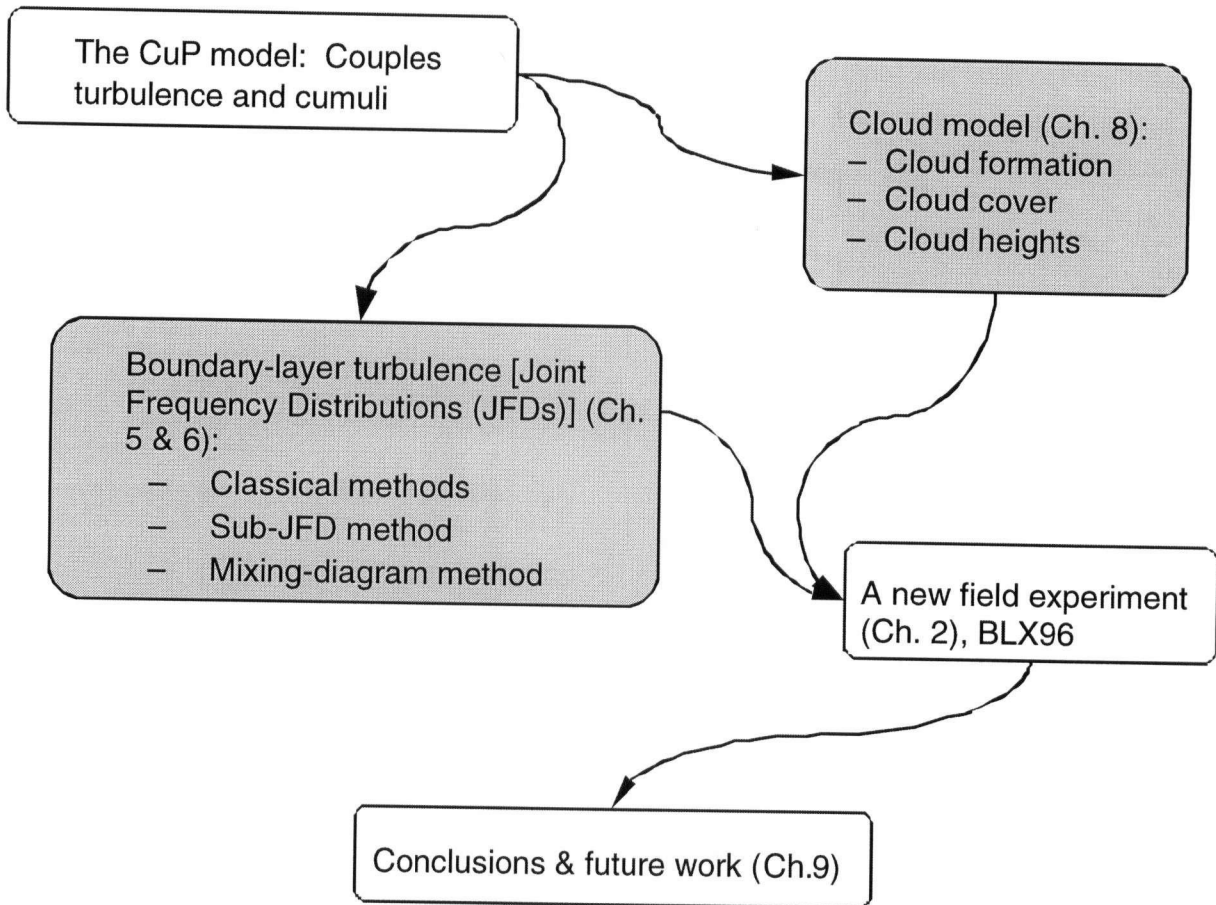


Figure 1.1. Sketch showing the relationships of different parts of this dissertation. See text for detailed description of the contents of each Chapter.

As part of this research a new field program, called Boundary Layer Experiment 1996 (BLX96), was conducted to measure JFDs over three different sites, as described in Chapter 2. Results from the field program suggested some shortcomings in typical boundary-layer scales; therefore, in Chapter 3 a new moisture scale is introduced. Detailed analysis of some of the findings from BLX96, to be used to develop parameterizations in later chapters, are shown in Chapter 4. Observed JFDs of θ vs. r will be presented in Chapter 5, and two new physically

based methods to describe JFDs will be introduced and compared to two classical methods to represent the JFDs. Parameterizations of JFDs will be developed in Chapter 6 to allow JFDs to be created for any time and place. Before estimates of cloud fields are made, the likely errors associated with observed cloud amounts during BLX96 will be presented in Chapter 7. This Chapter has also appeared as Berg and Stull (2002). In Chapter 8, estimates of cloud cover, cloud-base height, and cloud-top height using the new statistical parameterization will be made. These results will also be compared to three classical parameterizations. Finally, some conclusions and ideas for future work will be presented in Chapter 9. Relevant literature will be reviewed in each chapter.

Chapter 2: Boundary Layer Experiment 1996

2.1 Introduction and motivation for a new field experiment

Berg (1997) revealed that a combination of standard in situ surface observations (30 minute averages and standard deviations of temperature, humidity, winds, sensible heat flux, and latent heat flux) along with balloon radiosonde soundings did not provide sufficient data for verification of the first version of the Cumulus Potential (CuP) model. Four shortcomings were identified: (1) sampling problems with radiosonde profiles, (2) problems calculating Joint Frequency Distributions (JFDs) of θ vs. r using data from surface stations, (3) physics of the CuP model, and (4) advection of clouds.

An instrumented aircraft flying through the convective boundary layer is one way to address the first three shortcomings. Aircraft can measure the mixed-layer depth (z_i), dynamic and thermodynamic properties of the mixed layer more accurately than a balloon sounding because many more thermals are encountered by the aircraft. Similarly, JFDs measured using aircraft are more accurate than those measured with a surface sensor, again because more thermals are sampled. The aircraft has the added advantage that it can measure JFDs at a range of heights, so that changes in the JFD with altitude can be investigated.

Prior field experiments could supply data for this study. However, many older studies were either conducted over water, over hilly terrain, or had short flight legs. A new field program, called Boundary Layer Experiment 1996 (BLX96), was already being planned. It was decided that BLX96 could be tailored to gather the data that was required for further development and verification of the CuP model and to continue research into the structure of JFDs.

2.2 Boundary Layer Experiment 1996

Boundary Layer Experiment 1996 (BLX96) was conducted between 15 July and 13 August 1996 over regions of Oklahoma and Kansas USA (Stull et al. 1997; Berg et al. 1997). A total of twelve research flights were flown during BLX96. Each flight started between 10:00 and

10:30 LST, and lasted 4 to 4.5 hours. Solar zenith angles (ϕ) ranged between approximately 15° and 36° and were less than 30° for 80% of the legs flown. Only ten flights were used for this study, one was excluded because the tubing leading to the fast response humidity sensor was not connected during the flight, the other because wind speeds (about 8 m s^{-1}) lead to forced, rather than free convection (Obukhov length of -257.8 m). On 16 July, parts of the pattern were excluded because measured moisture flux was suspect during the third near-surface leg. This leg is discussed in more detail in Section 2.4.

The University of Wyoming King Air aircraft, which was instrumented for turbulence measurements, was the main instrument platform used during BLX96. On the aircraft, most variables were recorded at a rate of 50 Hz. Two different instruments were used to measure humidity: a LI-COR LI 6262 provided fast response measurements, and a Cambridge Chilled Mirror hygrometer (model 137C3) provided more accurate measurements recorded at a rate of 1 Hz. Stull et al. (1997) lists all of the instruments on the King Air during BLX96.

The region used for BLX96 was chosen for several reasons. First, the area is relatively flat, with large areas of homogeneous land use. Second, the US Department of Energy has developed a large instrument network, called the Atmospheric Radiation Measurement (ARM) Southern Great Plains (SGP) Clouds and Radiation Testbed (CART) in parts of north-central Oklahoma and south-central Kansas (Stokes and Schwartz 1994). This site covers an area approximately the size of a global climate model grid box (Figure 2.1). The main purpose of ARM SGP CART is to gather data for development of cloud and radiation parameterizations for use in global climate models. Data gathered is freely available and complements data collected during BLX96. Instruments are scattered throughout ARM SGP CART. At the center of ARM SGP CART, near Lamont Oklahoma, is the central facility that has the most extensive gathering of instruments in the site. Instruments located there include, but are not limited to: 60 m tower, 915 MHz wind profiler, balloon launch station, and Micropulse lidar and Belfort Laser Ceilometer to measure cloud-base height. Additional measurements are made at numerous other locations

scattered across the site.

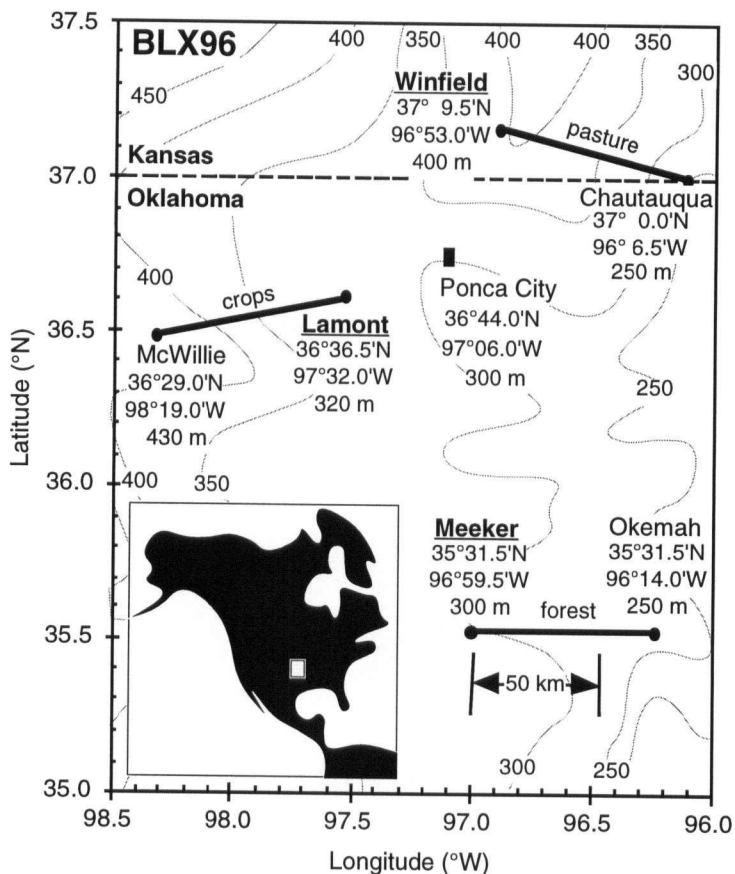


Figure 2.1 ARM SGP CART location within North America (inset) and the locations of each of BLX96 flight tracks. Contour lines mark smoothed height above sea level in 50 m increments.

Three different locations within ARM SGP CART were chosen for BLX96 flights. Each leg was named after a nearby hamlet or town (Figure 2.1). The three legs were chosen to be over regions of different land use and to be close to at least one ARM SGP CART surface station. The Lamont track was over flat terrain devoted to both wheat farming and hay production. Prior to BLX96 the wheat had been cut, and the wheat fields were bare. The ARM SGP CART central facility was located at the east end of this track. The Meeker track had many rolling hills and much forest coverage. The forest was not dense, and most of the trees were less than 10 m high. Some of the land was devoted to agriculture, either crops or hay production. The Winfield leg was over

a region with some gentle rolling hills. Most of the leg was over pasture, but there was some sparse forest near the east end of the track.

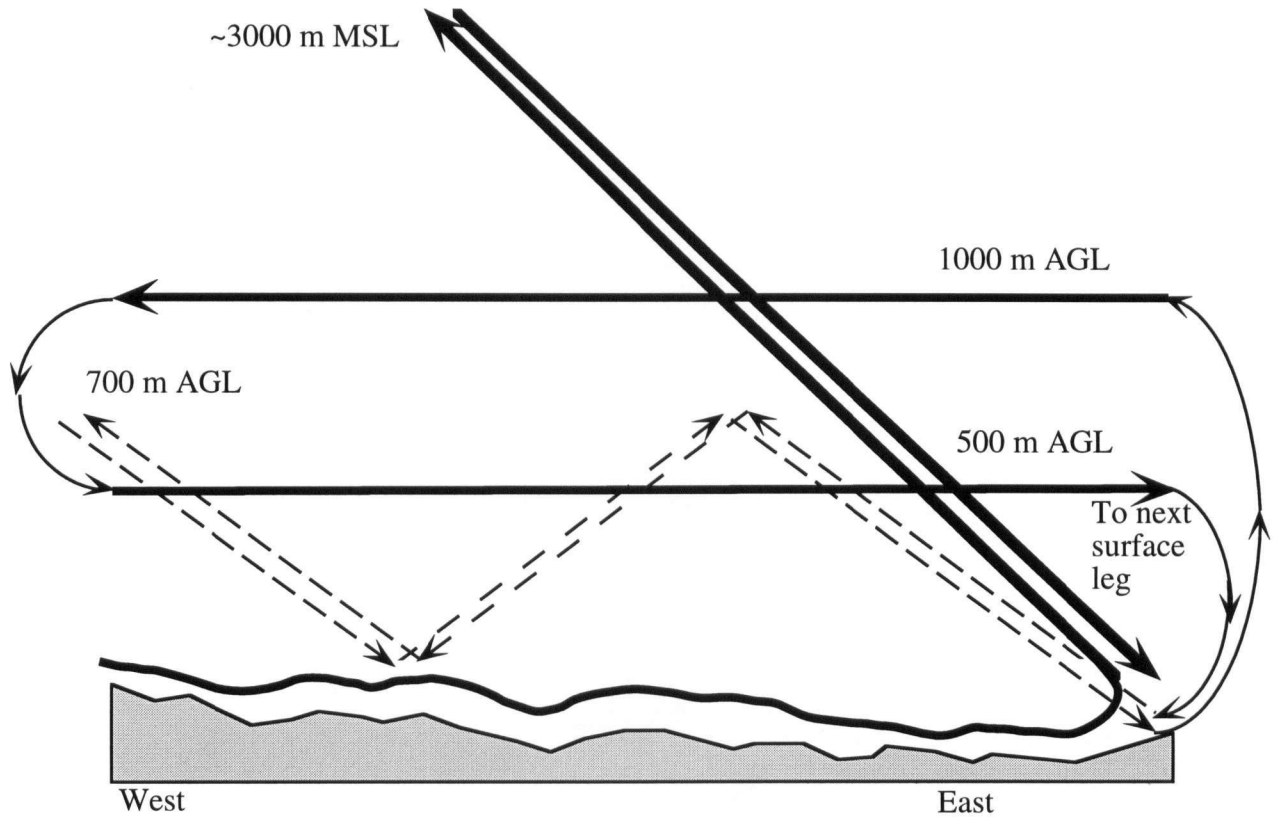


Figure 2.2 First half of the standard BLX96 flight pattern. Heavy lines indicate legs used in this study, thin lines indicate miscellaneous maneuvers, thin broken lines indicate legs used for other experiments. The second half of the pattern is a mirror image of this half, with horizontal legs at 750 and 250 m AGL rather than 1000 m and 500 m AGL.

A unique flight pattern (Stull et al. 1997; Berg et al. 1997) (Figure 2.2) was designed for BLX96 to simultaneously satisfy three different experiments, a radix-layer experiment (Santoso and Stull 1998; Santoso and Stull 2001), a convective transport theory experiment (Stull 1994), and work related to the JFDs and cloud cover presented in this dissertation. In each case, the pattern was oriented approximately perpendicular to the mean boundary-layer wind. For all of the BLX96 flights this resulted in tracks aligned in a nearly east-west direction. Soundings were flown from near the surface to above cloud top three times during each flight: near the start,

middle and end of the pattern. Special zigzag legs were flown for the radix-layer experiment. These legs ranged from near the surface to about 1/3 the boundary-layer depth (z_i) and are not used in this study. Level horizontal legs were flown at a range of heights within the boundary layer. The highest horizontal leg was flown approximately 1000 m Above Ground Level (AGL) or just below cloud base, whichever was lower. Other horizontal legs were flown at approximately 750, 500, and 250 m AGL (Figure 2.2). The aircraft speed during each horizontal leg was about 80 m s⁻¹. During each flight, three approximately-terrain-following near-surface legs were flown 30 to 60 m above the surface. Fluxes measured from these legs were used to compute standard boundary-layer scales. The heights of all legs correspond to heights ranging from about 0.02 to 0.8 z_i . Data from these horizontal legs and the soundings form the basis of the results presented in this dissertation. Samples of data collected from soundings and horizontal legs are shown in Appendix B.

Each horizontal leg was approximately 70 km long in order to yield robust turbulent statistics (Lenschow and Stevens 1980). Each elevated leg was offset downwind from the surface leg in an effort to sample from the same surface-flux footprint with each pass. Combining Weil and Horst's (1992) expression for the dimensionless downwind distance, and their relationship between the measurement height and maximum flux from some source region yields

$$x_{offset} = (0.7\bar{U}z^{2/3}) / \left[(g/\bar{\theta}_v)\overline{w\theta'_{v,sfc}} \right]^{1/3}, \quad (2.1)$$

where x_{offset} is the offset amount, \bar{U} is the average wind speed, z is the height of the flight leg, $\bar{\theta}_v$ is the average virtual potential temperature, g is the acceleration due to gravity, and $\overline{w\theta'_{v,sfc}}$ is the surface virtual heat flux. The offset amount was determined by the airborne scientist during flight based on the estimated surface heat flux, observed boundary-layer wind speed, observed $\bar{\theta}_v$ value, and the height of the flight leg above ground. The surface heat flux was estimated from surface fluxes measured at ARM SGP CART surface stations located near the flight track during the summer of 1995. During the flights, these values were adjusted for time of day and the amount of cloud cover. The boundary-layer wind speed and $\bar{\theta}_v$ were estimated from real-time displays during the slant soundings. In most cases the offset was small, with higher legs offset more than

lower legs. Most legs were flown less than 1 km downwind of the surface leg. The largest offset used during BLX96 was about 3.5 km.

Ideally, more horizontal legs would have been flown, but that was beyond the range of the King Air. We decided that it was better to design one flight pattern that met the requirements of all three experiments and to fly that pattern frequently, rather than design a separate flight pattern for each experiment. Upon reflection, this decision was correct, because it allowed us to sample as many days and locations as possible and avoided problems determining which pattern to fly.

The order of the legs was changed for the flight on 13 August. All of the horizontal legs were flown between the first and second set of soundings. Both zigzag patterns were flown between the second and third soundings. This was done to ensure that the horizontal legs were flown before the onset of cumuli. Ironically, the skies remained clear. A more detailed description of the synoptic weather patterns can be found in Stull et al. (1997) and in Table 2.2.

2.3 Data processing

First, the data were checked for outliers or bad data. Outliers were defined to be more than five standard deviations away from the mean. There were no outliers in the BLX96 data. Bad data were defined as those occasions where aircraft pitch was greater than $\pm 5^\circ$, a change in pitch greater than 2.5° between any two consecutive data points, aircraft roll was greater than $\pm 10^\circ$, or a change in roll of greater than $\pm 5^\circ$ for any consecutive data points.

A Discrete Fourier Transform (DFT) was used to filter the data collected from horizontal legs. A DFT was used, rather than a Fast Fourier Transform (FFT), to eliminate the need for zero padding or truncation of the data from each flight leg. Wavelengths less than approximately 20 m were removed from the data, primarily because the instruments on the aircraft were not co-located. Wavelengths greater than 5 km were removed to eliminate mesoscale effects that might be present. DFTs or FFTs require that all data points be equally spaced and that there are no missing data. Replacing bad data is a challenge. In our case, the points identified as “bad” were not noticeably

different than their neighbors; so they were not removed for the DFT calculations. These points were excluded for all subsequent calculations, for example calculations to determine the eddy-correlation flux or JFDs. To construct JFDs, each observation was placed into a θ vs. r bin 0.1 K by 0.1 g·kg⁻¹ wide.

The slant ascent and descent soundings were processed differently. The first two sets of soundings flown during each day reached from near the surface to above cloud top and then back to the surface. The final sounding of the day was a single sounding flown from near the surface to above cloud top. No descent sounding was flown to conserve flight time. During processing each sounding was reduced to 20 m vertical resolution using block averages. The 20 m block averages from the upward and downward soundings were averaged together to yield the final average sounding.

The mixed-layer depth (z_i) was found visual inspection of the slant soundings. Three different scientists determined their best guess, using profiles of θ_v , r , and/or winds. These three different values were averaged together to yield a best-guess value of z_i (Appendix A and B).

2.3.1 Cloud Observations

One of the goals of BLX96 was to provide data for verification of boundary-layer cumulus parameterizations. Earth cover, the fraction of the Earth's surface covered by clouds as seen from above or below, is a key variable for verification of such parameterizations. Standard surface observations are unsatisfactory because they measure sky cover, the amount of the sky dome covered by clouds, rather than the amount of earth covered. In addition, surface observations would be valid for only a fraction of the flight track. Observations of earth cover by an observer on the ground (either human or electronic) would be unreliable because only one or two clouds might be directly over the observer, leading to a large sampling error. Satellite observations were not used because many of the small boundary-layer cumuli (cumulus humilis) present during BLX96 were smaller than weather-satellite resolutions.

Because of the shortcomings of these methods, two alternative methods for measuring earth cover were used during BLX96: radiometrically and manually. The upward looking Eppley PSP pyranometer on the aircraft showed large differences between measurements made inside and outside cloud shadows. A threshold value of 575 W m^{-2} was applied to the unfiltered pyranometer time series to determine when the aircraft passed through a cloud shadow (Ek and Marht 1991). The estimated earth cover was defined as the fraction of the whole leg that was within cloud shadows. The pyranometer-measured earth cover was insensitive to the threshold chosen, for thresholds between 375 and 775 W m^{-2} .

The airborne scientist on each flight also made estimates of earth cover based on the cloud shadows projected on the ground. Fortunately the area under the flight tracks was divided by roads and fence lines into $800 \times 800 \text{ m}$ ($1/2$ mile \times $1/2$ mile) areas, allowing for more accurate estimates of earth cover. All of the manual estimates for a given flight leg were averaged together to give a leg average. The number of human observations logged during any given leg ranged from one to ten. Four different airborne scientists flew during BLX96. Although all four scientists trained together before the field program in an attempt to equalize their observations, there may be biases in earth-cover estimates. Young (1967) found that differences between observers working with the same satellite images were as large as two-oktas for the range of earth covers he studied. Similar errors might be expected for the observations made during BLX96. The airborne scientists also logged cloud thickness of the cumuli in three ways: (1) estimating aspect ratio (cloud width to cloud height) visually, (2) logging cloud-base and cloud-top altitudes during ascent and descent slant aircraft soundings, and (3) via post-flight inspection of footage from the forward looking automatic airborne video camera.

2.3.2 Identification of coherent drafts

Work presented in the following chapters requires the identification of relatively large coherent updrafts and downdrafts for each horizontal flight leg. Methods, like those proposed by Manton (1977), Coulman (1978), Lenschow and Stephens (1980), Nicholls and LeMone (1980),

Greenhut and Khalsa (1982, 1987), Grossman (1984), Khalsa and Greenhut (1985), Young (1988), Williams and Hacker (1992), Schumann and Moeng (1991), Siebesma and Cuijpers (1995) and Wang and Stevens (2000) were used to identify coherent drafts in the aircraft data. Three different criteria are needed to identify the drafts: an indicator variable to define the thermal, some threshold value of the indicator variable, and some length scale. Unfortunately, all of these criteria are arbitrary. Either w , θ_v , r , or T have been used as the indicator variable (Table 2.1). Crum and Stull (1987) tried to determine which indicator variable works the best. Based on observations of thermals made using a research aircraft and coincident lidar observations over land and near the mixed-layer top, they suggested that r is the best choice to identify thermals. In contrast, Schumann and Moeng (1991) suggested that using w to locate the thermals results in the most consistent results. Siebesma and Cuijpers (1995) used both w and r to define thermals in the cloudy boundary layer. In this study, w will be used as an indicator variable for two reasons: there was less scatter in the thermal statistics when using w rather than r , and because JFDs of θ vs. r for both updrafts and downdrafts will be found in chapter 5. If r were used as the indicator variable, the JFDs of updrafts and downdrafts would have an unrealistic abrupt edge at the threshold value of r , in other words, all of the updrafts would have r greater than the threshold value, and all downdrafts would have r less than the threshold value. Physically, the r distributions of updrafts and downdrafts are expected to be smooth.

One common way to define the threshold is: $\psi_{thresh} = \sqrt{m_{thresh} \sigma_{\pm\psi}^2}$, where m_{thresh} is called the threshold multiplier (dimensionless), ψ is the indicator variable, and $\sigma_{\pm\psi}^2$ is $\sigma_{+\psi}^2$ or $\sigma_{-\psi}^2$. The value of $\sigma_{+\psi}^2$ is the variance of ψ calculated using only the observations of ψ greater than the mean value of ψ , and the value of $\sigma_{-\psi}^2$ is the variance of ψ calculated using only the observations of ψ less than the mean value of ψ . Following the lead of Greenhut and Khalsa (1982), the threshold value in this study was defined as $w_{thresh} = \sqrt{\sigma_{\pm w}^2/2}$. One advantage of this choice of w_{thresh} is that the upward and downward mass flux are approximately the same (Greenhut and Khalsa 1982).

To be called a coherent draft, a structure must be longer than a specified length scale. In addition, if two drafts are separated by a distance less than the length scale, they are assumed to be one structure. Coulman (1978) used a length scale of zero, where his only criterion was the T threshold. Some authors (Greenhut and Khalsa 1982, 1987; Khalsa and Greenhut 1985) used a constant length scale. Young (1988) used a length scale of $0.1 z_i$. He chose this value because, in general, smaller turbulence scales are within the inertial cascade. In our work, we will use a slightly smaller length scale of $0.05 z_i$. A number of BLX96 spectra, particularly near the surface, have a peak very close to $0.1 z_i$, and drop off at shorter scales (Modzelewski, personal communication). Therefore, choosing a cutoff of $0.1 z_i$ might inappropriately remove some of the coherent drafts. Properties of the resulting drafts observed during BLX96 are shown in Chapter 4.

2.4 An investigation into some suspect flux values

A small (in magnitude) negative moisture flux of $-0.00538 \text{ g}\cdot\text{kg}^{-1} \text{ m}\cdot\text{s}^{-1}$ was measured during the last surface leg flown on 16 July (Meeker track, 14:00 LST) (Appendix A). This was unexpected because the moisture flux is generally positive during periods of free convection over land—this was the only negative moisture flux measured during BLX96. The sensible heat flux and the latent heat flux at the surface must balance the net radiation at the surface, therefore a negative moisture flux could be balanced by a large heat flux. But during this leg the observed heat flux was about the same as that observed during legs flown earlier that day; the resulting negative Bowen ratio (B) was the largest magnitude B measured during BLX96 (Figure 2.3).

Table 2.1. List of indicator variables used in different field studies, the physical reasoning behind the choice of the variable, some potential shortfalls associated with that variable, and the researchers that have used that variable.

Indicator Variable	Physical Reasoning	Potential shortfalls	Researchers
w	Direct measure of thermal velocity	Noisy signal	Nicholls & LeMone (1980) ¹ , Greenhut & Khalsa (1982, 1987), Grossman (1984), Khalsa & Greenhut (1985), Young (1988), Siebesma & Cuijpers (1995), Wang & Stevens (2000)
θ_v	Buoyancy is the dominant force driving the thermal.	Other forces and inertia can be important, especially high in the mixed layer where the thermal is often cooler than its surroundings.	Williams & Hacker (1992)
r	Thermals tend to be more moist than the environment	May not always be true over land. r is only weakly related to buoyancy.	Lenschow & Stephens (1980), Nicholls & LeMone (1980), Crum & Stull (1987), Siebesma & Cuijpers (1995)
T	T contributes substantially to the thermal buoyancy	r also contributes to thermal buoyancy, other forces can be important (see discussion for θ_v)	Manton (1977), Coulman (1978)

There are two explanations for this behavior: there is a measurement error, or some physical mechanism. The potential for measurement errors can be addressed using the two different moisture sensors on the King Air. The LI-COR measured the water-vapor concentration from the IR absorption of a small air sample. This instrument is a fast response instrument and was used to measure moisture fluxes using the eddy covariance technique. The Cambridge chilled-

¹Nicholls and LeMone (1980) used simultaneous values of w and r .

mirror hygrometer measured the dew-point temperature at a rate of 1 Hz. Although the Cambridge has a slower response rate than the LI-COR, fluxes can also be computed using the eddy covariance method. The two measured values of the fluxes should not be the same because of the different response rates of the instruments, but they should be similar. There was good agreement between the Cambridge and LI-COR fluxes for all other BLX96 legs. The Cambridge also reported a moisture flux of $-6.52 \times 10^{-6} \text{ g} \cdot \text{kg}^{-1} \text{ m} \cdot \text{s}^{-1}$ for the leg in question, so the negative moisture flux from the LI-COR is reasonable. The standard deviations of humidity measured by the Cambridge and the LI-COR for this leg were also compared and were not noticeably different from standard deviations computed for the other legs. There is no evidence that the LI-COR flux measurements were in error.

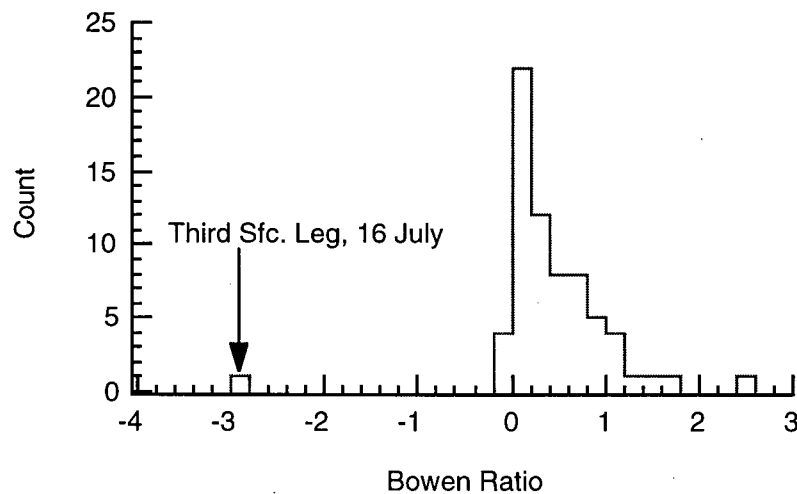


Figure 2.3 Histogram of observed Bowen Ratio (B) vs. count for all BLX96 flight legs. The leg with the questionable moisture flux is marked.

If the measurements were accurate, then there must be a physical process causing the negative moisture flux. It is convenient to decompose the measured moisture flux into three different pieces, the contributions from updrafts, downdrafts and the environment (section 2.3.1). For this leg the moisture flux contributed by the updrafts was very small, about $0.001 \text{ g} \cdot \text{kg}^{-1} \text{ m} \cdot \text{s}^{-1}$. The next smallest moisture flux contribution by updrafts during any other BLX96 leg was

an order of magnitude larger. The contribution to the moisture flux by the downdrafts was also the smallest observed during BLX96, about $0.001 \text{ g}\cdot\text{kg}^{-1} \text{ m}\cdot\text{s}^{-1}$ compared to the next smallest value measured during BLX96 of $0.005 \text{ g}\cdot\text{kg}^{-1} \text{ m}\cdot\text{s}^{-1}$. Because of the small contribution from updrafts and downdrafts, the environmental contribution to the flux is important, even though it is also very small in magnitude. During this leg the environmental moisture flux was negative. A number of other days had negative contributions from the environment, but the flux contribution from updrafts and downdrafts were large enough that the total moisture flux remained positive.

Advection of moist air aloft is one process that could lead to negative moisture fluxes. In general, the surface layer is more moist than the air higher in the boundary layer so that thermals rising through the mixed layer are more moist than their environment, in other words, the thermals have a moisture excess. If the mixed layer is moistening due to moisture advection then the thermal moisture excess is reduced and the moisture flux is reduced and could become negative. While advection leads to the negative moisture flux at the observation height, the moisture flux at the surface is probably positive, so that the surface energy balance is maintained. A negative moisture flux at the surface implies water vapor is condensing, or that dew is forming, which is unlikely on a sunny summer afternoon.

Unfortunately, advection could not be measured with the flight pattern flown during BLX96. But the observed rainfall pattern can give insight into moisture advection. The rainfall for the four days preceding 16 July was determined using a combination of rain gauges and NEXRAD prepared by the Arkansas Red River Basin River Forecast Center (<http://www.srh.noaa.gov/abr/c/>). Their algorithm compares the rainfall totals from rain gauges to the NEXRAD network. A bias is calculated and the NEXRAD values are adjusted (Fulton et al. 1998). NEXRAD observations are desirable for intermittent rain. In the days leading up to 16 July, there was much rain to the south of the Meeker track, but not much over the track itself (Figure 2.4). Up to 10 cm of rain fell to the south of the Meeker track between 12 UTC 13 July and 12 UTC 14 July, while only 2 cm fell over the track itself. Winds on 16 July were about

5 m s⁻¹, the strongest winds observed for the days included in this study. The southerly winds and rain pattern suggest that there should be strong moisture advection along the Meeker flight track. Observations by the airborne scientific observer support this contention. He reported that the surface under the track looked relatively dry with scattered cumuli humilis above the track, while cumuli mediocris and cumuli congestus were observed to the south of the flight track, indicating that the surface to the south could be more moist.

Further evidence of moisture advection can be found. The moisture advection can be calculated using data from the ARM SGP CART radiosondes. These radiosondes were launched every three hours (at 11:30, 14:30, 17:30 LST) from the central facility and boundary facilities located near the edge of ARM SGP CART domain. Each radiosonde was separated by approximately 180 km. A plane was fit through the mixed-layer mean r calculated from each radiosonde profile, and the horizontal derivatives of the r field were calculated from this plane. Horizontal wind velocity was taken from the leg means measured with the aircraft. On 16 July the average moisture advection was $3.8 \times 10^{-5} \text{ g} \cdot \text{kg}^{-1} \text{ s}^{-1}$, which was the second largest value measured during BLX96.

This leg will be excluded from the rest of the study because the moisture flux is dominated by advection, rather than convective processes. Two elevated legs, flown immediately before this surface leg will also be excluded because the proper scaling variables can not be calculated without the near surface leg.

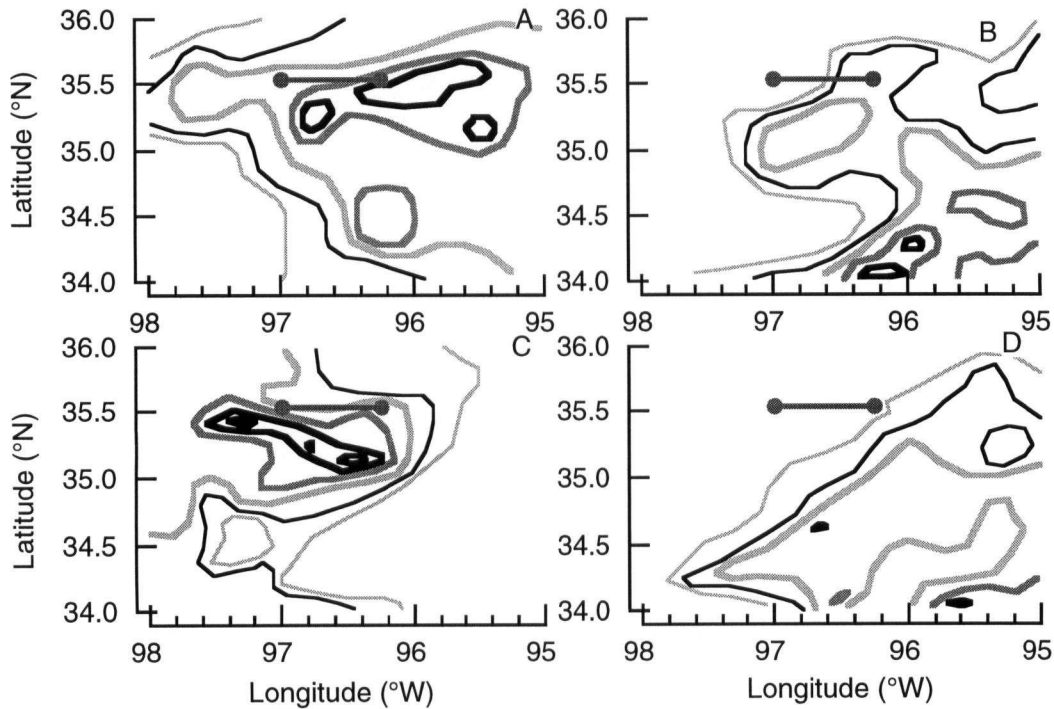


Figure 2.4 Contours of 24 hour accumulated precipitation for 24 hour periods ending at 12 UTC 12 July (A), 12 UTC 13 July (B), 12 UTC 14 July (C), and 12 UTC 15 July (D) from the combination of NEXRAD and rain gauge measurements. The first contour marks 0.5 cm (thin grey line), the second contour marks 1.0 cm (thin black line), the third contour marks 2.0 cm (heavy grey line) with a 2.0 cm contour interval thereafter. The heavy solid line with circles shows the Meeker flight track.

2.5 Net Data Available

After excluding flight legs flown on 21 July because of instrument errors, and the second set of legs flown on 16 July (three legs total) because of excess moisture advection, we are left with 65 legs of good data. These good legs are listed in Table 2.2, and will be used in the remainder of this research.

Table 2.2 List of BLX96 case study days, location, time, z/z_i , typical boundary-layer wind speed and direction and weather synopsis. Wind speeds less than 2 m s^{-1} are reported as light.

Date	Location	Time (LST)	z/z_i	Wind Speed (m s^{-1}), Direction	Weather
15 July	Lamont	10:12	0.061	2.5-5, 180-210°	Frontal passage on 13 July, weak pressure gradient
		11:22	0.62		
		11:37	0.29		
		11:52	0.034		
		13:10	0.33		
		13:25	0.094		
		13:40	0.025		
16 July	Meeker	10:45	0.053	5, 160-180°	Frontal passage on 13 July, weak pressure gradient
		11:56	0.74		
		12:10	0.30		
		12:26	0.03		
22 July	Winfield	11:12	0.057	2.5, 180-200°	MCC in Nebraska with approaching front.
		12:07	0.80		
		12:23	0.38		
		12:40	0.048		
		13:51	0.43		
		14:07	0.11		
		14:23	0.035		

Table 2.2 continued.

Date	Location	Time (LST)	z/z_i	Wind Speed (m s^{-1}), Direction	Weather
23 July	Lamont	11:46	0.039	Light, Variable southerly	Cb in North-Central Oklahoma overnight with frontal passage. Fair weather today
		12:53	0.036		
		14:05	0.43		
		14:20	0.17		
		14:37	0.027		
25 July	Winfield	11:05	0.046	Light, Variable northerly	Cb rained heavily on 24 July, small low- level ridge allowed fair weather today.
		12:19	0.47		
		12:35	0.22		
		12:50	0.026		
		14:05	0.28		
		14:20	0.083		
		14:36	0.022		
28 July	Meeker	11:19	0.15	Light, variable southwesterly	Mid-level ridge gave fair weather over much of the region
		12:32	0.61		
		12:49	0.29		
		13:05	0.04		
		14:19	0.34		
		14:37	0.11		
		14:53	0.039		

Table 2.2 continued.

Date	Location	Time (LST)	z/z_i	Wind Speed (m s^{-1}), Direction	Weather
31 July	Winfield	11:13	0.046	Light, variable southeasterly	Thunderstorms along approaching front kept to north during the day
		12:25	0.60		
		12:42	0.29		
		12:59	0.044		
		14:10	0.33		
		14:27	0.088		
		14:44	0.032		
2 Aug.	Meeker	10:59	0.088	Light, variable southeasterly	Front to the south washed out. Mid- and upper-level ridging kept disturbances to the north
		12:11	0.80		
		12:27	0.53		
		12:44	0.060		
		13:57	0.68		
		14:13	0.23		
13 Aug.	Lamont	11:03	0.033	Light and variable	Ridging at all levels, subsidence kept skies clear; very moist boundary layer contributed to haze.
		11:45	0.11		
		12:03	0.042		
		12:20	0.18		
		12:37	0.55		
		12:53	0.37		
		14:40	0.029		

Chapter 3: A New Moisture Scale for Convective Boundary Layers

3.1 Introduction

Similarity theory has proved to be a powerful tool that can be used to study a wide range of boundary layers, from flow in pipes to flow over the Earth's surface. This method can be used to collapse observations into a universal form. Empirical parameters can be fit to these universal forms to yield results that are valid at any time or place. One example is an equation for the variance of a scalar (σ_ψ^2) as a function of height above the Earth's surface. By choosing the proper scale (ψ_*), we hope that an expression like the following is true:

$$\sigma_\psi^2/\psi_*^2 = f(z/z_i), \quad (3.1)$$

where z is the height above ground, z_i is the mixed layer depth, and f is some function of dimensionless height. Numerous authors have developed similarity relationships that are valid in the stable, neutral, and unstable boundary layer (see Stull 1988 and 1990 for listing of many similarity scales).

Monin and Obukhov (1954) and Obukhov¹ (1971) introduced a number of important scales applicable in the atmospheric surface layer, including: friction velocity, roughness length, a length scale (later named the Monin-Obukhov length), and a temperature scale. This scaling is valid for any stability, as long as the winds are not calm. They utilized the assumption that fluxes in the surface layer are constant with height. Using the scales introduced by Monin and Obukhov, Businger et al. (1971) and Dyer (1974) independently derived similarity relationships for wind shear and heat flux near the Earth's surface.

Wyngaard et al. (1971), Wyngaard (1973), and Sorbjan (1986) applied the Monin and Obukhov scales to make dimensionless turbulent fluxes and other moments for a special case they called local free convection. A unique feature of this scaling is that z is an important scale. Local free convection scaling is valid for z much less than z_i . Although these results are useful, relationships applicable to the entire mixed layer are desirable.

¹This reference is an English translation of Obukhov (1946) (Businger and Yaglom 1971)

In his ground-breaking work using a numerical model, Deardorff (1970a) introduced a new mixed-layer similarity valid for cases where buoyancy is the dominant force driving convection. He determined the scales to be: the convective velocity (w_*), later named the Deardorff velocity, a temperature scale (θ_*), and a humidity (or passive scalar) scale (r_*) (Deardorff 1970a, 1974). He used z_i as a boundary-layer length scale. He defined w_* , θ_* , and r_* as

$$w_* = \left[(g/T_v) z_i \overline{w' \theta'_{v,s}} \right]^{1/3}, \quad (3.2a)$$

$$\theta_* = \overline{w' \theta'_{v,s}} / w_*, \quad (3.2b)$$

$$r_* = \overline{w' r'_{s}} / w_*, \quad (3.2c)$$

where g is the gravitational acceleration, $\overline{T_v}$ is the layer average virtual temperature, $(g/T_v) \overline{w' \theta'_{v,s}}$ is the surface buoyancy flux, r is the water-vapor mixing ratio, and $\overline{w' r'_{s}}$ is the surface moisture flux. Originally, he demonstrated the usefulness of these scales using both observations of the atmosphere and tank experiments of Rayleigh convection between two plates (Deardorff 1970b). Later, these scales were successfully applied to tank experiments designed to represent the atmospheric boundary layer (Deardorff 1972; Willis and Deardorff 1974; Deardorff and Willis 1985). Kaimal et al. (1976) successfully applied Deardorff scaling to observations from a field experiment conducted over northwestern Minnesota.

While Deardorff's scaling was shown to be useful, it seems to fail high in the boundary layer, near the entrainment zone. Using a wind tunnel, Fedorovich et al. (1996) found that there was still scatter in temperature measurements near the top of the mixed layer. The failure is most severe for passive scalars, like r . Lenschow and Stephens (1980) measured r during the Air Mass Transformation Experiment (AMTEX). Their scatter plots of \bar{r} and the variance of r (σ_r^2), which they normalized by r_* still varied by over an order of magnitude near z_i . Similar results were found during BLX96, where there was still considerable scatter near z_i after normalization by Deardorff's r_* .

While the apparent shortcomings in the traditional Deardorff scaling were being revealed, new methods were being proposed. Guillemet et al. (1983) developed scales based on (3.2) and

lapse rates above z_i . Wyngaard and Brost (1984) and Moeng and Wyngaard (1984) developed a scaling based on the top-down bottom-up turbulence model. They derived an equation for the scalar variance to be [Moeng and Wyngaard 1984, equation (3.4)]

$$\sigma_r = r_* (f_b + 2Rf_{tb} + R^2 f_t)^{1/2}, \quad (3.3)$$

where f_b , f_{tb} , and f_t are functions of height that define the contribution from the fluxes at the bottom, correlation between the fluxes at top and bottom, and the fluxes at the top of the boundary layer, respectively, and R is the ratio of the entrainment flux to the surface flux. Near the surface they found that the bottom-up flux dominated (3.3). Sorbjan (1990 and 1991) introduced new similarity scales for both penetrative and non-penetrative convection. Like the work of Wyngaard and Brost and Moeng and Wyngaard, his scales were based on the fluxes at the top and the bottom of the mixed layer [Sorbjan 1991, equation (8)]

$$\sigma_r = r_* \left[c_{5b} \frac{(1-z/z_i)^{4/3}}{(z/z_i)^{2/3}} + c_{5t} R_r^2 R_{\theta_v}^2 \frac{(z/z_i)^{4/3}}{(1-z/z_i + D)^{2/3}} \right]^{1/2} \quad (3.4)$$

where c_{5b} and c_{5t} are empirical constants, R_r^2 is the ratio of the entrainment moisture flux to the surface moisture flux, $R_{\theta_v}^2$ is the ratio of the entrainment buoyancy flux to the surface buoyancy flux, and D is the ratio of the entrainment zone depth to z_i . Sorbjan found that $c_{5b}=2.35$ and $c_{5t}=8$ for two different field projects over France. Near the surface (3.4) is dominated by the flux at the bottom of the mixed layer. Using a laboratory tank model with saline convection, Hibberd and Sawford (1994) found slightly different constants for density perturbations than those proposed by Sorbjan (1991). Zilitinkevich (1994) developed scales which account for turbulence driven by both wind shear and buoyant convection.

Santoso and Stull (1998, 2001) defined a new type of scaling valid from the surface to the portion of the boundary layer where variables become constant with height. They called this new layer the radix layer, which encompasses the traditionally defined surface layer and part of the well-mixed layer. They proposed that the height of the Radix layer top represents a useful length scale.

Equations like (3.3) and (3.4) are helpful and provide a physical basis for the form of the

normalized variances as a function of height. However, they can not be applied to other statistical moments of the scalar, the spectra of a scalar, or other parameters that might be related to the variable of interest because of their empirical constants. Given the shortcomings of the traditional Deardorff scaling, and difficulties in applying (3.3) and (3.4), a new scale for a passive scalar is defined. This new scale will be used in Chapter 6, where a parameterization for the JFDs is developed.

3.2 A new scaling

Like Wyngaard and Brost (1984), Moeng and Wyngaard (1984), and Sorbjan (1990, 1991 and 1999) this new scale assumes that (3.2c) is valid close to surface, and that (3.2c) does not do as good a job high in the mixed layer because of entrainment. Therefore, an expression that is dominated by the surface flux near the surface and the entrainment flux near the mixed layer top is desirable. A simple expression that fulfills these criterion is, assuming that the flux is a linear function of height, is

$$r_{*,new} = \left[\frac{\overline{w' r'_s} (1 - z/z_i)}{w_*} + \frac{\overline{w' r'_{z_i}} (z/z_i)}{w_*} \right] f(z/z_i), \quad (3.5)$$

where $\overline{w' r'_s}$ is the moisture flux at the surface, $\overline{w' r'_{z_i}}$ is the moisture flux at z_i (the entrainment moisture flux), and f is some function of dimensionless height. In his (3.2c), Deardorff does not include the function f because he is not explicitly modeling the behavior of the variable or statistical moment, as the other authors have done. Equation (3.5) is simply a more general case of (3.3) and (3.4) because it does not apply to only one statistical moment. Equation (3.3) has an additional cross term, which (3.5) would have if squared. Likewise, (3.5) is similar to (3.4) if w_* is used as the velocity scale rather than the scale used by Sorbjan (1990).

3.3 Results

Equation (3.5) can be used to normalize the standard deviation of r (σ_r) observed during BLX96 (Figure 3.1). It appears that (3.5), using $f=1$, does a better job than the traditional

Deardorff scaling because the scatter in Figure 3.1 is reduced at all levels. Particularly above $0.2 z_i$, the new scaling does a good job reducing the scatter because $\overline{w r_{z_i}}$ is included. The reduction in scatter of the data near the surface by both Sorbjan's scaling and the new scaling is surprising, because both approach Deardorff scaling near the surface. Some BLX96 near-surface legs had small near-surface moisture fluxes, so that the Deardorff r_* is very small. In these cases, the contribution from the entrainment flux is still significant because of the small surface flux.

The results using Sorbjan's method, shown in Figure 3.1, are not completely fair. Equation (3.4) was designed to predict the form of σ_r/r_* rather than reduce the scatter. If σ_r is divided by the right hand side of (3.4) the observations should collapse to a constant value of 1. That is not the case for BLX96 data, although the scatter is reduced considerably (all of the points lie between 0 and 5), but the average value is 1.7 not 1 (not shown). As stated earlier, the primary disadvantage of Sorbjan's methods is that they can not easily be applied to other statistical moments.

3.4 Conclusions

A new scale for a passive boundary layer scalar is proposed that is a function of both the surface flux and the entrainment flux of the scalar. For BLX96 data this new scaling significantly reduces the scatter in the observed moisture statistics compared to the standard mixed layer scaling proposed by Deardorff (1970a, 1970b). This new scale is not meant to replace the more physically based scaling published by other authors that can predict the functional form of the variances (Wyngaard and Brost 1984; Moeng and Wyngaard 1984; Sorbjan 1990, 1991). The benefit of this new scaling is that it can easily be applied to other statistical moments or used to create nondimensional groups. It will be used in this dissertation to normalize the moisture observations.

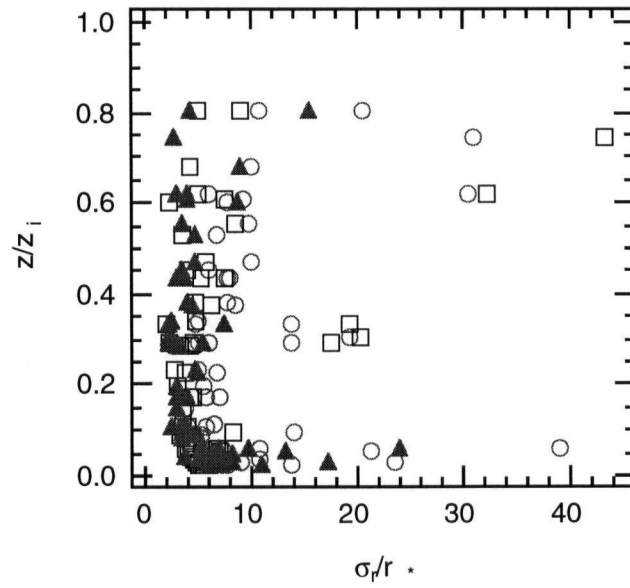


Figure 3.1. Plot showing σ_r/r_* vs. z/z_i using the standard r_* (3.2c) (circles), Sorbjan's scaling (3.4, using suggested c_{5t} and c_{5b} and BLX96 observed values of R_r , R_{θ_v} , and D) (squares), and $r_{*,new}$ (3.5, with $f = 1$) (triangles) for all BLX96 case study days.

Chapter 4: Properties of Coherent Drafts Observed During BLX96

4.1 Introduction

The coherent updrafts and downdrafts are important features in the convective boundary layer. Properties of coherent drafts observed during different field experiments have been reported in the literature (Frisch and Businger 1973; Coulman 1978; Lenshow and Stevens 1980; Khalsa and Greenhut 1985; Greenhut and Khalsa 1987; Young 1988; Williams and Hacker 1992). The methods used to find the coherent drafts in the BLX96 observations were described in Chapter 2.

The temperature properties of the thermals have been reported extensively, and are similar to results from BLX96, and will not be reported here. There seems to be some discrepancy in the fraction of the boundary layer that is covered by thermals, so the fraction of each leg covered by updrafts and downdrafts during BLX96 is reported in Section 4.2. Moisture properties of the updrafts and downdrafts will be reported in Section 4.3. Finally, some comments on mass flux approximations will be made in Section 4.4.

4.2 Fractional coverage of drafts

There has been much discussion in the literature about the fraction of the boundary layer that is covered by updrafts and downdrafts. Young (1988) found that approximately 45% of the boundary layer over land consists of thermal updrafts. Coulman (1978) reported that the coverage of thermals is about 40%. This is substantially different than the 16% found by Greenhut and Khalsa (1982). Lenshow and Stephens (1980) reported an intermediate value of about 28% over the ocean.

Young (1988) attributed the differences in the fractional coverage to different definitions of w_{thresh} . In Chapter 2, w_{thresh} for this study [and that used by Greenhut and Khalsa (1982)] was defined as $w_{thresh} = \sqrt{\sigma_{\pm w}^2/2}$. The $\sqrt{1/2}$ factor is the arbitrary threshold multiplier (m_{thresh}) defined in section 2.3.2. Figure 4.1 shows the observed coverage of updrafts and downdrafts for m_{thresh} ranging from 0, such as used by Young (1988) to $\sqrt{1/2}$ used by Greenhut and Khalsa (1982). As

expected, the fractional coverage of drafts changes as a function of m_{thresh} , with smaller values of m_{thresh} giving larger coverage by drafts. In each case, it appears that the cover of updrafts observed during BLX96 was less than the cover observed in other field experiments. The difference was smallest for the results reported by Greenhut and Khalsa (1982). The experiments by Lenschow and Stephens (1980) and Young (1988) had flight legs about half the length used during BLX96. Greenhut and Khalsa's (1982) flight legs were much longer than those flown during BLX96, on the order of hundreds of kilometers. In each case there were also minor differences in the length scale. It seems that the fraction of each flight leg covered with thermals during BLX96 is consistent with the observations from other field campaigns, depending on the threshold multiplier used. The research shows that the fraction of the boundary layer covered by drafts is a strong function of the criteria used. Young's (1988) criteria are less exclusive than that used by Greenhut and Khalsa (1982) so that Young identifies more thermals. For the work in later chapters we will focus only on more robust thermals so that the more restrictive definition of Greenhut and Khalsa (1982) will be used. The apparent linear change for threshold multipliers ranging from 0 to 0.4 for the BLX96 data was unexpected. Other factors, such as clouds, terrain, surface cover could also influence the fraction of the boundary layer covered by thermals.

The variation of the updraft and downdraft fraction with height is also of interest and will be used in Chapter 8. The updraft and downdraft fraction, using $m_{thresh} = \sqrt{1/2}$ and $m_{thresh} = 0$ is shown in Figure 4.2. Using $m_{thresh} = \sqrt{1/2}$, the fraction of each leg covered by either updrafts or downdrafts increases rapidly below $0.1z_i$. Above $0.1z_i$ it appears that the fraction of the leg covered is not a strong function of height. Using $m_{thresh} = 0$, the fraction covered by either updrafts or downdrafts seems to decrease some with height below $0.1z_i$. This behavior is expected because using $m_{thresh} = 0$ is less selective, so that more drafts are defined. However, above $0.1z_i$ it appears that the fraction of the leg covered by either updrafts or downdrafts increases slightly with height.

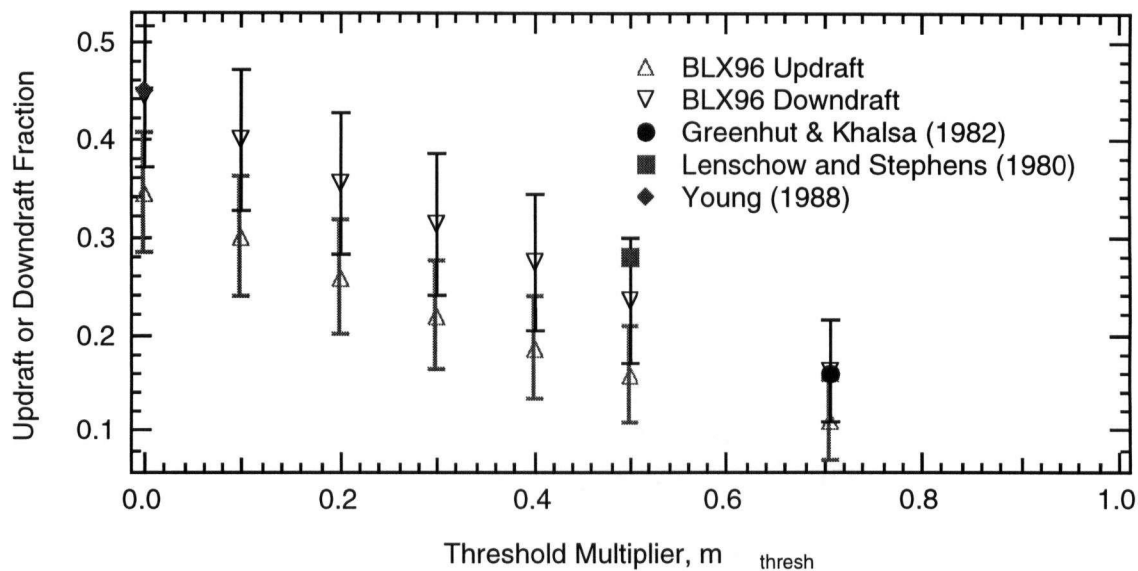


Figure 4.1. Updraft (upward pointing triangles) or downdraft fraction (downward pointing triangles) observed during BLX96 and selected updraft fraction reported during other field experiments by Greenhut and Khalsa (1982) over water (filled circle), Lenschow and Stephens (1980) over water (filled square), and Young (1988) (filled diamond) over land vs. m_{thresh} . Error bars indicate observed standard deviations from BLX96 flight legs.

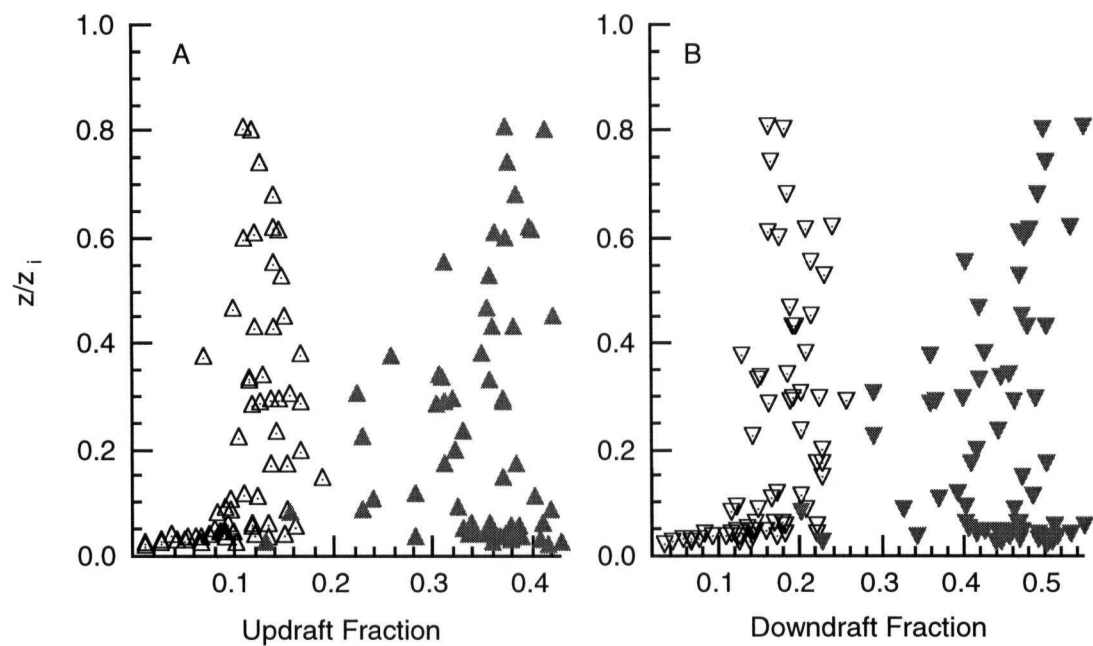


Figure 4.2. Fraction of the BLX96 flight legs covered by (A) updrafts and (B) downdrafts given $m_{thresh} = \sqrt{1/2}$ (open symbols) and $m_{thresh} = 0$ (filled symbols).

4.3 Updraft and downdraft properties

Many authors (Manton 1977; Coulman 1978; Lenschow and Stephens 1980; Khalsa and Greenhut 1985; Greenhut and Khalsa 1987; Young 1988; Williams and Hacker 1992) have reported the behavior of $\overline{\delta\theta}/\theta_*$ as a function of height, where δ indicates a difference between the draft property (either updraft or downdraft) and the leg mean, the overbar indicates an average over all up or downdrafts, and θ_* is the convective velocity scale (3.2b) and is defined to be $\theta_* = \overline{w\theta}_{sc}/w_*$, where w_* is the Deardorff velocity scale (3.2a), $w_* = \left[(g/T_v) z_i \overline{w\theta}_{vs} \right]^{1/3}$, and a subscript u or d is used to indicate an updraft or downdraft. All authors have found that $\overline{\delta\theta}_u/\theta_*$ and $\overline{\delta\theta}_d/\theta_*$ are well defined functions of height. Results from BLX96 were similar and will not be shown.

Of the previous work listed, only Manton (1977), Coulman (1978), Young (1988) and Williams and Hacker (1992), measured thermals in the convective boundary layer over land. Only Coulman (1978) reported the moisture properties of updrafts. Both $\overline{\delta r}_u$ and $\overline{\delta r}_d$ measured during BLX96 were normalized by $r_{*,new}$ (3.5). Updrafts near the surface are more moist than the environment (Figure 4.3). Higher in the boundary layer the moisture excess decreases. Near the top of the mixed layer there is more scatter, and the lack of observations makes an accurate analysis difficult. Intuitively, we would expect the moisture excess of updrafts to increase near the top of the mixed layer because each thermal is surrounded by drier air entrained from the free atmosphere. The coherent downdrafts are drier than the environment high in the mixed layer, and the moisture deficit of the downdrafts increases in magnitude lower in the boundary layer. Coulman (1978) had similar results near the surface, although a direct comparison is difficult because Coulman used a different normalization. Near the mixed-layer top, his values of humidity perturbation of the thermal continue to decrease. This apparent discrepancy might be explained by his normalization by σ_r , which also can be large near the mixed layer top. Lenschow and Stephens (1980) and Greenhut and Khalsa (1987) report results for updrafts over the ocean that are similar to those from BLX96. In both cases, their data suggest large values of $\overline{\delta r}_u$ near the mixed-layer top.

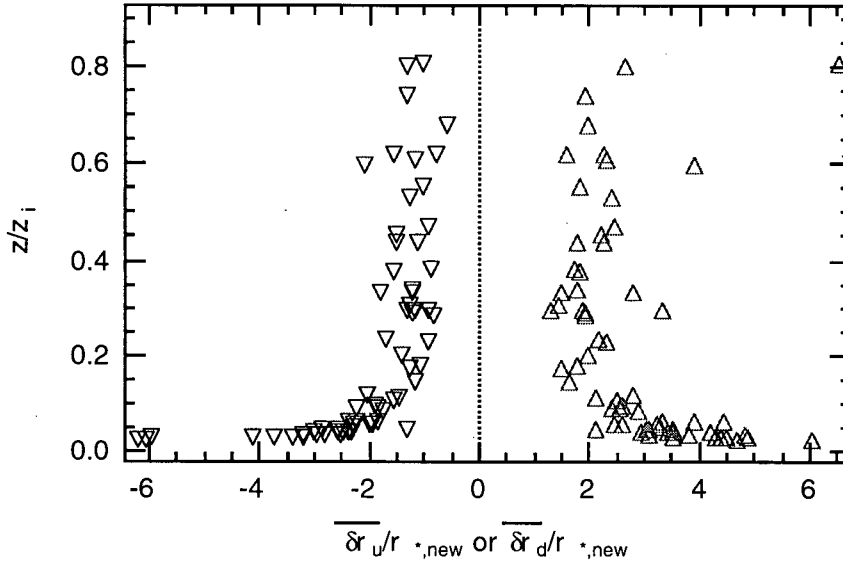


Figure 4.3. Plot showing $\overline{\delta r_u}/r_{*,new}$ (upward pointing triangles) and $\overline{\delta r_d}/r_{*,new}$ (downward pointing triangles) vs. z/z_i for all BLX96 case study days.

4.4 Comments on convective mass-flux parameterizations

Many authors have suggested using a convective mass flux approximation to represent the turbulent fluxes (Betts 1975, 1976; Manton 1975; Greenhut and Khalsa 1982, 1987; Nicholls and LeMone 1980; Randall et al. 1992; Siebesma and Cuijpers 1995; among others). This type of parameterization uses observed updraft and downdraft properties to determine the turbulent flux and will be used in Chapter 6 to develop a parameterization for the tilt of the JFDs. According to the mass-flux approximation, the flux of any variable, ψ , can be expressed as

$$\overline{w\psi} = \omega(\psi_T - \psi_{env}), \quad (4.1)$$

where ω is some convective velocity scale, ψ_T is the thermal value of ψ , and ψ_{env} is the environmental value of ψ . Three important assumptions are used to obtain (4.1): the area covered by drafts is small, the population of thermals can be represented by an average value, and that thermals and return circulation produce most of the flux, in other words, that the flux due to variations within the thermal and within the environment is small. Greenhut and Khalsa (1982) and Randall et al. (1992) suggested explicit inclusion of downdrafts in (4.1), so that

$$\overline{w\psi} = A(\overline{\rho_u \delta w_u \delta \psi_u} \alpha_u + \overline{\rho_d \delta w_d \delta \psi_d} \alpha_d), \quad (4.2)$$

where ψ is any variable, $\overline{\delta w}$ is the average draft velocity, $\overline{\delta \psi}$ is the average draft value of ψ , α is the fractional area covered by drafts, u indicates updrafts, d indicates downdrafts and A is some constant. This formulation ignores the contribution to the flux from variation within drafts, variation among drafts, or variations in the environment, also called the environmental flux. Greenhut and Khalsa (1982) found that $A = 1.25$, while Schumann and Moeng (1991) found that $A \approx 1.3$ for results from an LES. As Greenhut and Khalsa (1982) and Schumann and Moeng (1991) found, and is shown in Figure 4.4, (4.2) does a good job representing both the moisture and the heat flux measured by the aircraft during BLX96. The good agreement between the updraft and downdraft fluxes indicates that, in general, the assumptions used to obtain (4.1) and (4.2) are valid. In the illustration shown in Figure 4.4, a value of $A = 1.0$ was used.

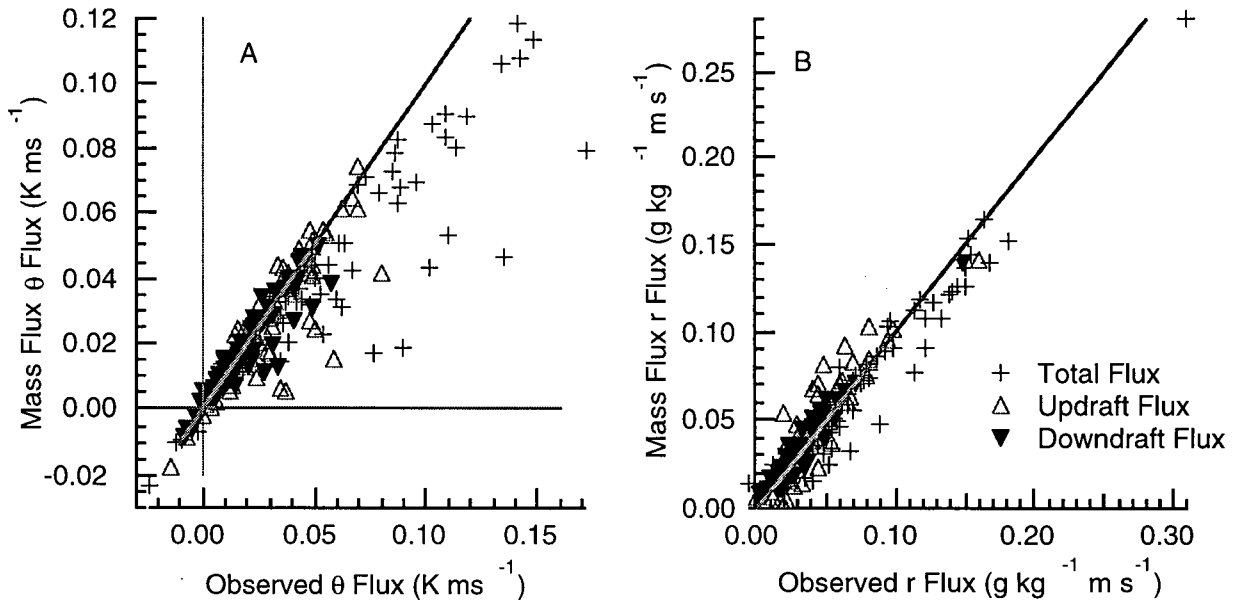


Figure 4.4. BLX96 mass-flux predicted flux vs. observed flux for the total flux (crosses), updrafts (upward pointing triangles) and downdrafts (downward pointing triangles) A) θ flux, B) r .

The largest discrepancies between the observed and mass-flux predicted fluxes occurred near the surface (Figure 4.5). It is convenient to define a normalized flux error

$$err_{flux} = \left(\overline{w'\psi'}_{mf} - \overline{w'\psi'}_{obs} \right) / \left(\overline{w'\psi'}_{obs} \right), \quad (4.3)$$

where err_{flux} is the flux error, $\overline{w'\psi'}_{obs}$ is the leg observed flux, $\overline{w'\psi'}_{mf}$ is the mass flux predicted flux (4.2). The large errors near the surface can be explained by turbulence occurring at length scales smaller than the critical length scale. The flux from these small drafts are treated as part of the environmental flux. Schumann and Moeng (1991) report similar results for the heat flux in a dry convective boundary layer where the subgrid flux predicted by the LES is large. The evidence in Figure (4.5) supports the notion that small-diameter “plumes” in the surface layer merge as they rise into larger diameter “thermals” in the mixed layer.

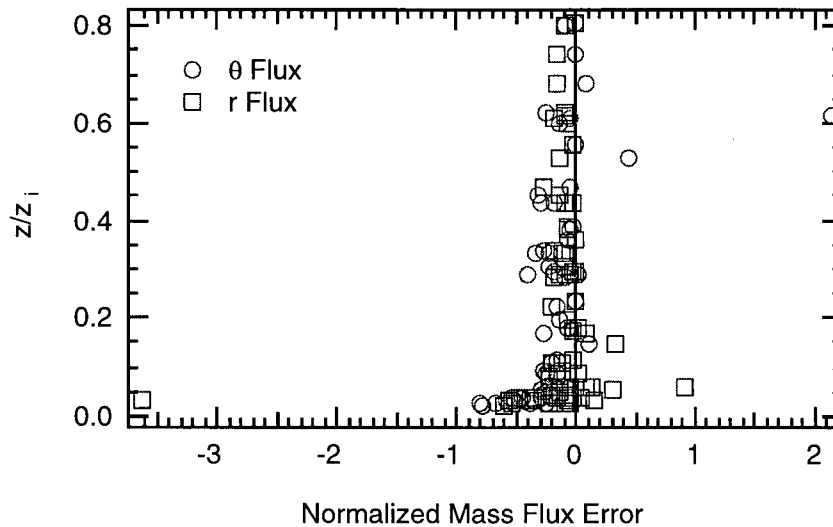


Figure 4.5. Plot of err_{flux} vs. z/z_i for all BLX96 case study days for $\overline{w'\theta'}$ (circles) and $\overline{w'r'}$ (squares).

4.5 Conclusions

In this chapter properties of coherent updrafts and downdrafts were investigated. Other researchers have reported large differences in the amount of the boundary layer covered by thermals. As speculated by Young (1988) the difference is related to the value of w_{thresh} . The

humidity of both updrafts and downdrafts over land were also reported and found to be similar to observations over water.

The standard mass flux approximation (4.2) was checked to ensure that it can be used to estimate fluxes during BLX96. The method works well, but the environmental flux can be large, especially near the surface. These results will be used in Chapter 6 to develop a parameterization for joint frequency distributions measured in the boundary layer.

Chapter 5: Observations and Models of Joint Frequency Distributions in the Daytime Convective Boundary Layer

5.1 Introduction

Joint frequency distributions (JFDs), also known as joint probability density functions, can provide a convenient framework for the investigation of physical processes in the convective boundary layer. In addition, discrete JFDs reduce the size of a long time series by combining many observations into finite sized bins. Holland (1973) used JFDs to investigate wave shapes, Mahrt and Paumier (1982) used JFDs of specific humidity and potential temperature (θ) to look at the effects of entrainment and mixing in a stratocumulus-topped boundary layer. Grossman (1984) used JFDs of vertical velocity (w) and water-vapor density to perform conditional sampling of data measured in a maritime boundary layer. He defined thermally direct and indirect fluxes using these JFDs. Using data from the Air Mass Transformation Experiment, Mahrt and Paumier (1984) constructed JFDs of w and θ . Deardorff and Willis (1985) examined JFDs of w and temperature generated from their laboratory tank model. They also used JFDs to perform conditional sampling, looking for coherent structures in the boundary layer. Wang and Stevens (2000) used Large Eddy Simulation (LES) to simulate JFDs from a maritime shallow cumulus case and a maritime stratocumulus case.

While these authors used JFDs as tools to examine the convective boundary layer, they did not attempt to quantify the physical processes that led to the shape of JFDs. Wyngaard and Moeng (1992) (hereafter WM) addressed this issue. They suggested a statistical approach, using the correlation between w and any arbitrary scalar to describe the tilt of the JFDs of w and the scalar. They compared their theoretical JFDs to JFDs generated by a LES. Schrieber et al. (1996) (hereafter SSZ) examined distributions of virtual potential temperature (θ_v) and moisture [their moisture variable was the height of the lifting condensation level (z_{LCL})]. They took a different tack than WM, developing a physically based method to explain the tilt of JFDs observed in the surface layer during HAPEX [Hydrologic-Atmospheric Pilot Experiment] (André, et al. 1986).

Two new conceptual models that describe the physical characteristics of JFDs of θ vs. water-vapor mixing ratio (r) are proposed in this chapter. Like the work of SSZ, these methods are based on physical processes in the boundary layer. In the first method, three different JFDs will be added together to form a single distribution of θ vs. r . These JFDs are: one representing updrafts, one representing downdrafts, and another representing the environment. Although this method does a good job, it needs a large number of parameters; therefore, a second, more compact method, is also introduced. The second approach views mixed-layer turbulence as a simple mixing process, and views the JFD of θ vs. r as a mixing diagram (Paluch 1979; Hanson 1984; Betts 1984, 1985; Betts and Albrecht 1987). When advection is small, the mixed-layer distribution is a mixture of air from two different source regions, the surface layer and the free atmosphere. The relationship is complicated because the thermodynamic properties of one or both of the source regions changes throughout the day. In this work, the properties of the mixed layer, the surface and the free atmosphere are used to align the distributions. Data from Boundary Layer Experiment 1996 (BLX96) will be used to demonstrate that the new methods can successfully predict the size and shape of the JFDs in the convective mixed layer.

First, some definitions associated with JFDs will be presented. Then the methods proposed by MW and SSZ will be applied to JFDs of θ vs. r observed during BLX96. Next, the new methods will be introduced. Finally, JFDs constructed using the two new methods will be compared to the older methods using data from BLX96.

5.2 Definitions

Joint frequency distributions simply define the probability that some observation, $\hat{\theta}$ and \hat{r} lies within an interval $d\theta$ dr

$$f(\theta, r) d\theta dr = \text{prob}(\theta < \hat{\theta} < \theta + d\theta, r < \hat{r} < r + dr). \quad (5.1)$$

Since the probability of finding the observation, $\hat{\theta}$ and \hat{r} , somewhere within the whole θ - r “space” is by definition 1, it follows that

$$\int_{-\infty}^{\infty} \int_{-\infty}^{\infty} f(\theta, r) d\theta dr = 1. \quad (5.2)$$

For the case of discrete JFDs, (5.2) can be written in terms of summations and the discrete bin size. If each of the variables has a normal distribution, then their joint normal distribution can be expressed as (for a distribution of θ vs. r)

$$f(\theta, r) = \frac{1}{2\pi\sigma_\theta\sigma_r(1-\rho_{\theta,r}^2)^{-1/2}} \exp\left\{-\frac{1}{2(1-\rho_{\theta,r}^2)}\left[\left(\frac{\theta-\bar{\theta}}{\sigma_\theta}\right)^2 - \frac{2\rho_{\theta,r}(\theta-\bar{\theta})(r-\bar{r})}{\sigma_\theta\sigma_r} + \left(\frac{r-\bar{r}}{\sigma_r}\right)^2\right]\right\}, \quad (5.3)$$

where $\rho_{\theta,r}$ is the correlation between θ and r , σ_θ is the standard deviation of θ , σ_r is the standard deviation of r , and the overbar represents a mean quantity. As indicated by equation (5.3) the interplay of the three parameters: $\rho_{\theta,r}$, σ_θ and σ_r control the tilt of, and spread along, the major and minor axes of the JFD.

5.3 Observations

While SSZ were the first to publish JFDs of θ_v vs. z_{LCL} , their data were limited to observations made approximately 100 m above the surface (roughly $0.05 z_i$ to $0.10 z_i$) during HAPEX. During BLX96, JFDs of θ vs. r were observed at heights ranging from $0.02 z_i$ to just above $0.8 z_i$, with most flight legs below $0.6 z_i$. The BLX96 flight legs also covered a larger horizontal distance than the HAPEX flights. As found by SSZ, a number of attributes seem to be common to all of their JFDs. The JFDs that we observed aloft share the key attributes described by SSZ for JFDs near the surface; namely, they are bounded, they are sharply peaked, the spread is skewed along any axis of the distribution, they have a tilted major axis, and a few JFDs have multiple peaks. However, there are some important differences. All the JFDs observed below $0.1 z_i$ have a positive correlation between θ and r ($\rho_{\theta,r}$), in other words, there is a positive slope to the major axis (Figure 5.1). Namely, warm air is usually more humid in the surface layer. There is also a large range in the observed $\rho_{\theta,r}$. Between 0.2 and $0.4 z_i$ there is a transition zone where some, but not all the JFDs have a negative $\rho_{\theta,r}$, or in other words, a negative tilt. Above

$0.4 z_i$, all of the observed JFDs have a negative $\rho_{\theta,r}$.

These measured values of $\rho_{\theta,r}$ can be compared to those reported by Wyngaard et al. (1978). It appears that $\rho_{\theta,r}$ measured by Wyngaard et al. (1978) are larger near the surface than those measured during BLX96. Their measurements were from over the ocean where convection was driven by cold air flowing over warm water. In this scenario, one would guess that $\rho_{\theta,r}$ would be quite large because the surface layer is very moist. Over the middle of a continent, one would expect some of the thermals to be relatively dry and that a smaller value of $\rho_{\theta,r}$ is expected. The observed differences between the results of Wyngaard et al. (1978) and BLX96 have important implications for the parameterizations of the JFDs. It means that $\rho_{\theta,r}$ is not universal, but changes from time to time and place to place.

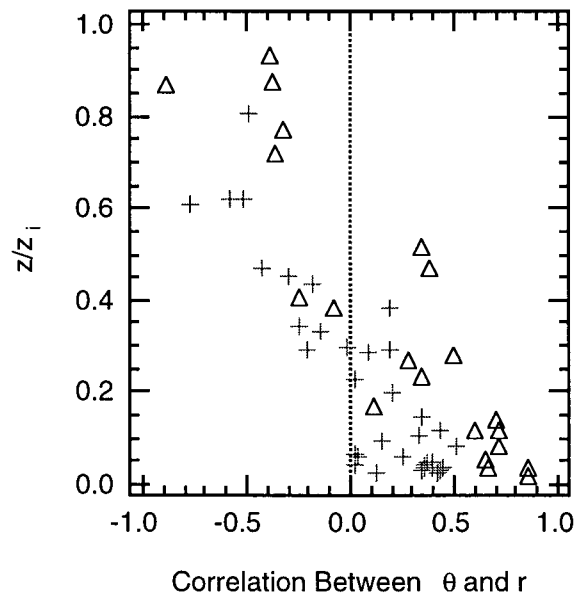


Figure 5.1. Correlation of θ and r for BLX96 flight legs (crosses) and observations from Wyngaard et al. (1978) (triangles) over the ocean vs. z/z_i measured during BLX96 horizontal flight legs.

The change of $\rho_{\theta,r}$, or the change of tilt of the JFDs with height can be explained. Solar energy is absorbed at the Earth's surface. Surface-layer processes cause air near the surface to warm and become more moist. As these warm and moist parcels rise above the surface they cause

the observed positive tilt. Near z_i , entrainment brings relatively warm and dry parcels from the free atmosphere down into the mixed layer. These warm and dry parcels lead to the observed negative tilt. Any method used to describe JFDs through the depth of the boundary layer must account for this behavior.

A sequence of JFDs observed on 16 July 1996 highlight this change of tilt (Figure 5.2). Each JFD was separated in time by about 15 minutes and each leg took about 15 minutes to fly. No corrections for nonstationarity of the boundary layer between flight legs has been applied. This example is typical of JFDs measured at various heights during BLX96, the positive slope for the leg near the surface is obvious, as is the negative slope near the mixed layer top. In this case, the middle leg seems to still have a positive tilt, but there is some evidence of a tail reaching towards warmer and dryer conditions. Figure (5.2) suggests that the lower-altitude JFDs might also have a smaller kurtosis (i.e. it is not as peaked) than the upper-level legs¹. However, this trend disappears when all days are considered.

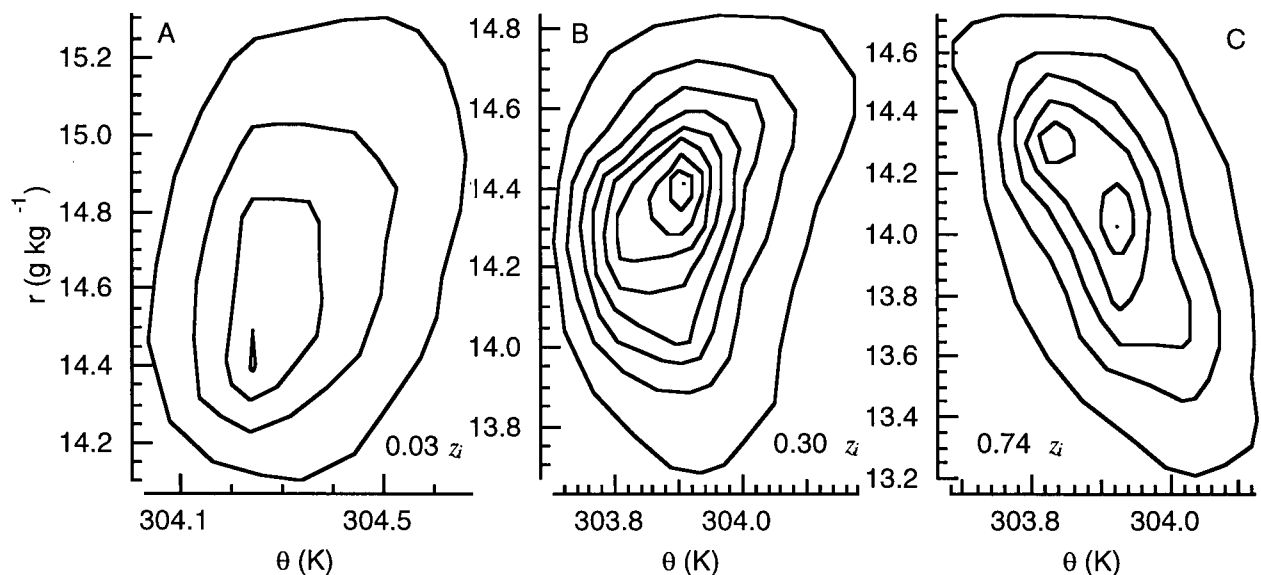


Figure 5.2. Sequence of three JFDs of θ vs. r at three different heights: (A) $0.03 z_i$, (B) $0.30 z_i$, and (C) $0.74 z_i$ measured on 16 July 1996. The outside contour indicates a normalized frequency of 0.005, and the contour interval is 0.01.

¹A Gaussian distribution has a kurtosis of 0, using the Gaussian-relative kurtosis definition of Press et al. (1992)

5.4 Previous methods

As mentioned in the introduction, two methods have been suggested to parameterize JFDs in the boundary layer. WM fit joint-Gaussian JFDs to JFDs of an arbitrary scalar and w generated by a LES model. They used three parameters to describe their JFDs: the measured correlation between the scalar and w , the standard deviation of the scalar, and the standard deviation of w . Their method is statistical and did not offer a physical explanation for the tilt of the JFD. While they constructed JFDs of a scalar vs. w , their mathematical techniques are also valid for JFDs of θ vs. r . Throughout the rest of this dissertation, this method will be called the statistical method.

SSZ introduced a physically based method to fit joint Gaussian JFDs to JFDs of θ_v vs. z_{LCL} measured in the surface layer during HAPEX. They introduced two new axes, which, while not geometrically orthogonal, are physically orthogonal. They related the slope of one axis to the Bowen ratio (B), and the slope of the other axis to a variable they called the solar forcing (θ_F). They defined θ_F as a fictitious temperature perturbation which accounts for the total net-radiative flux at the surface (Q^*) in a bulk flux parameterization

$$Q^* = \rho_{air} C_p w_T \theta_F, \quad (5.4)$$

where ρ_{air} is the density of air, C_p is the specific heat of air, and w_T is a turbulent transport velocity (Stull 1994). SSZ indicated that θ_F can be a function of surface albedo, land-use patterns or partial shading by scattered or broken clouds. They proposed that if θ_F and B are known, one could predict surface-layer JFDs. This method will be called the B - θ_F method. In Appendix C SSZ's equations are converted from their θ_v vs. z_{LCL} framework to the θ vs. r framework used in this dissertation.

Both the statistical and the B - θ_F methods are tested here against observations from BLX96. The observed variances and correlations from BLX96 were used to construct JFDs using the statistical method. Maximum-likelihood methods, like those used by SSZ, were used to find the two best-fit slopes of the axes of the B - θ_F method. Both methods were applied to data from 65 horizontal flight legs from BLX96. Figure 5.3 shows an example of the best-fit statistical

and $B-\theta_F$ methods against an observed JFD from one near surface leg on 13 August 1996 ($z/z_i = 0.04$). This leg was flown near 11:00 LST, and 44,050 points were used to construct the JFD. In both cases the modeled peak frequency is too small. This occurs because the Gaussian distribution it is not peaked enough. In this example, the observed kurtosis of r was 0.99, while the kurtosis of θ was 1.7. The observed JFDs are also skewed along their axes. It is impossible for a joint Gaussian JFD to fit the skewness because Gaussian distributions are symmetric.

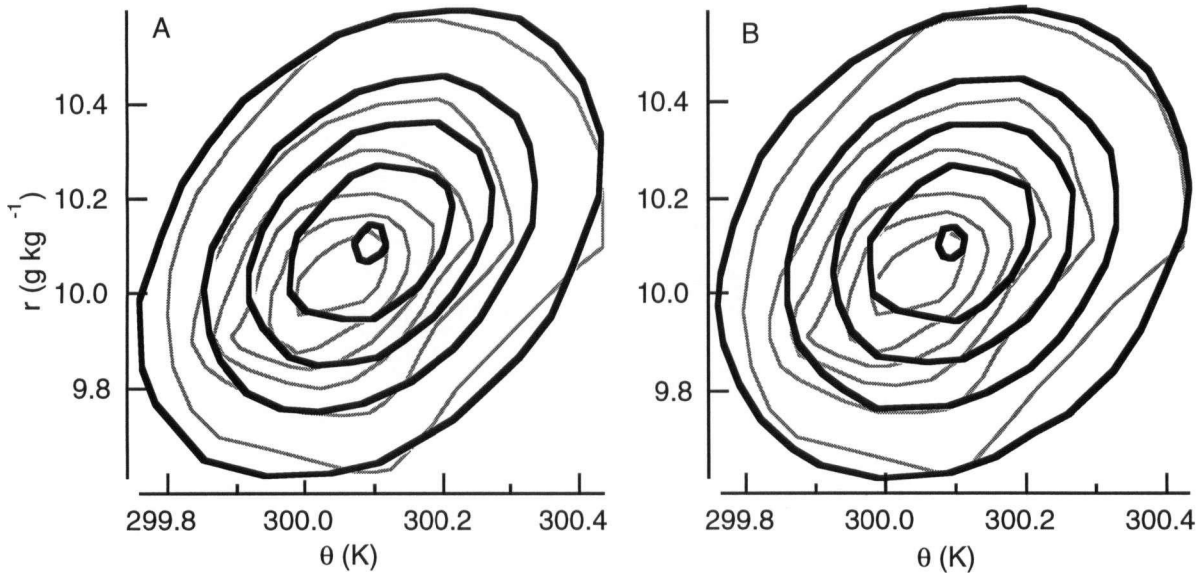


Figure 5.3. Observed JFD (thin lines) and sample fits of (A) the statistical method and (B) the $B-\theta_F$ method (thick lines) for a near surface leg at 11:00 LST on 13 August 1996. The first contour indicates a normalized frequency of 0.005 for both the observed JFD and the fit JFD, and the contour interval is 0.01.

SSZ proposed a simple measure of the goodness of fit. They defined the total error as:

$$err = \sum_j |\hat{f}_{obs,j} - \hat{f}_{fit,j}|, \quad (5.5)$$

where $\hat{f}_{obs,j}$ is the normalized frequency observed for the j th bin, and $\hat{f}_{fit,j}$ is the normalized frequency from the j th bin of the parameterization. The error of both methods was computed for all legs. The errors computed for the $B-\theta_F$ method are larger than the error of the statistical method. The average error for the statistical method was 0.34, while the error for the $B-\theta_F$

method was 0.39. SSZ suggested equations to predict the slope of both the θ_F and B axes. Poor agreement was found between slope predicted by SSZ's theory and the best-fit B and θ_F axes found using the maximum-likelihood method (Figure 5.4). As shown in Appendix C, SSZ's theory gives a constant θ_F slope in θ vs. r space, while the maximum-likelihood best fit suggests a weak dependence on B (Figure 5.5). This behavior may occur because the two maximum-likelihood axes are not independent. Two shortcomings of the maximum-likelihood method were noted for the BLX96 data: (1) the predicted slopes of the axes always had the same sign, and (2) both of the maximum-likelihood fits have some dependence on B . The slopes of these lines should be independent of each other, and the θ_F slope should be independent of B . These results suggest that the two slopes found by the maximum-likelihood method are not the θ_F and B axes desired by SSZ. The theoretical slopes suggested by SSZ will be explored more carefully in the next chapter.

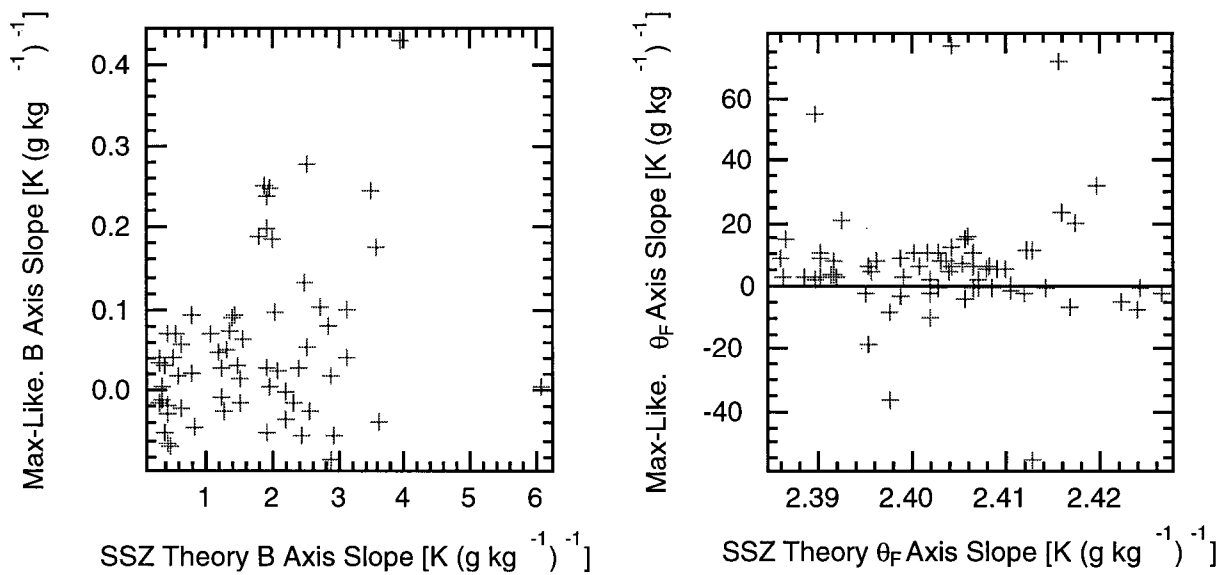


Figure 5.4. Maximum likelihood B axis slope vs. SSZ theoretical B axes slope and maximum likelihood θ_F axis slope vs. SSZ theoretical θ_F axis slope vs. for all BLX96 legs.

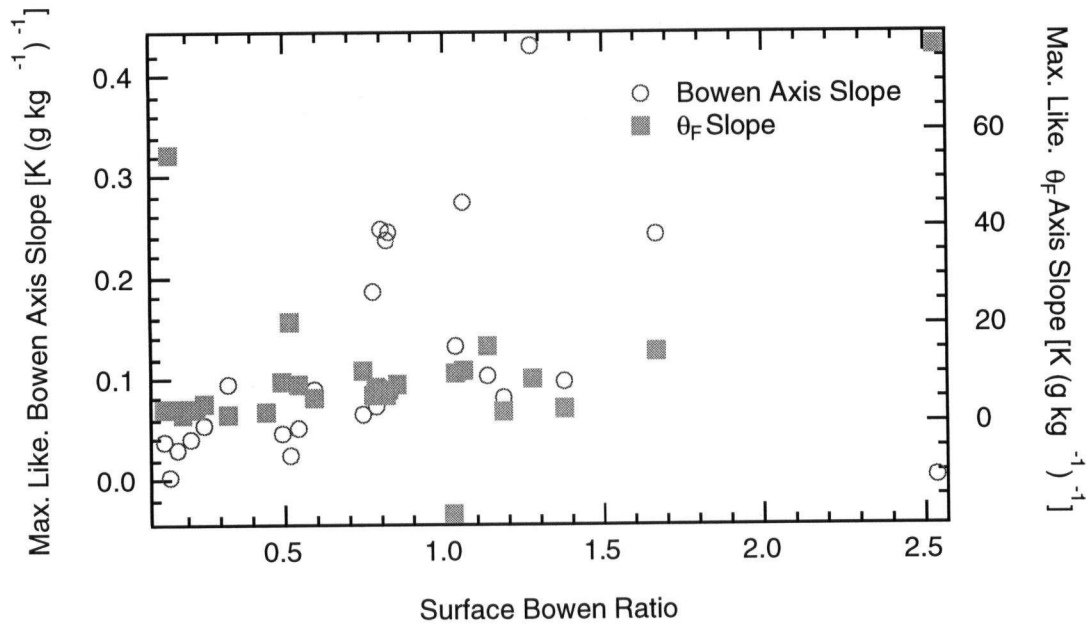


Figure 5.5. Maximum likelihood B axis slope (circles, left axis) and maximum likelihood θ_F axis slope (squares, right axis) vs. observed surface B for all BLX96 near surface legs.

5.5 Two new methods

5.5.1 Sub-JFD method

Next, two new methods to represent the JFDs in the convective boundary layer are introduced. Each method is based on physical processes that generate JFDs. In the first method, parcels in the mixed layer are divided into three different groups (Figure 5.6). One family of parcels are “updrafts”. These parcels have thermodynamic properties similar to those near the surface, are generally warmer and more moist than the mixed-layer mean, and contribute significantly to the turbulent flux. Another group, “downdrafts”, is made up of parcels of sinking air. Lower in the mixed layer, most of these parcels are cooler than the environment and are sinking due to buoyancy effects. At all altitudes, others are sinking because of pressure forces. These parcels also contribute to the turbulent flux. The largest group of parcels are those that are not part of an updraft or downdraft. These parcels have resided and been mixed in the mixed layer for some time, and have thermodynamic properties that are clumped around the leg mean values.

These will be called “environmental” parcels.

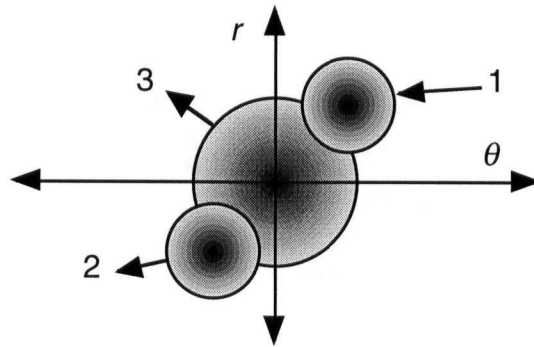


Figure 5.6. Sketch showing parcel families for: (1) updrafts, (2) downdrafts and (3) environment.

A number of other researches have investigated the convective boundary layer by locating coherent structures (Lenschow and Stephens 1980; Nicholls and LeMone 1980; Greenhut and Khalsa 1982, 1987; Grossman 1984; Khalsa and Greenhut 1985; Young 1988; Williams and Hacker 1992), and their exact methodology used to locate drafts was described in Chapters 2 and 4. The sub-JFD method will be applied using separate Gaussian JFDs to represent the updraft, downdraft, and environmental distributions. These sub-JFDs will be added together to form a single JFD representative of the boundary layer. This method is appealing because it has the potential to account for the skewness, kurtosis, and multiple peaks found in observed JFDs. Unfortunately for this method it is difficult to parameterize these sub-JFDs because of the large number of variables that are needed. A second method is also proposed because of this major shortcoming (section 5.5.3).

An example of the mean thermodynamic properties of the updrafts, downdrafts and environment measured on 25 July is plotted in Figure 5.7. In this example, the mean updraft, downdraft and environment lie on a straight line or mixing line in θ vs. r space. This occurred for nearly all of the flight legs (Figure 5.8). Why? This behavior indicates the environmental portion is made of a mixture of air from the updrafts and downdrafts. This finding supports the

argument of Crum and Stull (1987) that much of the air in the mixed layer is a mixture of entrained air and surface-layer air. For some legs near the top of the mixed layer, the behavior seemed to break down. Perhaps, at higher levels the entrainment occurs on a shorter time scale than the turbulent mixing so that drafts do not lie on a straight line.

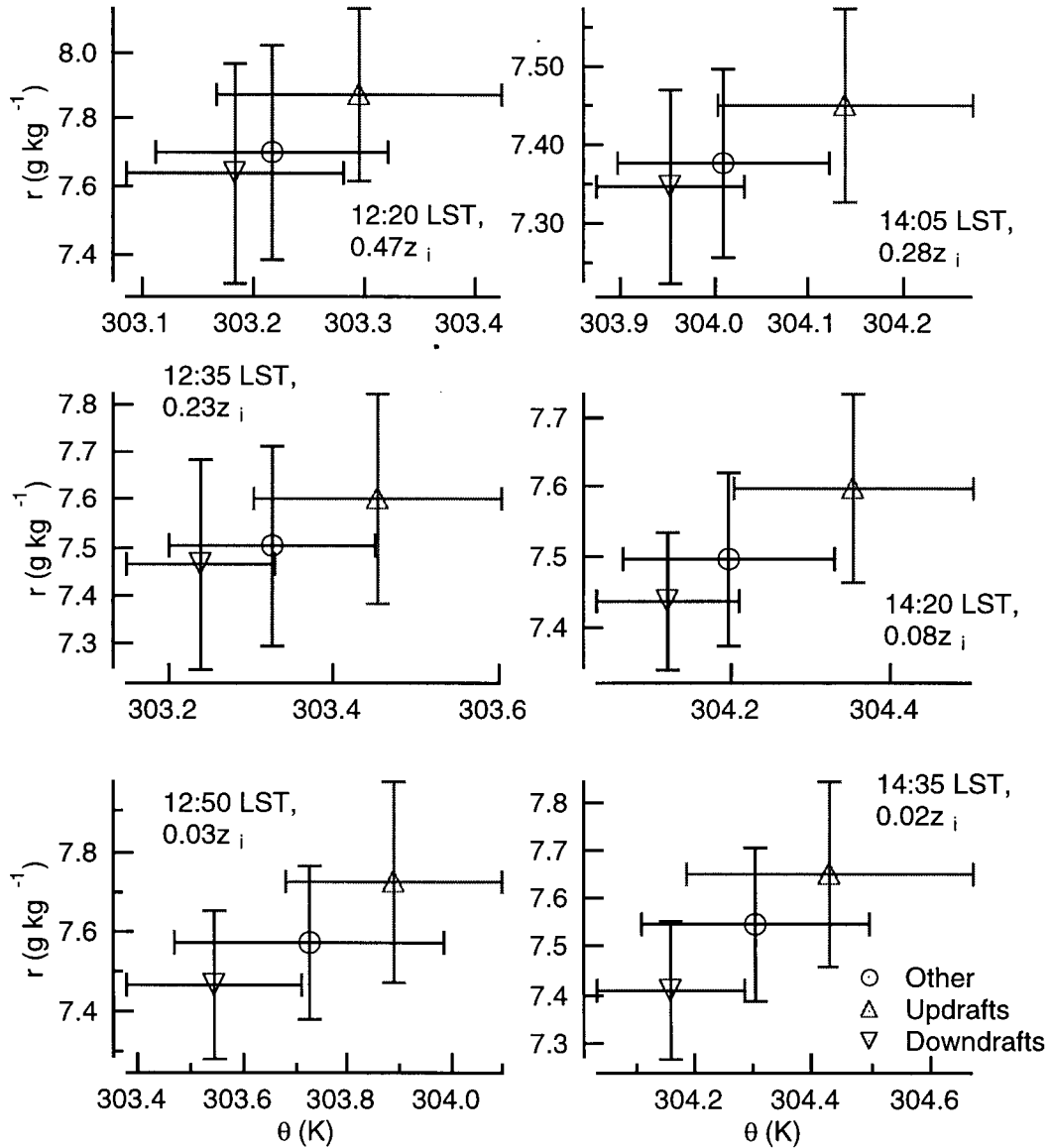


Figure 5.7. Plot showing updraft (upward pointing triangle), downdraft (downward pointing triangle) and environment means (circle) θ vs. r for six horizontal flight legs on 25 July. The error bars represent the standard deviations.

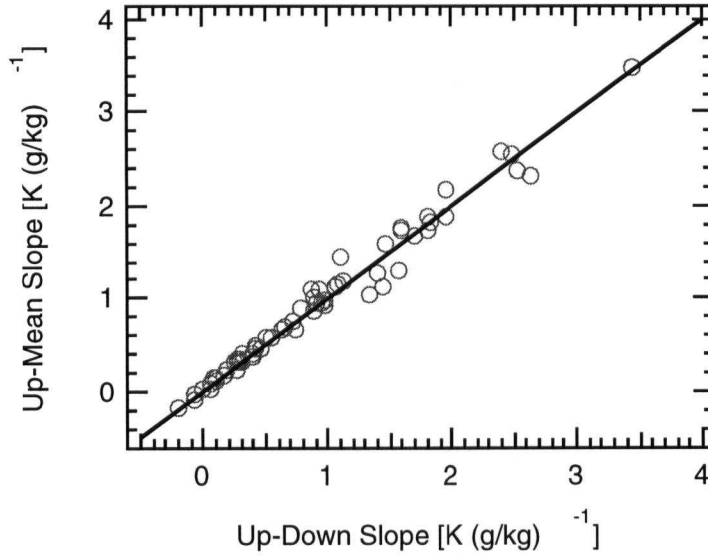


Figure 5.8. Slope of the line through the updraft and the leg mean $(\theta_u - \bar{\theta})/(r_u - \bar{r})$ vs. slope of the line through the mean of the updraft and downdraft $(\theta_u - \theta_d)/(r_u - r_d)$

As an aside, the fraction of updraft and downdraft air that is needed to produce the mixed-layer mean θ and r can also be computed. These fractions should not be confused with the fraction of each leg covered by drafts. Starting with the definition of the leg mean, $\bar{\theta}$ and \bar{r} , and ignoring the effect of the environment on the leg mean

$$\bar{\theta} = \frac{\tilde{f}_u \theta_u + \tilde{f}_d \theta_d}{\tilde{f}_u + \tilde{f}_d}, \quad \bar{r} = \frac{\tilde{f}_u r_u + \tilde{f}_d r_d}{\tilde{f}_u + \tilde{f}_d}, \quad (5.6)$$

where \tilde{f}_u is the fraction of the mean contributed by updraft air, \tilde{f}_d is the fraction of the mean contributed by downdraft air, θ_u and r_u are the average thermodynamic properties of the updraft, and θ_d and r_d are the average thermodynamic properties of the downdrafts. Equation (5.6) can be rearranged to form expressions for \tilde{f}_u and \tilde{f}_d given observed value of the boundary-layer mean and the draft means

$$\tilde{f}_u = \frac{\bar{\theta} - (\bar{r} \theta_d)/r_d}{\theta_u - (r_u \theta_d)/r_d}, \quad \text{and} \quad \tilde{f}_d = \frac{\bar{r} - \tilde{f}_u r_u}{r_d}. \quad (5.7)$$

These fractions are plotted in Figure 5.9 vs. z/z_i . While there is scatter in Figure 5.9, it appears that \tilde{f}_u decreases with height while \tilde{f}_d increases with height, as is expected. Near the surface,

both updraft and downdraft air contributed to the observed mean in about equal proportions. Higher in the boundary layer the fraction of downdraft air becomes dominate. The mean value of \tilde{f}_u is 0.4, while the mean value of \tilde{f}_d is 0.6.

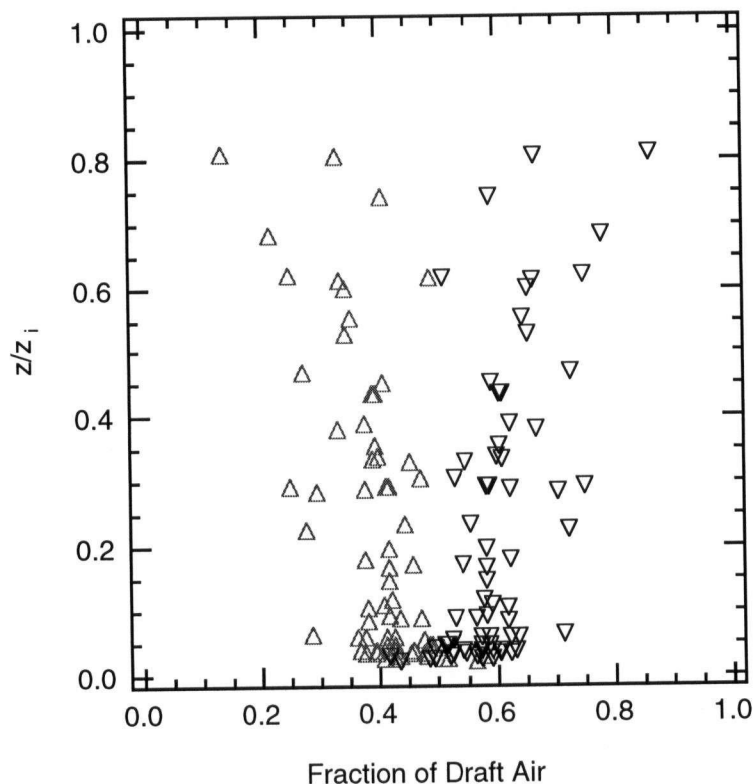


Figure 5.9. Plot of f_u (upward pointing triangles) and f_d (downward pointing triangles) vs. z/z_i for all BLX96 case study days.

5.5.2 Mixing-diagram method

Crum and Stull (1987) examined how distributions of r changed with height in the convective boundary layer. In the bottom half of the mixed layer, they found that the distribution of r was dominated by air that had risen from near the surface. Higher in the mixed layer they found evidence of unmixed entrained air, as well as air that was a mixture of both entrained air and surface layer air. This same reasoning can be applied to joint frequency distributions of θ vs. r .

In this conceptual model, the JFD of θ vs. r is viewed as a conserved-variable diagram, because both θ vs. r are conserved for dry adiabatic processes (Paluch 1979; Hanson 1984; Betts

1982, 1984, 1985; Betts and Albrecht 1987). The JFD computed from observations anywhere within the boundary layer is simply a large number of mixtures of air originating at the surface, air that has been entrained from the free atmosphere, and air that has resided in the boundary layer for some time. Thus, the JFD should stretch along a mixing line toward the thermodynamic properties of both the surface and the entrainment zone.

To investigate further, we can examine mixing diagrams of data collected from the slant ascent/descent soundings flown during BLX96. Figure 5.10 shows an example of three sequential soundings measured on 15 July. A similar plot was presented by Betts (1992). This plot is typical of mixing diagrams generated from the BLX96 soundings. On this particular day, θ and r of the free atmosphere did not change much with time, and are found at the lower-right quadrant of the diagram. On 27 July the mixed layer warmed with time (as shown by the shift of the mixed-layer points in the top left quadrant of Figure 5.10), dried some between both the first and second set of soundings and the second and third set of soundings (the mixed-layer points shifted down).

Other mixed-layer properties are apparent in Figure 5.10. Three different families of points are highlighted in Figure 5.10: mixed-layer points, entrainment-zone points and free-atmosphere points. The entrainment zone was determined from the slant ascent/descent soundings by locating the heights at which there were large jumps in the value of r . These large changes in r are caused by dry free-atmosphere air intruding down into the moist convective boundary layer. This type of identification is relatively easy with aircraft slant soundings, which pass through a large horizontal distance (approximately 70 km during BLX96) and thus intersect many thermal circulations. It would be more difficult with balloon soundings that drift along with a single thermal, and thus give effectively only a point sample. The points in the entrainment zone should lie on a mixing line between the free atmosphere and the mixed-layer mean. That was the case for nearly all BLX96 soundings. Surface-layer points are not highlighted in Figure 5.10. For flight safety reasons, the soundings flown during BLX96 did not go low enough to capture much of the superadiabatic surface layer. Because there were no observations of surface-layer properties an additional

assumption is needed. We assume that the mean properties of the observed updrafts lie on the mixing line that passes through the surface point on the mixing diagram. Therefore, these updraft properties will be used as a proxy for the surface layer properties.

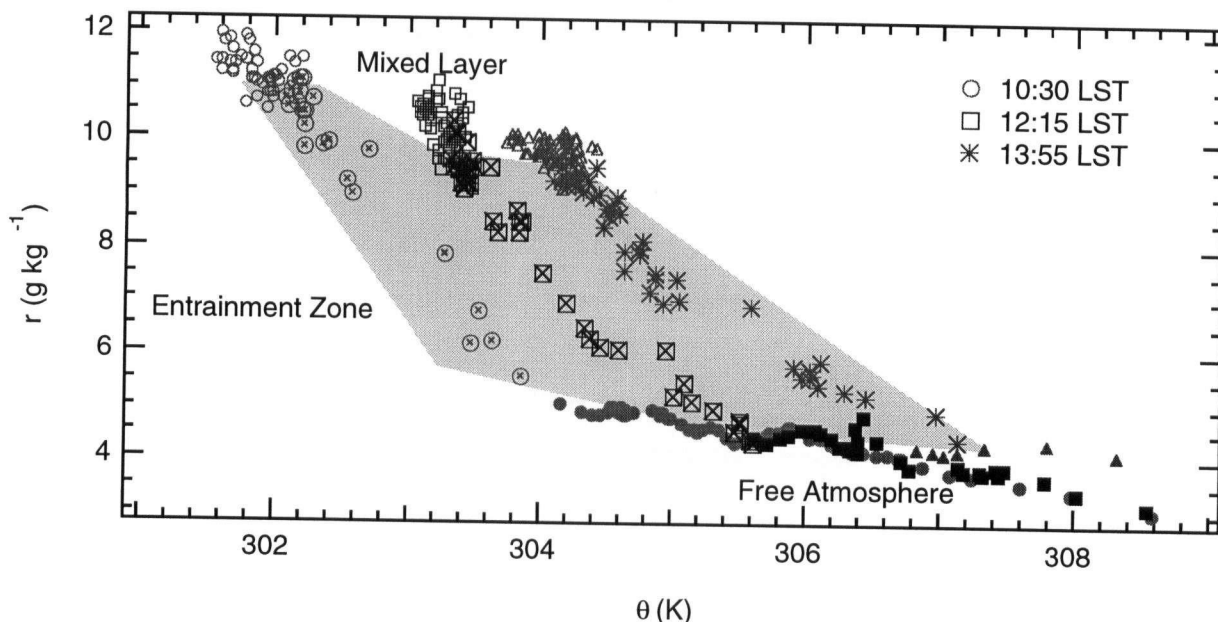


Figure 5.10. Mixing diagrams for the three sequential soundings on 15 July. Each symbol represents a block average over a depth of 20 m. The open symbols correspond to the mixed-layer values, circles with crosses, squares with crosses and asterisks correspond to the entrainment-zone values, and the filled symbols correspond to the free atmosphere. Shading highlights observations that are part of the entrainment zone.

The mixing diagram method has several advantages. There are fewer variables needed to parameterize the JFDs. This method also provides a convenient framework for examining how the boundary layer changes with time. The thermodynamic state of the mixed layer can be viewed as a time-dependent mixing process. If boundary-layer mixing were instantaneous, then all the observations would be grouped along a single mixing line connecting the surface and the free atmosphere. Instead, a unique shape is observed where the JFD is stretched towards warm and generally moist conditions near the surface, and warm and dry conditions aloft (Figure 5.11). We can use this diagram to look at different processes in the boundary layer (Betts 1984, 1992; Culf 1994). For days with quiescent weather and ample surface heating, the surface layer will warm

with time during the day. This surface heating and mixing will pull the mixed-layer distribution towards the surface point. At the same time, entrainment from the free atmosphere will also pull mixed-layer points towards the thermodynamic properties of the free atmosphere. Advection can also play a role, pulling the boundary-layer points in a third direction. The exact thermodynamic state of the mixed layer is due to this tug-of-war between surface and entrainment processes. Betts (1984) derived a vector equation for how the fluxes and advection can influence the thermodynamic state of the atmosphere.

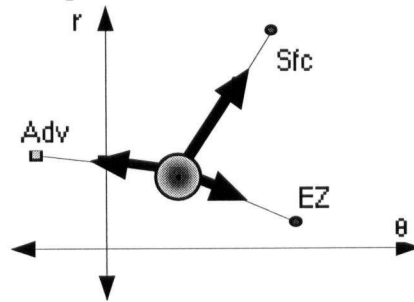


Figure 5.11. θ vs. r mixing diagram. The large circle represents the mixed-layer mean, the small circles represent the surface (Sfc), entrainment zone properties (EZ), and the square represents the advection (Adv). The large arrows indicate the “direction” that the different processes pull on the mixed layer mean, as well as the slope of the surface and the entrainment zone axes.

A slightly different approach to describe how the mixed layer mean θ and r change can be used for the special case of no advection. The budget equations for this special case can be written for both potential temperature, $\partial\theta/\partial t = -\partial\overline{w'\theta'}/\partial z$, and for mixing ratio, $\partial r/\partial t = -\partial\overline{w'r'}/\partial z$.

These equations can be combined and integrated over the mixed-layer depth to yield

$$\left(\frac{\partial r}{\partial t}\right)\left(\frac{\partial t}{\partial\theta}\right) = \frac{\partial r}{\partial\theta} = \frac{-\partial\overline{w'r'}}{-\partial\overline{w'\theta'}} = \frac{(\overline{w'r'}_{z_i} - \overline{w'r'}_{sfc})}{(\overline{w'\theta'}_{z_i} - \overline{w'\theta'}_{sfc})}. \quad (5.8)$$

Equation (5.8) indicates that changes in the mixing diagram are a function of only the flux divergence through the layer of interest; the thickness of the layer is not important. This equation can be rewritten as

$$\frac{\partial r}{\partial \theta} = \frac{\overline{w r}_{sfc}(1-R_r)}{\overline{w \theta}_{sfc}(1-R_\theta)} = \frac{C_p(1-R_r)}{L_v B(1-R_\theta)}, \quad (5.9)$$

where R_r and R_θ are the ‘‘Ball’’ ratios (Ball 1960) of the entrainment to surface fluxes, B is the Bowen ratio, C_p is the specific heat of air, and L_v is the latent heat of vaporization.

5.5.3 Application of the mixing diagram method

SSZ define a transform to convert from θ and r to a coordinate system defined using the slopes of their B and θ_F axes. These transformed values are used to create JFDs based on these new axes. Their definitions can be used to convert θ and r data into a coordinate system, c and m , based on slope (γ_{sfc}) of the surface axis and the slope (γ_{ez}) of the entrainment-zone axis (Appendix C).

$$c = \gamma_{ez} \left(\frac{\theta - \gamma_{sfc} r}{\gamma_{ez} - \gamma_{sfc}} \right) \text{ and } m = \frac{\theta - \gamma_{ez} r}{\gamma_{sfc} - \gamma_{ez}}, \quad (5.10)$$

where c has units of temperature and m has units of mixing ratio. The values of c and m are projected from the surface axis and entrainment zone axis onto the θ and r axes. A joint Gaussian distribution, framed in γ_{sfc} vs. γ_{ez} coordinate system and neglecting the correlation between c and m , takes the form

$$f(m, c) = \frac{1}{2\pi\sigma_m\sigma_c} \exp \left\{ -\frac{1}{2} \left[\left(\frac{m}{\sigma_m} \right)^2 + \left(\frac{c}{\sigma_c} \right)^2 \right] \right\}. \quad (5.11)$$

Unfortunately, (5.11) is not directly comparable to a joint Gaussian distribution, such as (5.3), in θ and r because the transform (5.10) is not area conserving. An area correction factor is derived in Appendix D that can be used to make (5.3) and (5.10) directly comparable.

It is also informative to look at distributions of c vs. m measured during BLX96 (Figure 5.12). Surprisingly, some of these distributions are correlated. If the two axes were picked correctly, we would expect that JFDs in c vs. m space would have no correlation. However, there is some correlation introduced by (5.10) (it is derived in Appendix E). This introduced correlation can best explained by looking at three idealized limiting cases: one where θ and r are

not correlated (sketched in Figure 5.13), a second where the new axes give a perfect fit, in other words, all the observations lie on either the surface or entrainment zone axis, in other words, all observations are mixtures of either mixed layer and free atmosphere air or mixed layer and surface-layer air (Figure 5.14a), and a third case where the surface and entrainment-zone axes are orthogonal to each other (Figure 5.14b). For the case where θ and r are not correlated the transform introduces a correlation. The JFD plotted in θ vs. r space would appear to be an oval or a circle. Remember, two of the quadrants defined by the axes contribute a positive value to the correlation and two quadrants contribute a negative value to the correlation. If the axes are shifted, such as occurs when the coordinates are shifted, the fraction of the JFD which make positive and negative contributions would change, and the correlation would become nonzero. In the perfect-fit case, all the observations lie on the new axes, so that any point only contributes to c or m and the correlation is zero. For the case where surface and entrainment-zone axes are orthogonal, the positive and negative areas in the transformed space cancel.

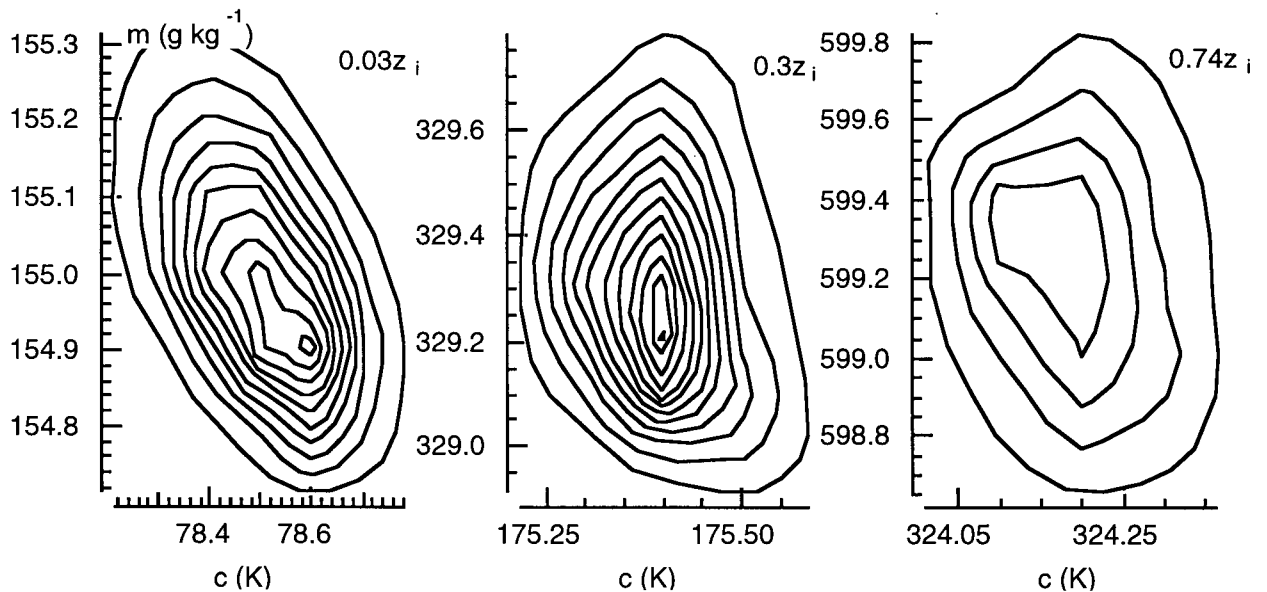


Figure 5.12. Sequence of the JFDs of c vs. m at three different heights ($0.03z_i$, $0.3z_i$, and $0.74z_i$) measured on 16 July 1996, the same times as the JFDs shown in Figure 5.2. The first contour marks a normalized frequency of 0.01 and the contour interval is 0.01.

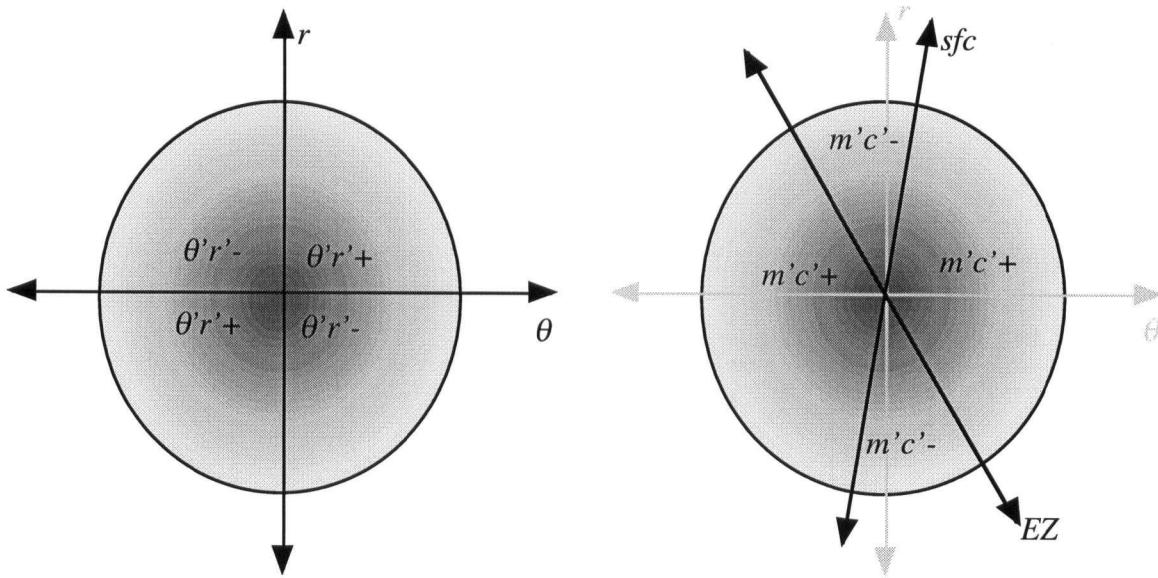


Figure 5.13. Sketch of a case where the JFD (shaded circle) is uncorrelated in θ vs. r (left), but is correlated in c vs. m space because of the larger area contributing positive values (right).

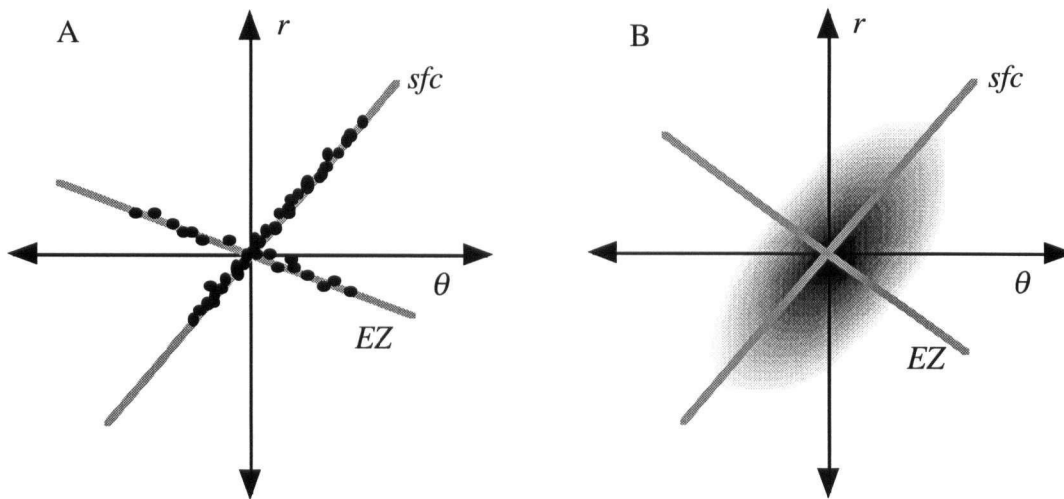


Figure 5.14. Sketch of two cases where a JFD (points or shading) is correlated in θ vs. r space, but is not correlated in c vs. m space, (A) perfect fit and (B) orthogonal surface and entrainment zone axes.

The observed JFDs from 16 July (Figures 5.2 and 5.12) show this behavior very well. The lowest leg has very little tilt when plotted in θ vs. r space (Figure 5.2), especially if one

focuses on the larger frequencies near the mean. For this JFD $\rho_{\theta,r} = 0.25$. When data from the lowest leg is plotted in c vs. m space there is a definite tilt to the JFD. For this transformed JFD $\rho_{c,m} = -0.58$. As shown in Appendix E, the contribution to $\rho_{c,m}$ by the coordinate transformation can be separated from that due to the covariance of θ and r . For this leg the contribution from the coordinate transformation is -0.48 , or about 84% of the correlation in c vs. m space. This behavior is not problematic because we are only concerned with results in θ vs. r space and in the next section it will be shown that $\rho_{\theta,r}$ calculated from the best-fit JFDs is very close to the observed value of $\rho_{\theta,r}$.

5.6 Results

JFDs were fit to 65 horizontal flight legs from BLX96. For this comparison the observed mean, standard deviation, and correlation were used to apply the statistical method. This method will be used as the control method, and the $B-\theta_F$, sub-JFD, and mixing-diagram methods will be compared to the statistical method. Maximum-likelihood methods were used to find the best-fit B and θ_F axes needed by the $B-\theta_F$ method. The observed updraft, downdraft and environment mean, observed standard deviations, correlations, and frequencies were used to fit the sub-JFD method. Inferred surface-layer properties and observed entrainment-zone properties were used to provide the data for the mixing-diagram method.

A sample fit using each method is shown in Figure 5.15. Each method seems to do a good job. The sub-JFD method is able to capture some of the skewness. However, in each case the peak frequency is too small. An additional problem is evident in the $B-\theta_F$ fit. Two sets of axes are shown in the plot, one estimated by the maximum-likelihood methods, the other predicted by the theory suggested by SSZ. The agreement between the two is poor [as reported in section 5.5 (Figure 5.4)].

The error between the different methods and observations found using (5.5) is shown in Figure 5.16. One additional method is included in this plot for comparison, using the statistical

method, but assuming that $\rho_{\theta,r} = 0$ (no tilt to the JFD). From the plot it appears that the other methods are superior to this simplistic fit. The mixing-diagram JFDs did not do as well as the sub-JFD method or the $B-\theta_F$ (Figure 5.16). The performance of this method should not be considered discouraging, because the tilt of the major and minor axes was based strictly on the new theory, not on a statistical best fit. The $B-\theta_F$ method did a good job (Figure 5.16). One would expect the quality of the fit to be good, given that the maximum-likelihood methods were used to find the best-fit axes. However, as shown earlier in this chapter, the slopes predicted by the surface layer theory were different than those predicted by the maximum-likelihood methods. The sub-JFD method did the best job (Figure 5.16). In most cases the error associated with the sub-JFD method was smaller than the error of the statistical fit. The better fit is not surprising because the skewness and kurtosis can be represented by this method. However, as described earlier, this method requires many more parameters than the other methods.

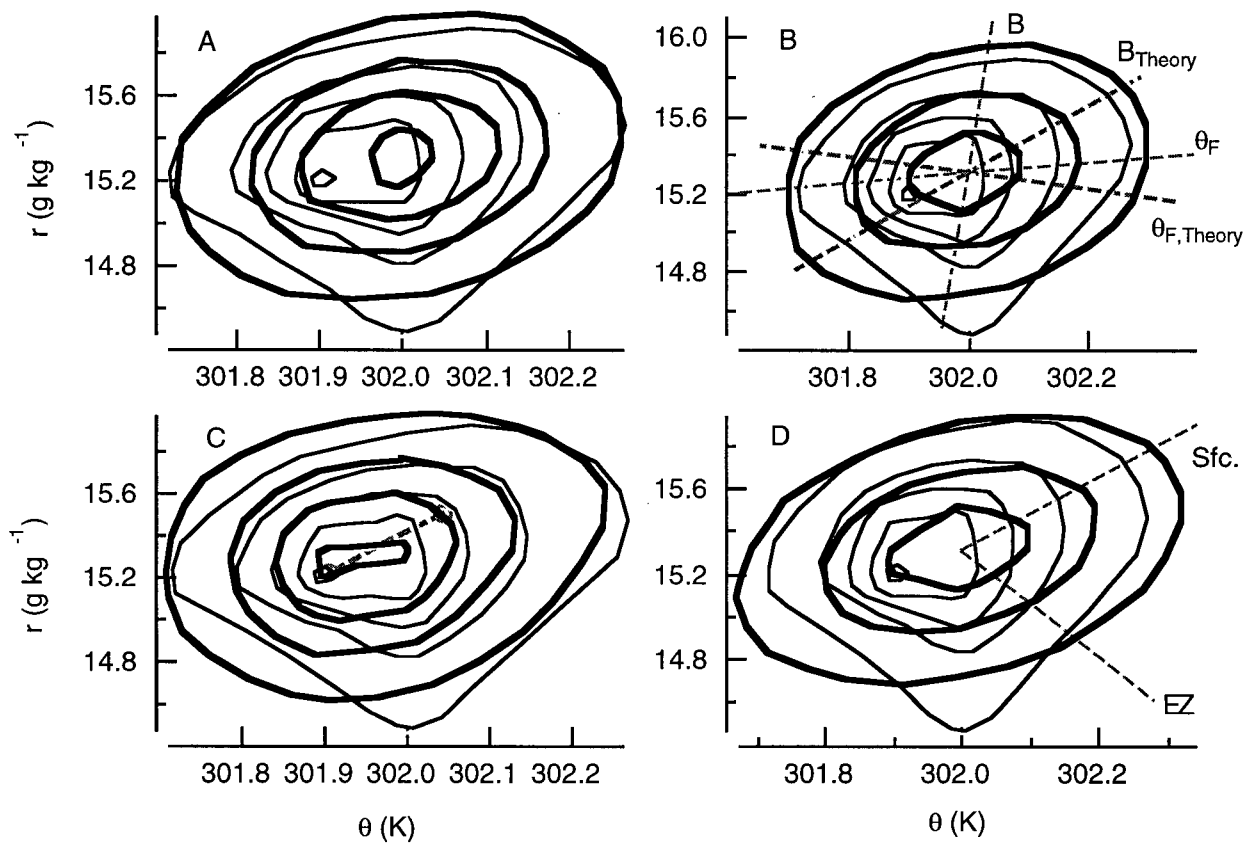


Figure 5.15. Plot of observed (thin lines) and predicted JFDs (heavy lines) for: (A) the best fit Gaussian, (B) best-fit $B-\theta_F$ axes (thin broken lines), theory predicted $B-\theta_F$ (heavy broken lines), (C) sub-JFD axis (broken lines) with updraft and downdraft means marked with an open circle, and (D) surface-entrainment zone axes (broken lines). All plots are based on data from the leg on 2 August (11 LST, $z/z_i=0.09$). In each case the first contour marks a normalized frequency of 0.005 and contour interval is 0.01.

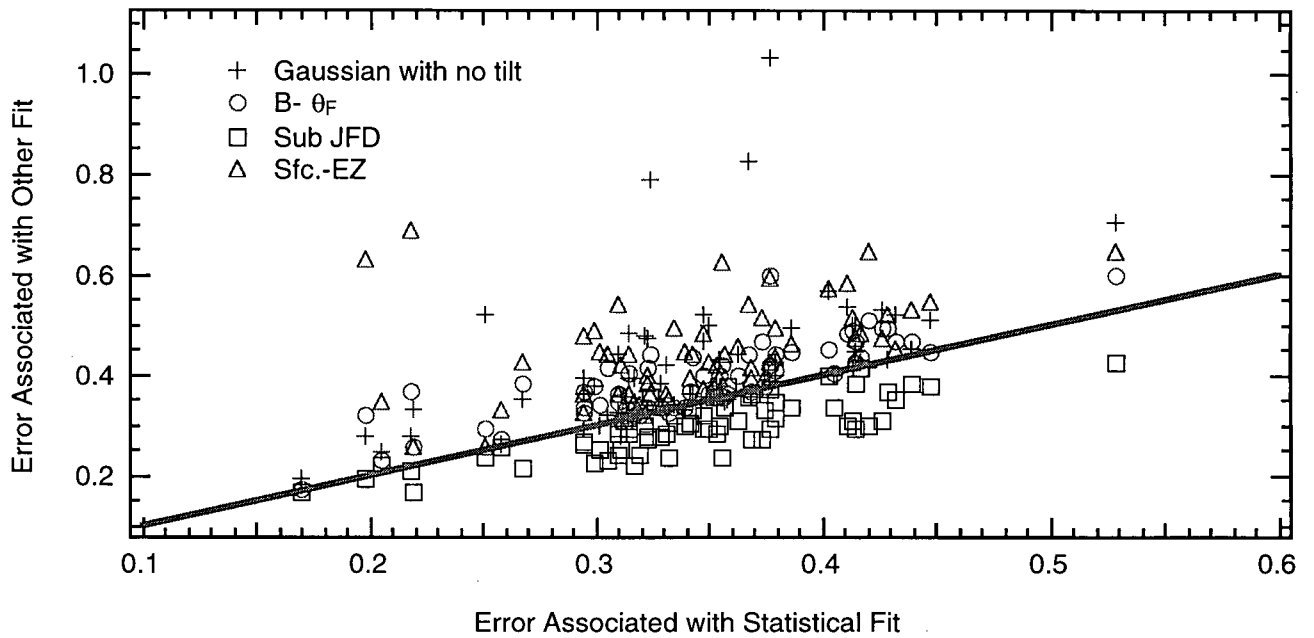


Figure 5.16. Error associated with a statistical fit with no tilt (crosses), error associated with the $B-\theta_F$ method (circles), error associated with the sub-JFD method (squares), and error associated with the surface-entrainment zone method (triangles) vs. error associated with the statistical fit. Points below the diagonal line have less error than the control method of statistical fit.

5.6.1 Correlation of observed and mixing-diagram JFDs

In section 5.5, the correlation between θ and r ($\rho_{\theta,r}$) and c and m ($\rho_{c,m}$) was discussed. While the coordinate transform introduces an extra correlation in c vs. m space, this extra correlation is not apparent when the mixing-diagram JFDs that were fit in c vs. m space are plotted in θ vs. r space. Figure 5.17 shows a plot of $\rho_{\theta,r}$ calculated from the observations vs. $\rho_{\theta,r}$ calculated from the best-fit Gaussian JFDs. The agreement between the two is quite good, suggesting that the mixing-diagram theory does a good job predicting $\rho_{\theta,r}$. For cases where $\rho_{\theta,r}$ calculated from the BLX96 observations and $\rho_{\theta,r}$ from the mixing-diagram JFDs are both negative, $\rho_{\theta,r}$ predicted by the mixing diagram is slightly smaller than the observed. It is not clear why this is the case, but a number of them occur for legs near the top of the boundary layer. This

could be related to errors in the entrainment-zone slope, which are interpolated to the time of the relevant flight leg.

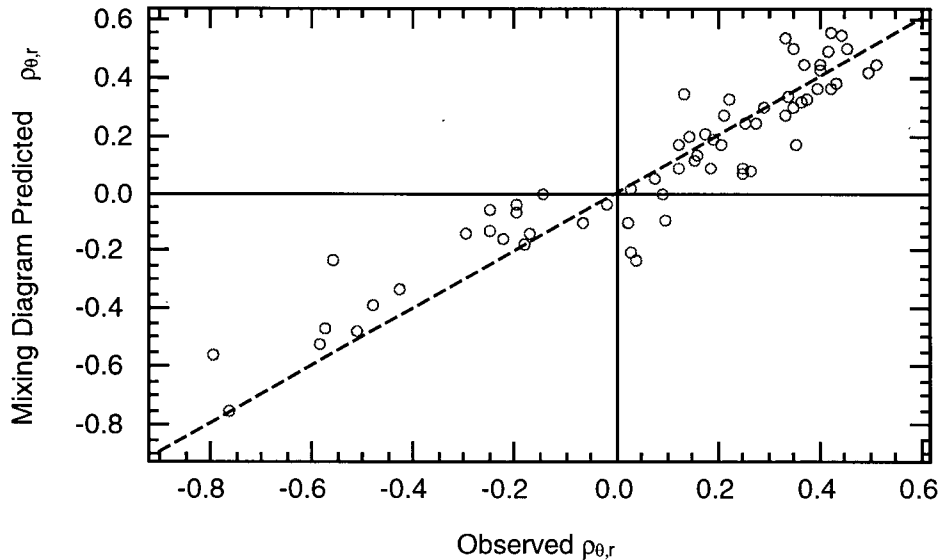


Figure 5.17. Best-fit $\rho_{\theta,r}$ vs. observed $\rho_{\theta,r}$ for all BLX96 flight legs. The dashed line is the 1:1 line.

There are five cases where the observed $\rho_{\theta,r}$ and mixing-diagram predicted $\rho_{\theta,r}$ have different sign (Figure 5.17). This occurs for cases when the observed JFD has a complicated shape (A, B and C in Figure 5.18), or a more simple shape (D and E in Figure 5.18). In either case, the observed $\rho_{\theta,r}$ is rather small for each of the five cases (less than 0.1, Table 5.1). The three cases with the complicated shape were measured on 15, 22, and 25 July. For cases A and B, it appears that a JFD with a negative tilt is not a bad fit, especially if one focuses only on the region of the JFD with high normalized frequency. Case C has a tail reaching towards a warm and dry values, which may give rise to the small negative value of $\rho_{\theta,r}$ (-0.11) predicted by the mixing-diagram method. The observed JFDs for cases D and E seem to have a simple shape, and both the positive values of $\rho_{\theta,r}$ for the observed JFDs and the negative values of $\rho_{\theta,r}$ for the fit JFDs are small and may not be significant (less than 0.1 in magnitude). These errors will be ignored because the absolute error in $\rho_{\theta,r}$ is small and may not be statistically significant

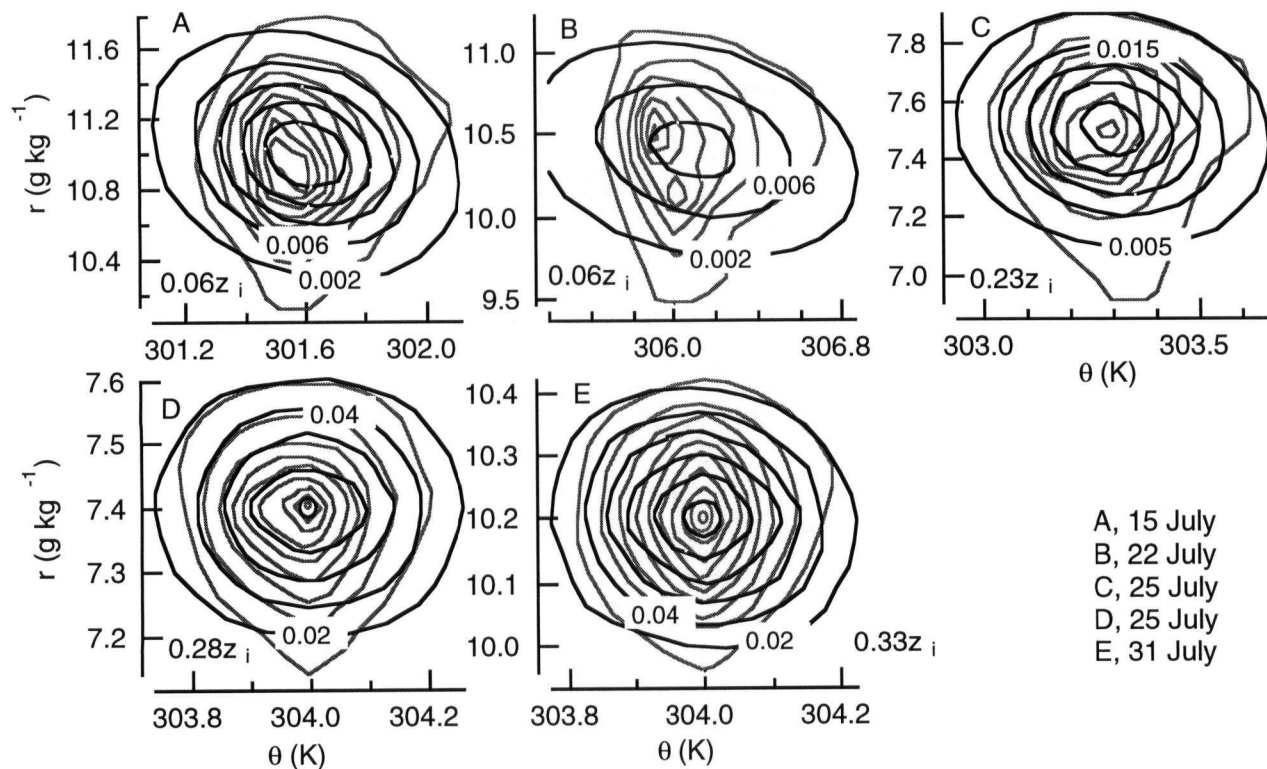


Figure 5.18. Observed (gray lines) JFDs and best-fit surface-entrainment zone JFDs (black lines) for the five cases where the observed $\rho_{\theta,r}$ had an opposite sign than the best-fit $\rho_{\theta,r}$. The normalized frequency represented by the first contour and the second contour are marked and the contour spacing is constant. The contour interval for the observed JFDs is the same as for the best-fit JFDs.

Table 5.1. Case (as described in section 5.7.1), date, time, height, observed $\rho_{\theta,r}$ and predicted $\rho_{\theta,r}$ for the case study days were the observed and predicted $\rho_{\theta,r}$ were of different sign.

Case	Date	Time (LST)	Height (z/z_i)	Observed $\rho_{\theta,r}$	Predicted $\rho_{\theta,r}$
A	15 July	10:15	0.06	0.03	-0.21
B	22 July	11:15	0.06	0.04	-0.23
C	25 July	13:30	0.23	0.03	-0.11
D	25 July	14:00	0.28	0.10	-0.01
E	31 July	14:10	0.33	0.10	-0.10

5.7 Conclusions

JFDs of θ vs. r measured during BLX96, at heights ranging from 0.02 to $0.8 z_i$ in the daytime convective boundary layer, were described. It was found that JFDs observed near the surface had a positive tilt to their major axis, while those higher up had a negative tilt. This negative tilt was attributed to entrainment processes in the boundary layer.

Two new methods, both based on physical processes in the boundary layer, were suggested to explain the magnitude of the observed tilt of JFDs of θ vs. r . One method was based on adding three different sub-JFDs. Each sub-JFD was made from air belonging to one of three categories: updrafts, downdrafts or the environment. The second method describes the JFDs in the mixed layer as mixtures of air from near the surface, from the entrainment zone and from the environment. The relationship of these three source regions was used to tilt the JFDs. The sub-JFD method was superior to any of the other methods used, but requires many more parameters to describe the distribution. The mixing-diagram method was not as successful as the sub-JFD, but requires fewer parameters.

The correlation between θ and r ($\rho_{\theta,r}$) calculated from the BLX96 data was compared to $\rho_{\theta,r}$ calculated for mixing-diagram JFDs. The agreement seems to be good. There were five cases

out of 65 total where $\rho_{\theta,r}$ calculated from the observed data was of opposite sign from the $\rho_{\theta,r}$ of the best-fit JFDs. These cases were examined more closely and it appears that a negative value of $\rho_{\theta,r}$ is not necessarily a bad estimate. In the next chapter methods to parameterize both types of distributions will be introduced.

Chapter 6: Parameterization of JFDs of Potential Temperature and Water-Vapor Mixing Ratio

6.1 Introduction

The goal of this chapter is to test several parameterizations for the JFDs and to pick the best one(s) for use in a later chapters to predict boundary-layer cumuli. In Chapter 5, the tilt of JFDs measured in the daytime convective boundary layer was related to physical processes in the boundary layer. Two older methods were reviewed, the statistical method (Wyngaard and Moeng 1992) and the $B - \theta_F$ method (Schrieber et al. 1996). Two new methods, one based on sub-JFDs and another on mixing processes, were introduced. In this chapter, the parameterization of JFDs using each of the four methods will be discussed. By parameterizing the JFDs, the results can be incorporated into climate and weather-forecast models to describe subgrid heterogeneity and cumuli (Chapter 8). The variables that must be parameterized for each method are listed in Table 6.1. Those variables for which a physically based parameterization or a similarity parameterization will be developed are identified.

There is little theoretical guidance for a parameterization of the statistical method. Many authors have shown that σ_θ/θ_* and σ_r/r_* are well behaved functions of height when normalized by the appropriate scaling variable (e.g. Willis and Deardorff 1974; Lenschow and Stephens 1980; Khalsa and Greenhut 1987). In Chapter 3 a new moisture scaling variable, $r_{*,new}$, was introduced based on the moisture fluxes at both the top and bottom of the mixed layer. It was shown in Chapter 4 that the correlation of θ and r is also a function of height for BLX96 (although this relation may not be universal). These expressions can be used to parameterize the statistical method. Attempts to find an expression relating the correlation between θ and r to Bowen Ratio (B) were unsuccessful.

Schrieber et al. (1996) argue that two different factors cause the tilt of JFDs of θ_v vs. z_{LCL} . They hypothesize that variations in both B and the total energy supplied at the surface lead to the tilt of the JFD. They called their new axes the B and θ_F axes. In Chapter 5, their equations

predicting the slope of these two axes were compared to the best-fit maximum-likelihood axes.

There was a relationship between their B axis and the predicted slope, but the relationship was not as expected. They seem to be missing some important physical processes. There did not appear to be a relationship between the maximum-likelihood solar forcing axis and the theoretical axis.

In this chapter, details of the parameterization of the sub-JFD and mixing-diagram method will be explained. Similarity expressions will be derived for quantities for which a physically based parameterization is not developed. Finally, the goodness of fit of each of the parameterization methods will be shown.

Table 6.1. List of methods used to parameterize JFDs, the variables needed for the parameterization and the basis for the parameterization (physical or similarity theory). The symbol, γ , indicates the slope of an axis indicated by the subscript, σ the spread along an axis indicated by the subscript, ρ a correlation between two variables indicated by the subscripts, a subscript up indicates updrafts, a subscript dn indicates downdrafts, a subscript env indicates environment, a subscript sfc indicates surface axis, a subscript ez indicates entrainment-zone axis, a subscript B indicates Bowen-ratio axis, and a subscript θ_F indicates solar-forcing axis.

Method	Variables Needed	Physically Based	Similarity Based
Statistical	$\bar{\theta}$, \bar{r} , σ_θ , σ_r and $\rho_{\theta,r}$		σ_θ , σ_r and $\rho_{\theta,r}$
$B-\theta_F$	$\bar{\theta}$, \bar{r} , γ_B , γ_{θ_F} , σ_B and σ_{θ_F}	γ_B and γ_{θ_F}	σ_B and σ_{θ_F}
Sub-JFD	$\bar{\theta}$, \bar{r} , $\overline{\theta_{up}}$, $\overline{\theta_{dn}}$, $\overline{r_{up}}$, $\overline{r_{dn}}$, $\sigma_{\theta,up}$, $\sigma_{\theta,dn}$, $\sigma_{\theta,env}$, $\sigma_{r,up}$, $\sigma_{r,dn}$, $\sigma_{r,env}$, α_{up} , α_{dn} , & α_{env}	$\overline{\theta_{up}}$, $\overline{\theta_{dn}}$, $\overline{r_{up}}$ & $\overline{r_{dn}}$	$\sigma_{\theta,up}$, $\sigma_{\theta,dn}$, $\sigma_{\theta,env}$, $\sigma_{r,up}$, $\sigma_{r,dn}$, $\sigma_{r,env}$, α_{up} , α_{dn} , & α_{env}
Mixing Diagram	$\bar{\theta}$, \bar{r} , γ_{sfc} , γ_{ez} , σ_{sfc} , and σ_{ez}	γ_{sfc} and γ_{ez}	σ_{sfc} , and σ_{ez}

6.2 Parameterization of JFD tilt

6.2.1 Sub-JFD method

A substantial shortcoming of the sub-JFD method described in Chapter 5 is the number of variables required to describe the JFDs (Table 6.1). The statistical method needed only five variables: the mean θ and mean r , the standard deviation of θ (σ_θ), the standard deviation of r (σ_r), and the correlation ($\rho_{\theta,r}$) between θ and r . The $B-\theta_F$ method is only slightly more complicated needing six parameters: the mean θ and mean r , the slope of the B axis (γ_B), the slope of the θ_F axis (γ_{θ_F}), the standard deviation along the B axis (σ_B), and the standard deviation along the θ_F axis (σ_{θ_F}). The new sub-JFD method requires 16 parameters: the mean θ and mean r of updrafts, downdrafts, and environment; the standard deviation of θ and the standard deviation of r for updrafts, downdrafts, and environment; the updraft, downdraft, and environmental fraction; and optionally the correlation between θ and r of each category of draft.

While these extra parameters provide a more realistic description of the convective boundary layer, they make the parameterization of this method unwieldy. While a simple expression will be derived for the tilt of the means of the updrafts and downdrafts, no simple, physically based, expression was found for the other parameters. Therefore, this method will not be used to parameterize the JFDs at this time. The excessive number of variables required by this method motivated the development of the mixing-diagram method.

6.2.2 Mixing-diagram method

The mixing-diagram method requires the same number of variables as the $B-\theta_F$ method: the mean θ and mean r , the slope of the surface axis (γ_{sfc}), the slope of the entrainment-zone axis (γ_{ez}), the standard deviation along the surface axis (σ_{sfc}), and the standard deviation along the entrainment-zone axis (σ_{θ_F}). Only σ_{sfc} and σ_{θ_F} need to be parameterized using similarity methods because γ_{sfc} and γ_{ez} are either known from observations or model output (or for γ_{sfc} can

be related to B). In Chapter 5, the theoretical basis of γ_{sfc} was introduced and will be investigated more carefully next.

As suggested by Schrieber et al. (1996), the slope of the line through the means of the updrafts, downdrafts and environment should be related to B . When B is large: the sensible heat flux is large and the moisture flux is small; variations of θ tend to be large relative to variations of r ; and the slope of the line through updraft and environment means is small. When B is small: the heat flux is small relative to the latent heat flux; the variations of θ tend to be smaller than the variations of r ; and the slope of the line through updraft and environment means is large.

We can define B , using the eddy correlation method to compute the fluxes, as,

$$B_z = \frac{C_p \overline{w\theta}}{L_v \overline{w r}}, \quad (6.1)$$

where the subscript z indicates B is a function of height, C_p is the specific heat of air and L_v is the latent heat of vaporization. Using the mass-flux approximation introduced in Chapter 4 (4.2) and ignoring the environmental flux, (6.1) can be written as

$$B_z \approx \frac{C_p (\overline{\delta w_u \delta \theta_u} \alpha_u + \overline{\delta w_d \delta \theta_d} \alpha_d)}{L_v (\overline{\delta w_u \delta r_u} \alpha_u + \overline{\delta w_d \delta r_d} \alpha_d)} \quad (6.2)$$

where $\overline{\delta w}$ is the average draft velocity, $\overline{\delta \theta}$ is the average draft perturbation value of θ , $\overline{\delta r}$ is the average draft perturbation value of r , α is the fraction of legs covered by drafts, the subscript u indicates updrafts, and the subscript d indicates downdrafts. Equation (6.2) can be simplified because of mass continuity in the boundary layer, $\overline{\delta w_u} \alpha_u = \overline{\delta w_d} \alpha_d$, to be

$$B_z \approx \frac{C_p (\overline{\delta w_u \delta \theta_u} \alpha_u - \overline{\delta w_u \delta \theta_d} \alpha_u)}{L_v (\overline{\delta w_u \delta r_u} \alpha_u - \overline{\delta w_u \delta r_d} \alpha_u)} = \frac{C_p \overline{\delta w_u} \alpha_u (\overline{\delta \theta_u} - \overline{\delta \theta_d})}{L_v \overline{\delta w_u} \alpha_u (\overline{\delta r_u} - \overline{\delta r_d})}. \quad (6.3)$$

After some algebraic manipulations (6.3) can be solved for the slope of the line through the updraft and downdraft means,

$$\frac{C_p}{L_v B_z} = \frac{\overline{\delta r_u} - \overline{\delta r_d}}{\overline{\delta \theta_u} - \overline{\delta \theta_d}}. \quad (6.4)$$

Figure 6.1 shows the observed slopes measured during BLX96 and the slopes predicted by

(6.4) using the value of B_z calculated from the horizontal flight legs. Overall equation (6.4) seems to do a good job predicting the slope of the line through the means. A further simplification can be made to (6.4). In Chapter 5 (Figure 5.11), it was shown that

$$\frac{\overline{\delta r_u} - \overline{\delta r_d}}{\overline{\delta \theta_u} - \overline{\delta \theta_d}} = \frac{\overline{\delta r_u} - \bar{r}}{\overline{\delta \theta_u} - \bar{\theta}}, \quad (6.5)$$

where \bar{r} is the mean value of r calculated for the entire leg and $\bar{\theta}$ is the mean value of θ calculated for the entire leg. Equations (6.4) and (6.5) can be combined so that the downdraft properties in (6.4) are replaced with the leg mean properties. There were some legs for which (6.4) or (6.5) do not do a good job. These cases were near the mixed layer top and (4.2) did not do a good job representing the flux.

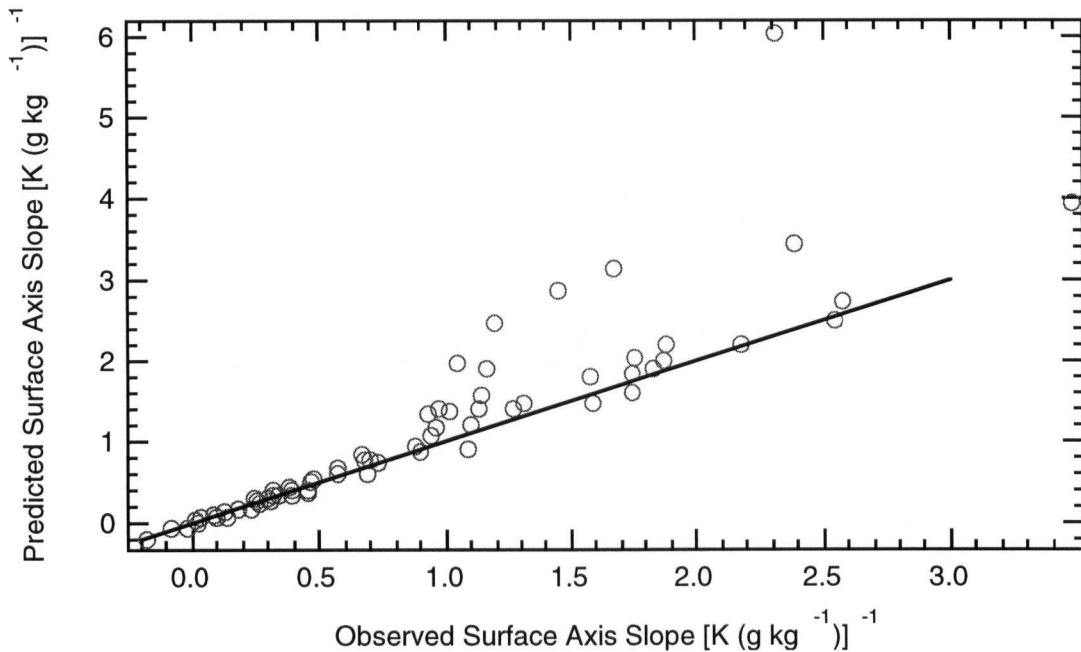


Figure 6.1. Predicted surface axis inverse slope using the left-hand side of (6.4) vs. observed surface axis inverse slope, the right-hand side of (6.4) (circles) for BLX96 case study days. The solid line is the 1:1 line.

Similar results can be found taking a different approach based on the surface energy budget. Borrowing Schrieber et al.'s (1996) methods, expressions for the surface layer perturbation values can be found (their equations 4 and 5). This can be combined to yield an equation for the slope of the line connecting the mixed-layer mean and the surface-layer

thermodynamic properties:

$$\frac{r'}{\theta'} = \frac{C_p}{L_v B_{sfc}} \quad (6.6)$$

where r' and θ' are the differences between the mixed layer mean and the surface layer value, and B_{sfc} is the surface value of B . For legs near the surface (6.6) is identical to the equation derived using the mass-flux approximation (6.5). For legs higher above the surface the (6.4) and (6.6) are not the same because of variations of the fluxes and B with height. Betts (1984) obtained results similar to (6.4) and (6.6) using a mixing diagram technique.

6.3 Parameterization of JFD spread

Expressions are needed for σ_θ , σ_r and $\rho_{\theta,r}$ used by the statistical method, σ_B and σ_{θ_F} used by the $B-\theta_F$ method, and σ_{sfc} and σ_{ez} used by the mixing-diagram method. The expressions listed in this section were found for a subset of BLX96 case-study days chosen at random (table 6.2). These “calibration subset” days happened to include legs from each location, although three of the five were the Winfield leg. Only one of the chosen days was clear. The reason for using the random subset is that the remaining case-study days will be used for verification of the results.

Table 6.2. “Calibration subset” of BLX96 case-study days used to perform the statistical fits, and the associated location and cloud-cover amount.

Date	Location	Cu Coverage
15 July	Winfield	Scattered Cu
22 July	Winfield	None
25 July	Winfield	Scattered Cu
27 July	Lamont	Scattered Cu
28 July	Meeker	Scattered Cu

6.3.1 Parameters for statistical method

Three different variables are needed to parameterize the JFDs using the statistical method: σ_θ , σ_r and $\rho_{\theta,r}$. Sorbjan (1991) suggested an expression for σ_θ/θ_* , where θ_* is the convective velocity scale (his equation 6)

$$\frac{\sigma_\theta}{\theta_*} = \left[c_{2b} \frac{(1 - z/z_i)^{4/3}}{(z/z_i)^{2/3}} + c_{2t} R^{4/3} \frac{(z/z_i)^{4/3}}{(1 - z/z_i + D)^{2/3}} \right]^{-1/2}, \quad (6.7)$$

where R is the Ball ratio (Ball 1960) of entrainment-zone heat flux to surface heat flux, D is the ratio of the entrainment zone depth to z_i , and c_{2b} and c_{2t} are empirical constants. Sorbjan suggests that $c_{2b} = 2.2$ and $c_{2t} = 6$. For the calibration subset of BLX96 days, the average value of R was 0.46 and the value of D was 0.4. Figure 6.2 shows the results from (6.7) and the BLX96 data using these average values. Sorbjan's expression does a good job representing BLX96 data, although it may underestimate σ_θ/θ_* higher in the mixed layer.

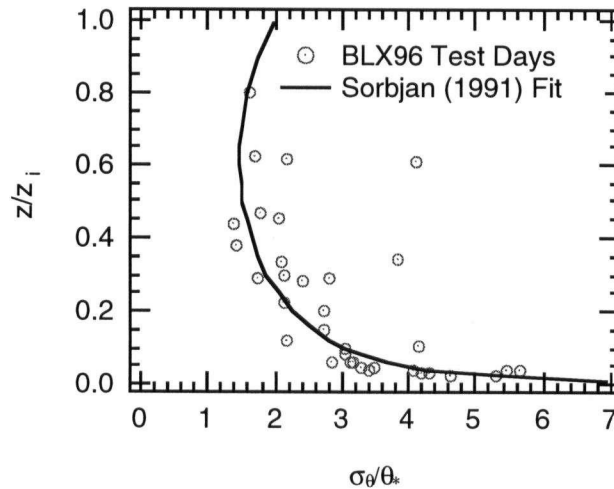


Figure 6.2. Sorbjan's expression for σ_θ/θ_* (line) and observed values of σ_θ/θ_* (symbols) vs. z/z_i for the calibration subset of BLX96 case study days.

Sorbjan (1991) also derived an expression for σ_r/r_* . However, as was shown in Chapter 3, the traditional value of r_* is not the best choice, so a new expression is derived. For convenience (3.5) is rewritten here

$$r_{*,new} = \left[\frac{\overline{w r_s} (1 - z/z_i)}{w_*} + \frac{\overline{w r_{z_i}} (z/z_i)}{w_*} \right] f(z/z_i). \quad (3.5)$$

In chapter 3, it was shown that, given $f(z/z_i) = 1$, the new scaling does a good job collapsing the BLX96 moisture data to a universal curve. For the calibration subset of BLX96 data, the least-squares best-fit expression for the curve $\sigma_r/r_{*,new}$ (Figure 6.3) is

$$\sigma_r/r_{*,new} = 2.8 + 0.25(z/z_i)^{-0.81}. \quad (6.8)$$

The universality of (6.8) needs to be tested with data from more diverse locations to verify this result.

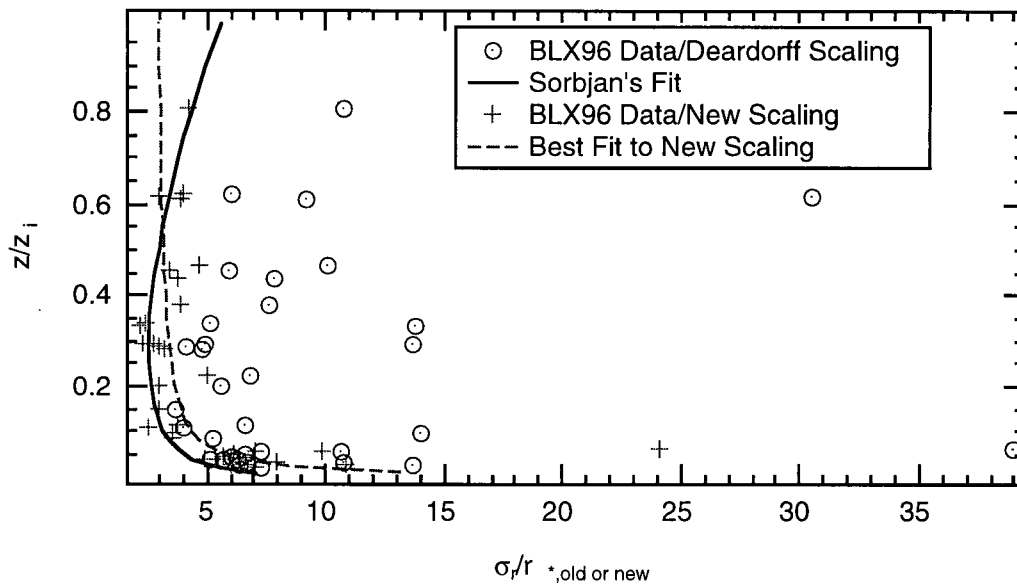


Figure 6.3. Sorbjan's expression for σ_r/r_* (solid line), BLX96 data scaled with standard Deardorff scaling, (circles), BLX96 data scaled with $r_{*,new}$ (crosses), and BLX96 best fit (6.8) (broken line), vs. z/z_i .

Expressions are also needed for $\rho_{\theta,r}$. The data from BLX96 appear linear, so a straight line was fit to the observations (Figure 6.4). The best-fit curve for the BLX96 data was found to be

$$\rho_{\theta,r} = 0.39 - 1.4(z/z_i). \quad (6.9)$$

As pointed out in Chapter 5 and shown in Figure 6.3, it appears that this curve is not universal.

Wyngaard et al. (1978) reported values of $\rho_{\theta,r}$ measured in the maritime boundary layer that were larger than those found during BLX96. Some implications of the variation of $\rho_{\theta,r}$ for different sites will be discussed in section 6.4.

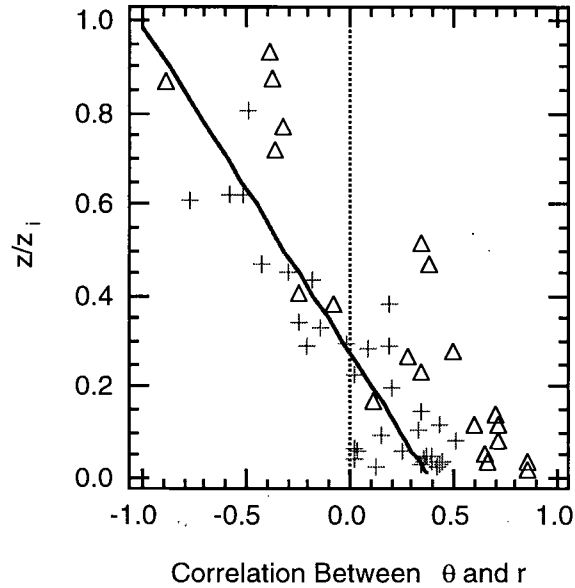


Figure 6.4. The value of $\rho_{\theta,r}$ measured by Wyngaard et al. (1978) over the ocean (triangles) and $\rho_{\theta,r}$ measured during BLX96 (crosses) vs. z/z_i . The solid line is the best-fit line to the BLX96 data.

6.3.2 Parameters for the $B-\theta_F$ method

The $B-\theta_F$ requires two different parameters: σ_B and σ_{θ_F} . Figure 6.5 shows that, when normalized by θ_* or $r_{*,new}$ the observed values of σ_B and σ_{θ_F} each collapse onto a single curve.

Using a least-squares technique, the best-fit power law was found to be

$$\sigma_B/r_{*,new} = 2.53 + 0.57(z/z_i)^{-0.65}, \text{ and} \quad (6.10a)$$

$$\sigma_{\theta_F}/\theta_* = 1.56 + 0.47(z/z_i)^{-0.56}. \quad (6.10b)$$

Alternatively, equations for σ_B and σ_{θ_F} were derived by Schrieber et al. (1996) that were based on σ_θ , σ_r and $\rho_{\theta,r}$ yielding

$$\sigma_B^2 = \left(\frac{1}{\gamma_B - \gamma_{\theta_F}} \right)^2 \left[\sigma_\theta^2 - 2\gamma_{\theta_F}\rho_{\theta,r}\sigma_\theta\sigma_r + \gamma_{\theta_F}^2\sigma_r^2 \right], \text{ and} \quad (6.11a)$$

$$\sigma_{\theta_F}^2 = \left(\frac{\gamma_{\theta_F}}{\gamma_B - \gamma_{\theta_F}} \right)^2 \left[\sigma_{\theta}^2 - 2\gamma_B \rho_{\theta,r} \sigma_{\theta} \sigma_r + \gamma_B^2 \sigma_r^2 \right], \quad (6.11b)$$

where γ_B is the slope of the B axis and γ_{θ_F} is the slope of the θ_F axis. Values of σ_{θ} , σ_r and $\rho_{\theta,r}$ needed by (6.11a) and (6.11b) were calculated from (6.7), (6.8) and (6.9).

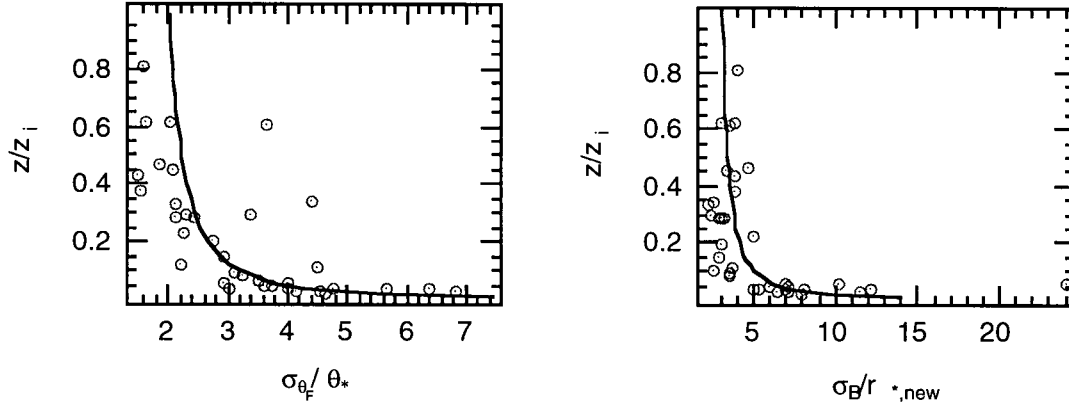


Figure 6.5. Observed values of $\sigma_{\theta_F}/\theta_*$ (left, circles), $\sigma_B/r_{*,new}$ (right, circles), and best-fit curves, (6.10a and b) (lines) for the BLX96 control days vs. z/z_i .

6.3.3 Parameters for mixing-diagram method

The values of σ_{ez} and σ_{sfc} must be parameterized for the mixing-diagram method. The tilt of the two axes are defined by conditions at the top and the bottom of the boundary layer, so that the slopes do not need to be parameterized. Using data from the BLX96 calibration subset days, least-square best-fit power-law functions can be fit to the curves of σ_{ez}/θ_* and $\sigma_{sfc}/r_{*,new}$

$$\sigma_{ez}/\theta_* = 2.0 + 8.2 \times 10^{-4} (z/z_i)^{-1.8} \quad \text{and} \quad (6.12a)$$

$$\sigma_{sfc}/r_{*,new} = 2.3 + 1.1 \times 10^{-2} (z/z_i)^{-1.6} \quad (6.12b)$$

Figure (6.6) shows (6.12a) and (6.12b) plotted as a function of z/z_i . The agreement seems to be good for the range of z/z_i observed during BLX96. However, it is not clear that θ_* and $r_{*,new}$ are the relevant scales. While the value of σ_{ez} does have units of temperature, it represents a relationship that is dependant on both θ and r (5.10). Likewise, σ_{sfc} is also a function of both θ and r . Efforts were made to define two new scaling variables using the projected variables c and

m , which were defined in Chapter 5 (5.10), c_* and m_* . First, the observed heat and moisture fluxes were converted to fluxes of c and m using Schrieber et al.'s (1996) (14a) and (14b). The fluxes of c and m , along with w_* were used to define c_* and m_* using definitions analogous to those used by standard Deardorff scaling. Unfortunately, this scaling did not improve the results.

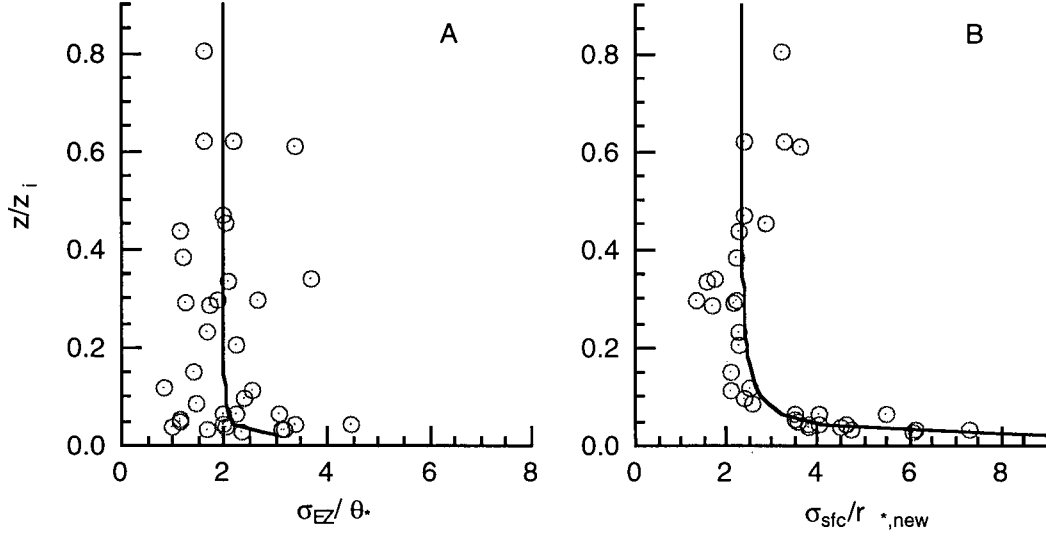


Figure 6.6. Observed (A) σ_{ez}/θ_* and (6.12a) and (B) $\sigma_{sfc}/r_{*,new}$ and (6.12b) observed on the BLX96 case study days vs. z/z_i .

As an alternative to (6.12a) and (6.12b) σ_{ez} and σ_{sfc} can be defined in terms of σ_θ , σ_r and $\rho_{\theta,r}$ using definitions derived by Schrieber et al. (1996) as

$$\sigma_{ez}^2 = \left(\frac{\gamma_{ez}}{\gamma_{ez} - \gamma_{sfc}} \right)^2 \left[\sigma_\theta^2 - 2\gamma_{sfc}\rho_{\theta,r}\sigma_\theta\sigma_r + \gamma_{sfc}^2\sigma_r^2 \right], \text{ and} \quad (6.13a)$$

$$\sigma_{sfc}^2 = \left(\frac{1}{\gamma_{sfc} - \gamma_{ez}} \right)^2 \left[\sigma_\theta^2 - 2\gamma_{ez}\rho_{\theta,r}\sigma_\theta\sigma_r + \gamma_{ez}^2\sigma_r^2 \right]. \quad (6.13b)$$

Thus, the value of σ_{ez} , σ_{sfc} and $\rho_{\theta,r}$ can be found from a combination of (6.7), (6.8) and (6.9) that accounts for the influences of both θ and r in each standard deviation. The next subsection tests the capability of (6.13) and the other parameterizations.

6.4 Verification against independent data

A “verification subset” was created from all the remaining BLX96 cases that were not randomly chosen to help with calibration. The verification subset is listed in Table 6.3.

Table 6.3. “Verification subset” of BLX96 case-study days used to perform the statistical fits, and the associated location and cloud-cover amount.

Date	Location	Cu Coverage
16 July	Meeker	Scattered Cu
23 July	Winfield	Scattered Cu
31 July	Winfield	Scattered Cu
2 August	Meeker	None
13 August	Lamont	None

JFDs were created for the verification subset of BLX96 cases using theories presented in Chapter 5 and the equations presented in section 6.3. Namely, values of σ_{θ} , σ_r , and $\rho_{\theta,r}$ needed by the statistical method were determined from (6.7), (6.8), and (6.9), respectively. Schrieber et al.’s (1996) theories were used to predict γ_B and γ_{θ_F} for the $B-\theta_F$ method. Equations (6.11a) and (6.11b) were used to predict σ_B and σ_{θ_F} , respectively. To parameterize the mixing-diagram method the value of γ_{sfc} was predicted from (6.4), while σ_{ez} and σ_{sfc} were predicted from equations (6.13a) and (6.13b). Relevant soundings were used to calculate γ_{ez} .

The similarity relationships derived in section 6.3 [(6.10a), (6.10b), (6.12a) and (6.12b)] could have been used to find σ_B , σ_{θ_F} , σ_{ez} and σ_{sfc} based on observations from BLX96. However, using (6.11a), (6.11b), (6.13a) and (6.13b), which are formulated in terms of σ_{θ} , σ_r and $\rho_{\theta,r}$, to predict the values of σ_B , σ_{θ_F} , σ_{ez} and σ_{sfc} has an advantage: results from each method are more consistent with each other. In other words, differences in the fits are due to differences in the theories, rather than differences in the predicted value of the standard deviations.

Figure 6.7 shows sample fits for 27 July 1996. This leg was flown at a height of $0.62 z_i$. In this case, the tilt of the JFD is negative. The $B-\theta_F$ method is unable to capture this behavior, while both the statistical and mixing-diagram methods can. For this case the difference between the statistical method and the mixing-diagram method is very small. As discussed in Chapter 5, the peak frequency of all methods is less than the observed JFD, although in this example the differences are small. The observed peak frequency was 0.083, while the predicted frequencies for the statistical, $B-\theta_F$, and mixing-diagram method were: 0.079, 0.060, and 0.079, respectively.

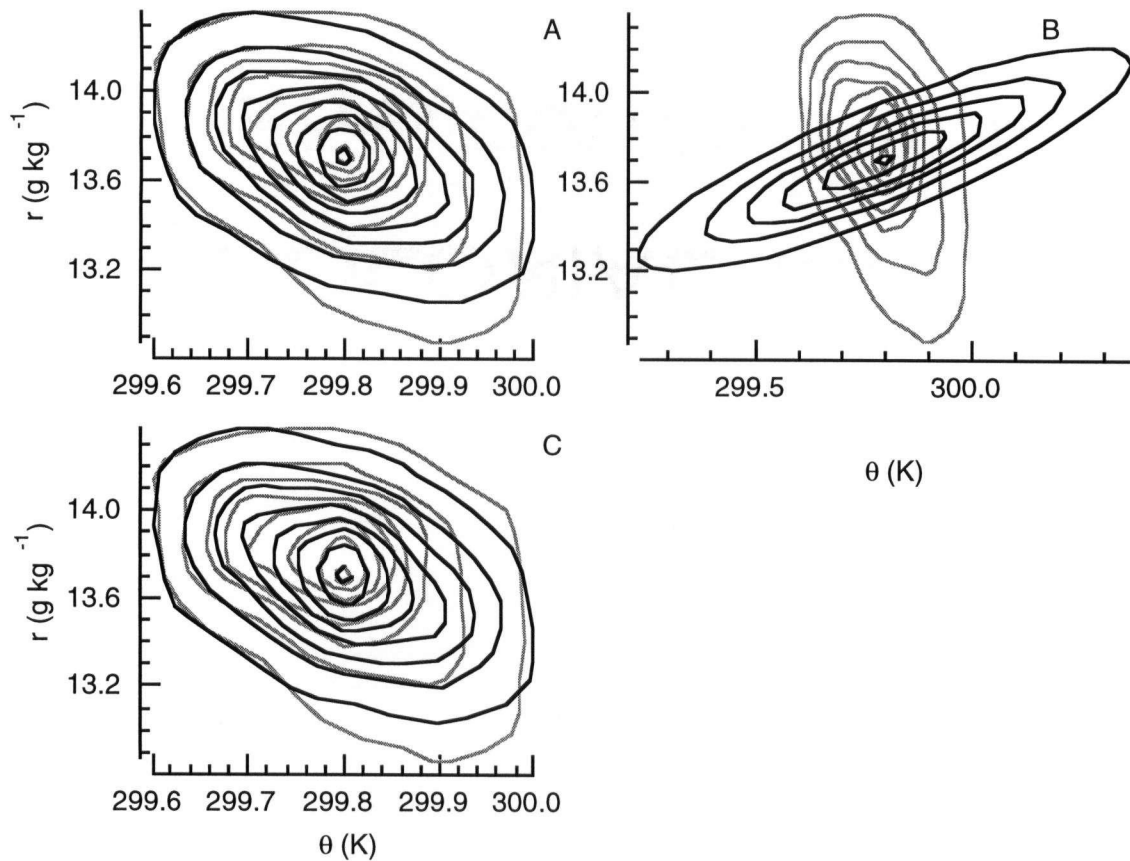


Figure 6.7 Observed (gray) and parameterized (black) JFDs using (A) Gaussian, (B) $B-\theta_F$ and (C) mixing diagram for 27 July 1996 for leg at $0.62 z_i$ at 12:11 LST. The first contour indicates a normalized frequency of 0.005 and the contour interval is 0.01 for both the observed and parameterized JFDs.

JFDs were computed for all the BLX96 “verification subset” cases, the results from which were compiled and are shown in Figure 6.8. Like Chapter 5, the $B-\theta_F$ and mixing-diagram methods will be compared to the statistical method. It appears that both the statistical method and the mixing-diagram method work better than the $B-\theta_F$ method. There is only one case where the error from the $B-\theta_F$ method is close to the one-to-one line. There is little difference in the error predicted by the statistical method and the mixing-diagram method; most of the points are very close to the 1:1 line. As pointed out by Schrieber et al. (1996), an error of 1.0 shows no skill. Both methods are better than no fit for most of the flight legs; only one flight leg had an error in the statistical or mixing-diagram method that was greater than 1.0. Many of the $B-\theta_F$ JFDs had errors larger than 1.0.

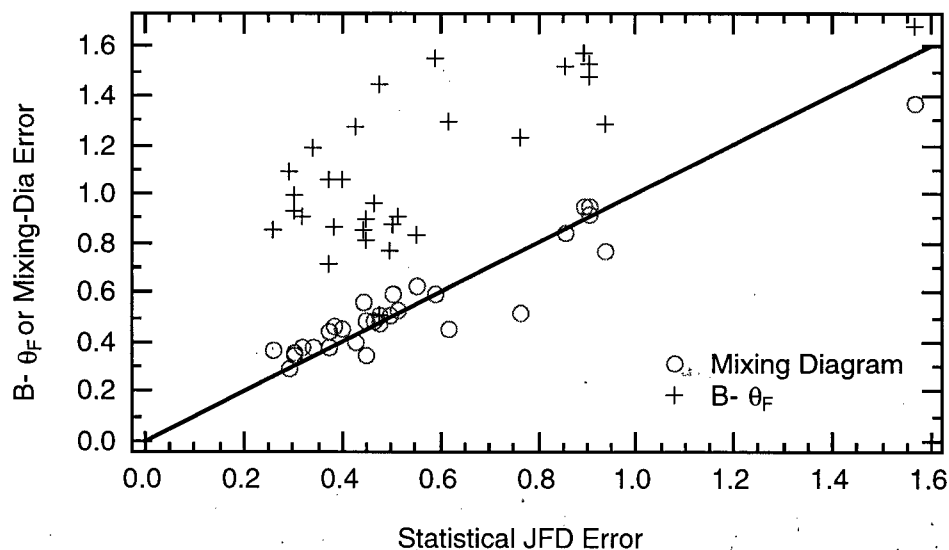


Figure 6.8. Errors associated with either the mixing-diagram method (circles) or $B-\theta_F$ (crosses) vs. errors associated with the parameterized statistical JFD. Points to the right of the one-to-one line have a smaller error than the statistical method.

The good agreement between the statistical method and the mixing-diagram method is encouraging. For the BLX96 case-study days the statistical method should do a good job because

each of the parameters, σ_θ , σ_r and $\rho_{\theta,r}$, are well behaved. However, the mixing-diagram method has several advantages over the statistical method. First, the mixing-diagram method is more robust than the statistical method because the tilt of the JFD is a function slopes of the surface and entrainment zone axes. Second, only σ_{ez} and σ_{sfc} , which could be described by (6.12a) and (6.12b) must be parameterized in the mixing-diagram method, compared to σ_θ , σ_r , and $\rho_{\theta,r}$ that must be parameterized in the statistical method. But, if (6.13a) and (6.13b) are used to estimate σ_{ez} and σ_{sfc} then, a third variable ($\rho_{\theta,r}$) is needed and both the statistical method and the mixing-diagram method depend on σ_θ , σ_r , and $\rho_{\theta,r}$. At first glance, this would seem to reduce the advantage of the mixing-diagram method over the statistical method. However, the mixing-diagram method is less dependant on the value of $\rho_{\theta,r}$ than the statistical method.

A simple test comparing the dependance of the statistical method and the mixing-diagram method on $\rho_{\theta,r}$ can be conducted by setting $\rho_{\theta,r} = 0.99$ or 0 . An absolute error range (ER) can be defined as the larger of either the difference between the error with $\rho_{\theta,r} = 0$ and the error with the observed $\rho_{\theta,r}$, or the difference between the error with $\rho_{\theta,r} = 0.99$ and the error with the observed $\rho_{\theta,r}$. This can be formalized as

$$ER = \max \left(\left\| \sum_i |\hat{f}_{\rho_{\theta,r},i} - \hat{f}_{obs,i}| - \sum_i |\hat{f}_{0.99,i} - \hat{f}_{obs,i}| \right\|, \left\| \sum_i |\hat{f}_{\rho_{\theta,r},i} - \hat{f}_{obs,i}| - \sum_i |\hat{f}_{0,i} - \hat{f}_{obs,i}| \right\| \right) \quad (6.14)$$

where $\hat{f}_{obs,i}$ is the observed frequency, $\hat{f}_{\rho_{\theta,r},i}$ is the parameterized frequency using $\rho_{\theta,r}$ predicted by (6.9), $\hat{f}_{0.99,i}$ is the parameterized frequency with $\rho_{\theta,r} = 0.99$, and $\hat{f}_{0,i}$ is the parameterized frequency with $\rho_{\theta,r} = 0$. In this test the mixing-diagram method still predicts the correct tilt to the JFD, only the estimates of the spread are effected. Figure (6.9) shows these calculations for all BLX96 case study days. In most of the cases the error range is much smaller for the mixing-diagram method than for the statistical method. The average error range calculated for the mixing-diagram method was found to be 0.5 compared to a an average error range of 1.2 for the statistical method.

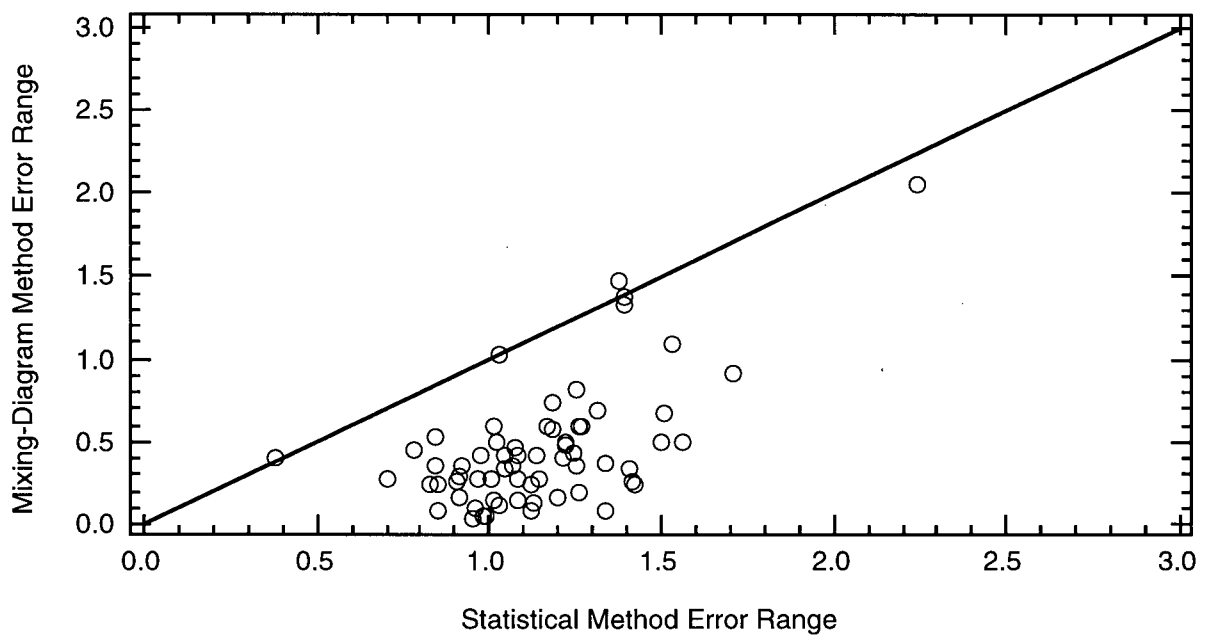


Figure 6.9. Mixing-diagram error range vs. statistical error range for all BLX96 case study days. The solid line is the 1:1 line. Points below this line indicate that the mixing-diagram error range is smaller than statistical method error range.

6.5 Conclusions and recommendations

In this chapter equations were found that can be used to find the standard deviations and correlations used to parameterize JFDs using either the statistical, $B-\theta_F$, or mixing-diagram method as a function of height. An expression is also derived to predict γ_{sfc} for use in the mixing-diagram method. Parameterized JFDs are created and compared to the measured JFDs from BLX96. Overall, the agreement between the measured and the parameterized JFDs is good, with mixing-diagram method and the statistical method having about the same skill. The mixing-diagram method is recommended because it has two advantages over the statistical method: (1) the tilt is based on physical processes, and (2) the parameterized JFD is less sensitive to the value of $\rho_{\theta,r}$. The $B-\theta_F$ method was also used to generate JFDs, but was not as successful as the other methods, and is not recommended.

Chapter 7: Accuracy of Point and Line Measures of Boundary Layer Cloud Amount¹

7.1 Introduction and Motivation

All measurements, particularly those of cloud cover, contain some errors. Before introducing a parameterization to predict boundary-layer cloud cover in the next Chapter, these cloud-cover measurement errors should be examined.

One of the oldest, and perhaps most common, methods of observing cloud cover is a human observer stationed on the ground. In this case, the observer reports the fraction of sky dome that is covered with clouds. Alternatively, cloud cover can be reported in terms of the fraction of the Earth's surface that is covered by clouds, which is the definition of cloud cover that will be used in subsequent chapters. This value can be measured with a downward looking satellite. It can also be measured when a sensor on an aircraft is flown over or under a cloud field, or when a cloud field is blown over a vertically looking, narrow-beam sensor on the ground. These two measures of cloud amount are usually not the same because both the cloud base and cloud sides block parts of the sky dome, so that sky cover is greater than earth cover (Appleman 1962; Hoyt 1977). Both Malick et al. (1979) and Henderson-Sellers and McGuffie (1990) have developed empirical relationships coupling these two types of observations.

These different definitions of cloud cover maybe useful for different applications. The sky cover is useful for radiation budget measurements where presence of cloud sides contributes to both the short and longwave radiation received at a point on the surface. Earth cover of fair weather cumuli is a pertinent parameter for coupling boundary-layer processes to the amount of cloud cover, and for determining the transfer of pollutants out of the convective boundary layer.

Many researchers, as well as the Automated Surface Observing System (ASOS) used by the National Weather Service (NWS) and Federal Aviation Administration (FAA), use a

¹This chapter has been adapted from: Berg, L. K., and R. B. Stull, 2002: Accuracy of point and line measures of boundary layer cloud amount. *J. Appl. Meteor.*, **41**, 640-650.

ceilometer, lidar or other vertically looking active sensor to estimate earth cover [Bretherton et al. 1995; White et al. 1995; Fairall et al. 1997; National Oceanic and Atmospheric Administration (NOAA), FAA, U.S. Navy, and U.S. Air Force 1998; Grimsdell and Angevine 1998; Lazarus et al. 2000 are recent examples]. For these instruments a cloud is detected when the sensor's emitted light is scattered off of clouds and returned to a detector on the surface. Earth cover is the fraction of measurement intervals, over some arbitrary averaging time, where clouds are detected. A typical averaging time is one-half hour.

Other methods are passive, detecting a cloud when sunlight reaching a pyranometer on the ground or on an aircraft is interrupted by cloud shadow (Ek and Mahrt 1991). When the sun is not directly overhead, errors arise because the silhouette of the cloud blocking the sunlight includes the vertical depth of the cloud, not just the horizontal cross-sectional area.

While many have used vertically pointing sensors, little has been mentioned of the accuracy of these measurements. Aviolat et al. (1998) is an exception. They indicate that ceilometers are not a good tool to estimate cloud cover because they are point measurements. The sampling error associated with a point measurement can be large, particularly during periods with low wind speeds, when few clouds move over the sensor. In order to improve the accuracy of these measurements a longer averaging time can be used, however nonstationarity of the cloud field could become an important factor. Feijt and van Lammern (1996) improved their cloud-cover measurements by combining ceilometer measurements with satellite observations.

The purpose of this chapter is twofold. First, earth-cover errors associated with observations from an upward looking sensor are compared to averaging time or distance. For airborne sensors this could be the length of time it takes to fly one flight leg. For sensors on the ground this corresponds to the length of atmosphere advected over the sensor. Inspired by the work of Poellot and Cox (1977), who looked at the averaging time needed to measure accurate shortwave fluxes, and Santoso and Stull (1999), who designed optimal flight patterns to sample boundary-layer turbulence, tests are conducted where a virtual aircraft is "flown" under a simulated cloud field. An empirical set of equations are found for the virtual data that relate the measurement

errors to an arbitrary averaging length and earth cover. Second, these virtual results are used to interpret a comparison of passive pyranometer measurements with human estimates of earth cover made during BLX96 (Chapter 2).

7.2 Earth-Cover Observation Methods

7.2.1 Simulated Observations

There has been much debate in the literature about the nature of the spatial distributions of real cumuli. Some researchers have suggested that cumuli are clumped (Plank 1969; Randall and Huffman 1980; Joseph and Cahalan 1990; Sengupta et al. 1990). Other authors believed that fields of cumuli were regular (Bretherton 1987, 1988; Ramirez and Bras 1990). Some authors have assumed that cloud fields were randomly distributed (Ellingson 1982; Zuev et al. 1987). Others have found that smaller cumuli were clumped, while the larger cumuli tended to a more regular or random distribution (Weger et al. 1992; Zhu et al. 1992). Ramirez and Bras (1990), Weger et al. (1992), and Zhu et al. (1992) related observed or simulated nearest-neighbor distributions to theoretical nearest-neighbor distributions for a random process, for many different cloud fields. They found that very different looking cloud fields, including random cloud fields, could produce similar nearest-neighbor distributions. In some cases terrain elevation (Smolarkiewicz and Clark 1985) or the presence of lakes (Rabin et al. 1990) can also influence the cloud cover.

A random cloud field was used in this simulation study. Vertically thin, horizontally circular clouds were randomly placed on a regular 0.1 km grid in a 710 by 82 km domain. The clouds were not allowed to overlap, but cloud edges could touch. Using standards proposed by Joseph and Cahalan (1990), this simulated cloud field is very slightly regular. Tests showed that cloud-cover statistics generated from slightly regular or completely random cloud fields are indistinguishable from each other.

The cloud diameters were chosen to follow a log-normal distribution. The parameters for

the log-normal distribution were chosen to be consistent with the observations of Lopez (1977) and Plank (1969). For the results presented, the mean cloud radius was 0.5 km and the standard deviation was 2.0 km.

Earth-cover values were allowed to range from 5% to 40% for the tests, which corresponds to “few cumuli” to “scattered”. All of the cloud centers were located within the domain, but clouds could hang off the edge of the domain. This might lead to inaccurate earth-cover estimates near the edge because no clouds were allowed to hang onto the domain. To eliminate edge effects the simulated aircraft “flew” horizontal legs within a sub-domain of 690 by 72 km. Each parallel leg was 0.1 km apart laterally, and ranged in length from 5 to 70 km. During each virtual flight, the fraction of the flight leg that was under simulated clouds was recorded to provide a line average. These results also correspond to a cloud field advecting over a ground based sensor at a variety of wind speeds.

A second experiment using the virtual aircraft was conducted to compare earth cover estimates made along a single line through the cloud field to the earth cover estimated using a swath (area) average centered on the aircraft. This experiment corresponds more closely to the earth-cover measurements by an observer on board an aircraft who can see cloud shadows covering the ground to the left and right of the aircraft track, in addition to the shadows immediately ahead. The width of the swath (3.5 km) was chosen to be similar to the area beneath the aircraft used to estimate earth cover during BLX96.

7.2.2. Effect of solar zenith angle on cloud shadows

Using cloud shadows projected on the Earth to estimate earth cover, the method used during BLX96, is exact only for a solar zenith angle (ϕ) of zero or, alternatively, for infinitely thin clouds. As ϕ increases, part of the sunlight could be blocked by the cloud sides, causing the shadow projected onto the Earth’s surface to be larger than the true earth cover. Taller clouds enhance this effect because more sunlight is blocked. However, for shallow clouds and high sun,

the earth-cover errors are minimal. During BLX96 most flight legs were flown during fair-weather, anticyclonic conditions within a few hours of solar noon and ϕ ranged between approximately 15° and 36° and were less than 30° for 80% of the legs flown. It was observed during BLX96 that most of the cumuli were short, with an aspect ratio between one and two.

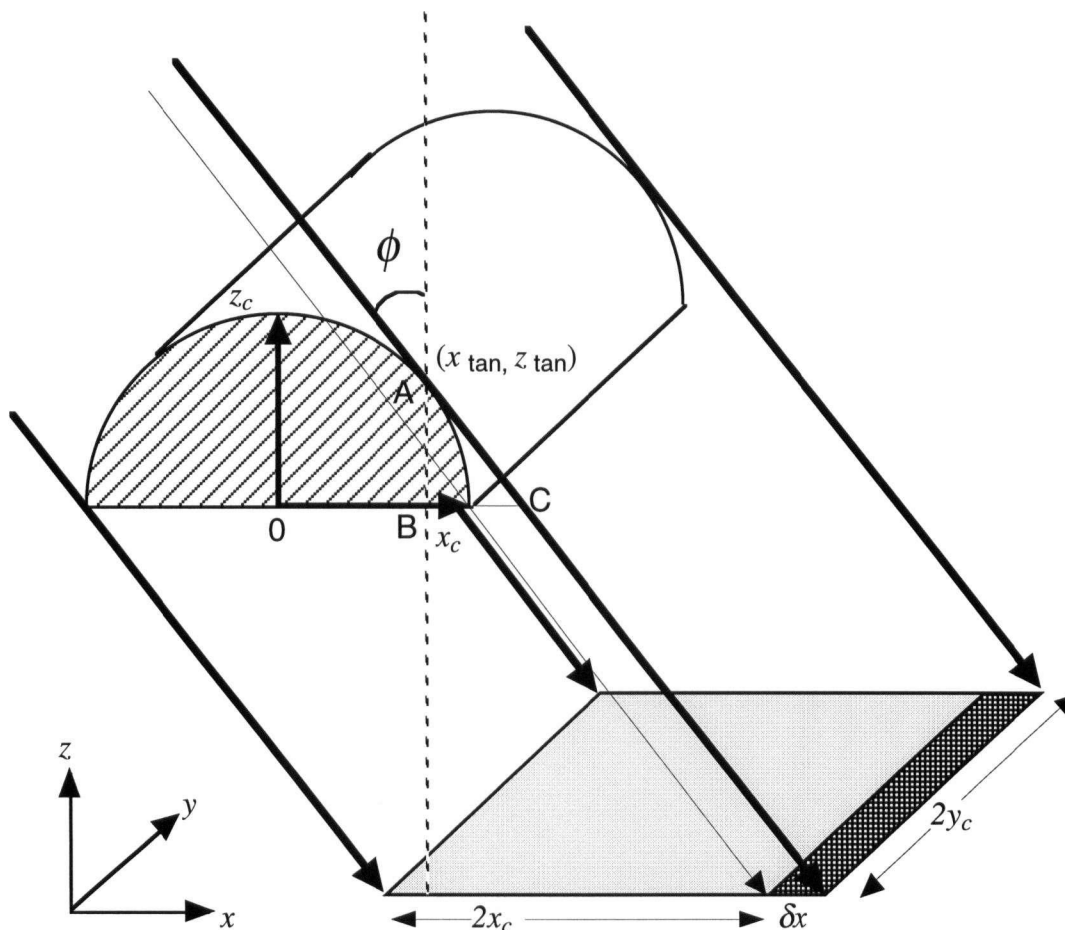


Figure 7.1. Sketch showing cloud geometry used to estimate the earth-cover error associated with cloud thickness and ϕ . Heavy descending arrows represent the actual sun's rays, the thin one represents a ray striking the edge of an infinitesimally thin cloud. The shaded semicircle aloft is a single boundary layer cumulus with height z_c . The point, x_{\tan}, y_{\tan} , marks the tangent point of the sun's ray. Shading below the cloud shows the true cloud width ($2x_c$), and the error associated with the solar zenith angle (δx).

A simple analytical experiment can be used to estimate the error in measured earth cover due to different ϕ and cloud aspect ratios. For this analysis the downwelling radiation is assumed to be plane parallel. Clouds are assumed to have flat bottoms, a square base and are semi-circular or semi-elliptical in cross section parallel to the sun's rays (Figure 7.1). Clouds are assumed to have a rectangular cross section in the dimension perpendicular to the sun's rays, in other words the clouds rotate as the sun moves across the sky. One important implication of this cloud geometry is that the cloud shadow is rectangular.

With these assumptions and a value of ϕ , the amount that cloud shadows overestimate earth cover can be calculated analytically. Figure 7.1 shows an example where the cloud shadow is some amount (δA) larger than the true earth cover (A). The geometric location of cloud top is defined using

$$\frac{x^2}{x_c^2} + \frac{z^2}{z_c^2} = 1, \quad (7.1)$$

where x_c is one-half the cloud width, and z_c is the cloud thickness. The location on the cloud where the sun's ray is tangent to the cloud determines how much radiation the cloud blocks and the size of the cloud shadow ($A + \delta A$). This point is found by taking the derivative of (7.1) with respect to x to find the slope of the tangent line at any point along the cloud's top. Combining this result with (7.1) and ϕ yields equations for the z location (z_{\tan}) and the x location (x_{\tan}) where the sun's ray is tangent to the cloud's top

$$z_{\tan} = z_c \left[\frac{x_c^2 \tan^2(\pi/2 - \phi)}{z_c^2} + 1 \right]^{-1/2}, \quad (7.2)$$

$$x_{\tan} = x_c \left[\left(1 - z_{\tan}^2 / z_c^2 \right) \right]^{1/2}. \quad (7.3)$$

As shown in Figure 7.1, the triangle (ABC) formed by a vertical line through the tangent point, the cloud base, and the line representing the sun's ray, can be used to find the length (δx) added to the cloud shadow. This equation can be written as

$$\delta x = x_{\tan} + z_{\tan} \tan(\phi) - x_c. \quad (7.4)$$

Equations (7.3) and (7.4) show that the error is a function of the cloud thickness, width, and ϕ .

As a check of the behavior of these equations we find that as ϕ approaches zero in (7.2), $\tan^2(\pi/2 - \phi)$ approaches infinity, and z_{\tan} approaches zero. Using (7.3) we find that $x_{\tan} = x_c$, and (7.4) predicts that the error approaches zero, as expected when the sun is directly overhead.

The total area of the cloud shadow can be found using (7.4) and a cloud length of $2y_c$

$$A + \delta A = 2y_c(2x_c + \delta x) = 4x_c y_c + 2y_c \delta x. \quad (7.5)$$

The total area is a function of cloud height, diameter, and ϕ . A fractional error can be defined as $[(A + \delta A)/A]$, which, using (7.5) can be rewritten as $1 + \delta x/2x_c$. Combining this form of the fractional error with equations (7.2) through (7.4) yields an equation for the fractional error that is a function of only the aspect ratio of the cloud ($R = 2x_c z_c^{-1}$) and ϕ

$$\frac{A + \delta A}{A} = \frac{1}{2} \left\langle 1 + \left[1 - [0.25R^2 \tan^2(\pi/2 - \phi) + 1]^{-1} \right]^{1/2} + 4R^{-2} [\tan^2(\pi/2 - \phi) + 4R^{-2}]^{-1/2} \tan(\phi) \right\rangle. \quad (7.6)$$

From the observations of cloud diameters and cloud heights during BLX96, as well as the solar zenith angle calculated from the time, latitude, and longitude of the flights, the error in earth cover associated with cloud shadows can be calculated. For shallow clouds with an aspect ratio of two, the fractional error is small, 1.11 for $\phi = 35^\circ$ (Figure 7.2). As the clouds grow deeper, the error increases, for clouds with aspect ratio of one, the fractional error is 1.36 for $\phi = 35^\circ$, but is much smaller for smaller ϕ . For taller clouds the error would be even more substantial. Thus, for most of the BLX96 observations the error is small, and the cloud shadow method can be used to infer earth cover (Appendix F).

7.3 Simulated Cloud Field Results and Applications

7.3.1. Results

The “observed” mean earth cover, estimated by sampling along lines with the virtual aircraft, is very close to the true simulated earth cover based on the known areal coverage of the synthetic clouds (Figure 7.3). These results are almost independent of the length of the simulated

flight leg, at least for legs as short as 5 km, or about 2 to 5 times the mean distance to the nearest neighbor, depending on the earth cover. There is a small bias, which increases as the leg length gets shorter (approximately 2% bias for the 5 km long leg).

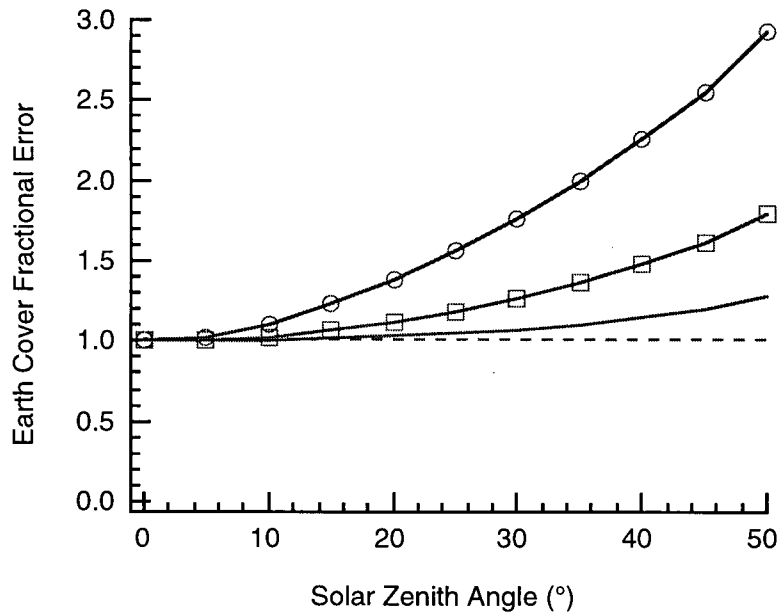


Figure 7.2. Earth cover fractional error vs. solar zenith angle for aspect ratios of two (no symbol), one, (squares) and one-half (circles). The dashed line marks a fractional error of one.

The standard deviation of the mean earth cover for all legs can be calculated to give an estimate of likely measurement errors. This leg-to-leg standard deviation decreases with increasing leg length (Figure 7.4). However, the changes are smaller for longer legs. The standard deviation is smaller for the swath than for the single line average. Figure 7.5 provides another, more explicit, look at the differences between the single line and the swath measurements. For this case of 20% true simulated earth cover, the swath estimates of earth cover range from 10% to 33% while the single-line average ranges from about 7% to 42%.

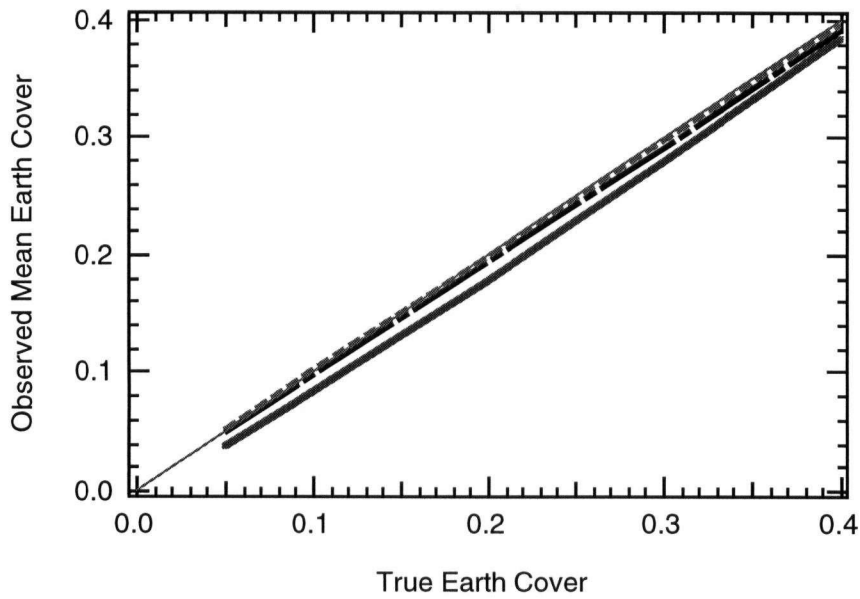


Figure 7.3. Observed virtual mean earth-cover vs. true simulated earth cover for legs of 5 (thick solid), 20 (dot dashed), and 70 km length (dashed) for all 6900 legs. The thin solid line is the 1:1 line.

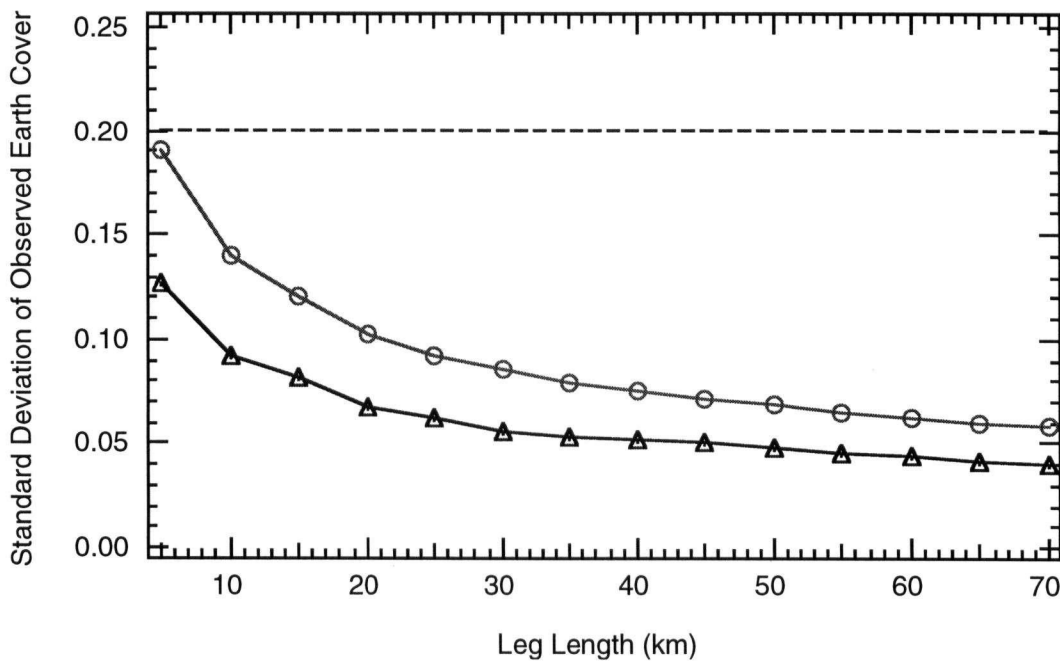


Figure 7.4. Leg-to-leg standard deviation of the observed earth cover vs. leg length for single line averages (circles) and vs. leg length for a swath average (triangles), for a case with a true simulated earth cover of 20% (dashed line). A smaller standard deviation implies that the sample is a better estimate of the true cloud population.

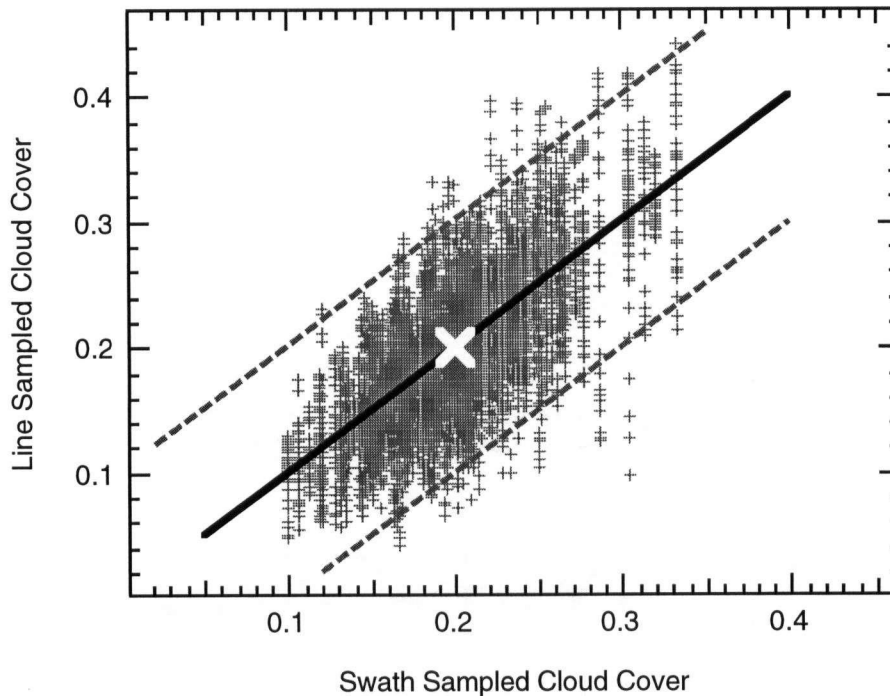


Figure 7.5. Simulated line-sampled vs. simulated swath-sampled earth cover for a case with a true earth cover of 20% (white X) and a leg length of 70 km. The solid line is the 1:1 line, the dashed lines are $\pm 10\%$ from the the 1:1 line.

The leg-to-leg standard deviation increases with earth cover for simulated true earth cover values less than about 20% (Figure 7.6). For the 5 km long leg the standard deviation is larger than the simulated true earth cover for earth covers ranging from 0 to just under 20%. For simulated earth cover greater than 20%, the standard deviation is only a weak function of earth cover. The qualitative shape of the standard-deviation curve in Figure 7.6 can be explained by the bounded nature of earth cover, which can only range between 0 and 100%. The relatively small leg-to-leg standard deviation “measured” by the virtual aircraft at smaller earth covers is affected by the number of legs with no earth cover. For example, given 5 km long legs and 5% earth cover, over 80% of the legs flown had no earth cover, leading to a smaller standard deviation (although still larger than the observed earth cover) than would be expected if a distribution with negative earth covers was used. As the true earth cover gets larger there are fewer legs with 0% earth

cover, and the standard deviation increases until the effects of the bounding are removed. Similar effects are expected at larger earth covers, because the maximum earth cover is also bounded.

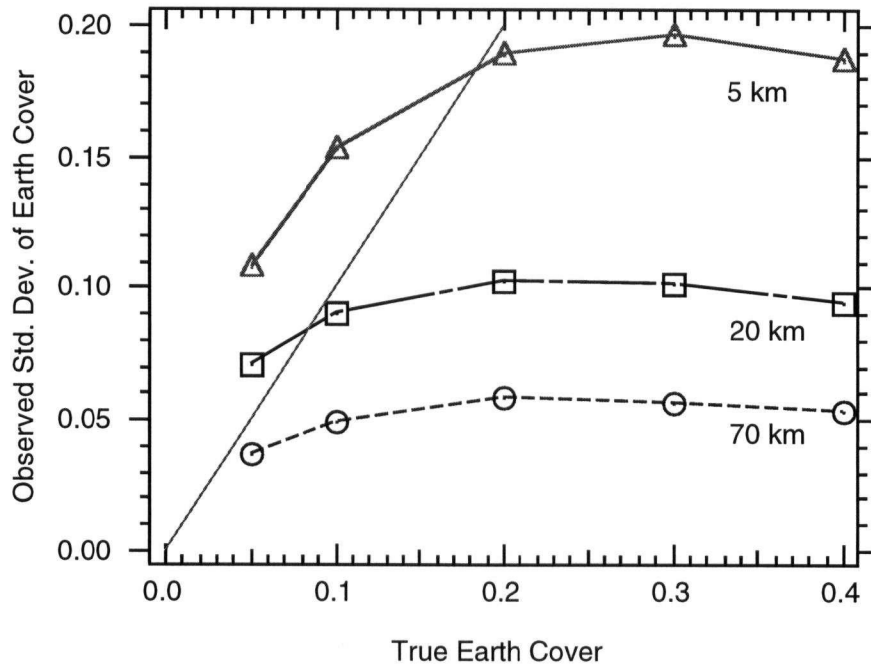


Figure 7.6. Leg-to-leg standard deviation of sample earth cover vs. true earth cover for flight legs of 5 (solid line with triangles), 20 (dot dashed line with squares), and 70 km length (dashed with circles). The thin solid diagonal line is the 1:1 line, and points above this diagonal line have errors greater than the true earth cover.

These results have important implications for ground-based instruments. Clouds are advected by the mean wind over ground-based instruments. A hypothetical wind speed of 10 m s^{-1} , and an averaging time of 30 minutes (such as that used by ASOS) corresponds to an averaging length of about 20 km. For legs of this length the maximum leg-to-leg standard deviation is about 10%, and for earth covers smaller than about 8% the standard deviation is larger than the observed earth cover (Figure 7.6). To reduce the standard deviation close to 5% an averaging time of 90 minutes is needed. This time period is rather long, the non-stationarity of the cloud field could be important.

Cases with organized cloud fields have been ignored in this study. The clouds are assumed to be randomly distributed. During periods of strong wind, roll vortices can form (Etling and Brown 1993; Weckwerth et al. 1997). In this case the clouds would be organized in rows that are nearly parallel to the mean wind. A ground-based sensor might measure earth covers that are very small or very large, depending on the location of the sensor relative to the cloud streets. Thus, the error could be much larger than the values suggested by this study. It is for just this reason that research flights in the real convective boundary layer are usually flown crosswind.

The size distributions of clouds cannot be inferred from a single leg. There were many legs, even at 40% earth cover and 70 km long legs where the virtual aircraft intercepted only a small number of clouds. However when all of the flight legs were combined, the cloud size statistics approach the true distribution (not shown).

7.3.2. Applications

An equation, or a set of equations, relating the error in the measured earth cover of fair-weather cumuli to the leg length and the earth cover can be found. Such an equation would be useful to scientists planning a field program or interpreting results from previous field work. Figure 7.4 shows an example of the leg-to-leg standard deviation measured with the virtual aircraft for a true simulated earth cover of 20%. Similar plots were made for a range of simulated earth covers; while the general shape of the curves are the same, there are large differences in the fit parameters. It may be simpler to relate the Noise to Signal Ratio (NSR) to the leg length, where NSR is defined to be

$$\text{NSR} = \sigma_x / \bar{x}, \quad (7.7)$$

where \bar{x} is the average and σ_x is the standard deviation of any variable, x . Unfortunately, the NSR curves also vary greatly with different amounts of earth cover. However, the simulated observations collapse onto one “universal” curve when the NSR is normalized by the NSR of the shortest leg flown, which is the maximum NSR (NSR_{MAX}) observed at a given true simulated earth cover. A power-law relationship was fit to the $\text{NSR}/\text{NSR}_{\text{MAX}}$ points, yielding an expression

of the form

$$\frac{\text{NSR}}{\text{NSR}_{\text{MAX}}} = -(0.0832 \pm 0.006) + (2.22 \pm 0.01)l^{-(0.445 \pm 0.005)}, \quad (7.8)$$

where l is the averaging length in kilometers. The NSR_{MAX} is a function of earth cover (not shown). Again, a power-law relationship was fit to the NSR_{MAX} data, yielding

$$\text{NSR}_{\text{MAX}} = -(1.03 \pm 0.07) + (0.994 \pm 0.06)\alpha_{\text{cloud}}^{-(0.462 \pm 0.01)}, \quad (7.9)$$

where α_{cloud} is the earth cover fraction. Equations (7.7), (7.8), and (7.9) can be combined to give an expression for the leg-to-leg standard deviation given some arbitrary leg length and earth cover

$$\sigma_{\text{cloud}} = \alpha_{\text{cloud}} \left(0.0856 - 0.0827\alpha_{\text{cloud}}^{-0.462} - 2.29l^{-0.445} + 2.21\alpha_{\text{cloud}}^{-0.462}l^{-0.445} \right). \quad (7.10)$$

For leg lengths greater than 15 km, (7.10) is accurate to within 8% of the standard deviation observed by the virtual aircraft flying under the simulated cloud field. For shorter flight legs (7.10) is not as accurate. For example, given 5 km long legs and 5% earth cover, (7.10) overestimates the standard deviation observed by the virtual aircraft by about 35% [i.e. 15% predicted by (7.10) compared to 11% measured with the virtual aircraft].

Alternatively, when planning a field program, one might be interested in the leg length (in km) required to estimate the earth cover to some desired accuracy. Equations (7.8) and (7.9) can be manipulated to give

$$l = \left[\frac{\text{NSR}}{-2.28 + 2.21\alpha_{\text{cloud}}^{-0.462}} + 0.0374 \right]^{-2.25}. \quad (7.11)$$

The average error in leg length predicted by (7.11) for all simulated earth covers, compared

to the simulated flight legs, is about 3%. The maximum error in leg length estimated using (7.11) compared to observations using the virtual aircraft is 14%, which occurs for a simulated earth cover of 20% [i.e. 60.5 km predicted by (7.11) compared to 70 km measured with the virtual aircraft]. In a strict sense (7.11) is circular, one must know the earth cover to determine the leg length that is needed to measure the earth cover. However, in practice a range of applicable earth cover or some approximate value of the earth cover is often known from the climatology of the field site, so that (7.11) can be used to estimate the leg lengths needed. For example, during BLX96 all of the flights were to take place during conditions with fair-weather cumuli cover of 0 to 30%, but not during conditions with more earth cover. So (7.11) could be used with hypothetical earth covers ranging from near zero to as large as 30%, to estimate the maximum leg length that would be required to give good earth cover estimates.

How does the leg length required for accurate estimates of earth cover compare to the leg lengths needed for accurate measurements of turbulent statistics? Lenschow et al. (1994) found that for a leg length of 20 km the random error in the scalar fluxes is about 18%. For a leg length of 70 km the errors in the scalar fluxes drops to about 12%. From the Lenschow et al. work, the requirements for the accurate measurement of turbulent quantities in the boundary layer are more strict than that required for measurements of earth cover. Thus, choosing a leg length to give accurate turbulent statistics should meet the requirements needed for accurate measurement of fair-weather boundary-layer earth cover.

7.4 Observed BLX96 Results

The agreement between the airborne observer and the aircraft mounted pyranometer during BLX96 is good, but not perfect (Figure 7.7). These observations have been corrected for the cloud shadow error using (7.6). Most of the observations (90%) are within $\pm 10\%$ of each other. There appears to be little bias between the different observers. When the earth cover is small, the airborne observer tended to estimate larger amounts of earth cover than was recorded by the pyranometer.

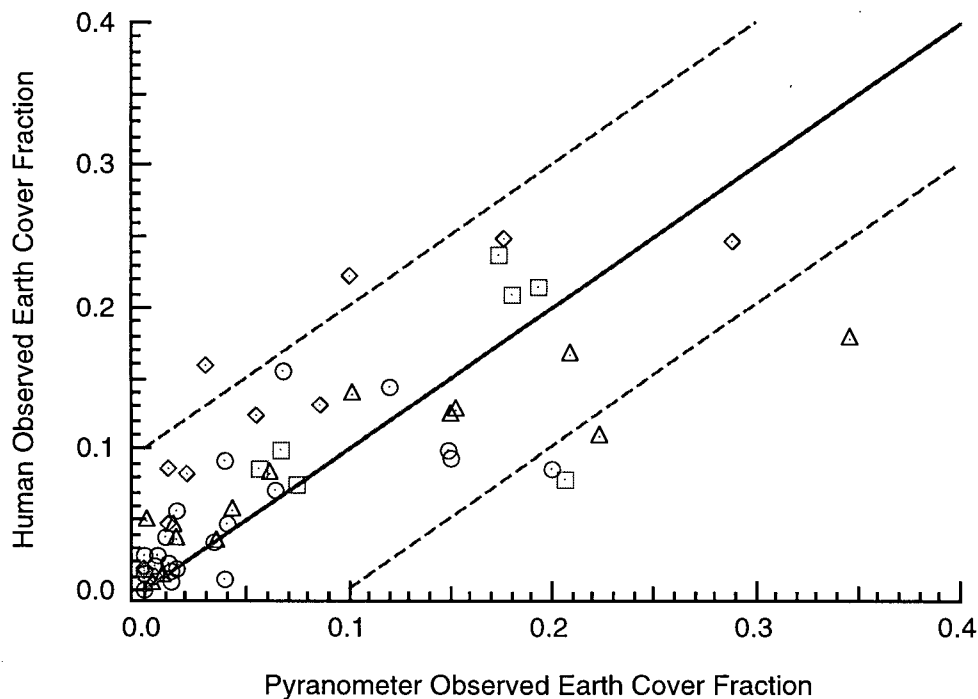


Figure 7.7. Human-observed, swath (area) average, earth-cover fraction for each of the four different scientists (different symbols) vs. pyranometer-observed, line sampled, earth-cover fraction for all BLX96 cloudy legs. The thin solid line is the 1:1 line, the thin dashed lines are ± 0.1 from the 1:1 line.

A straight line can be fit to the observations. Both the errors in the pyranometer and the errors in the human observations must be accounted for when fitting a straight line to the data (Press et al. 1992). The error in the aircraft pyranometer was assumed to follow (7.10) using a 70 km long leg. The human errors were taken to be similar to those suggested by Young (1967). Two factors should be considered when using Young's error analysis. His data were for humans analyzing satellite photos rather than a quick look at a real cloud field, so the errors in BLX96 are likely to be larger than those found by Young. The smallest earth cover he used was about three oktas. This is about the maximum earth cover observed during BLX96. Young found that the error in measured earth cover shrinks as the true earth cover increased. He argues that as the true earth cover shrinks, the error in measured earth cover shrinks as well. He suggests that for an

earth cover of zero, there would be zero error in the human observations. This precludes using some of the BLX96 data in the prescribed fitting procedure because zero error leads to a singularity in the calculations. With all human observations of zero earth cover removed, the calculated slope of the best-fit line is 0.9 ± 0.13 and the intercept is 0.0004 ± 0.0002 . These fit parameters indicate that the two observed distributions are drawn from the same parent distribution.

A second test, the Kolmogorov-Smirnov test, can be used to determine if the observed distributions came from the same parent distribution (Press et al. 1992). This test compares the cumulative distributions of two variables. The largest value of the difference between these two distributions is used as a test statistic and is compared to the Kolmogorov-Smirnov probability function to determine the confidence of the estimate. For the BLX96 data the largest difference in the cumulative distribution functions was 0.18, the p-value was 0.24, so there is insufficient evidence to indicate that the distributions are different.

While the statistical tests suggest that the parent distributions are the same, there are a number of reasons for the scatter in Figure 7.7. Sampling errors are a likely explanation. The airborne observer looked at cloud shadows projected within a swath area on the ground under the aircraft. When averaged over the entire flight leg, this corresponds to a wide swath, approximately 3.5 km wide during BLX96, through the cloud field. The pyranometer is a line estimate through the cloud field. The two methods are sampling different areas to estimate the earth cover. The experiment with the virtual aircraft can also provide insight into this question. Although constructed using only one true simulated earth cover of 20%, Figure 7.5 provides some insight into this question. Points for cases of different simulated earth cover could be added to the plot, but the qualitative results would be unchanged. Many of the differences between the swath and the line-sampled earth cover in Figure 7.5 are similar in magnitude to the differences shown in Figure 7.7. Henderson-Sellers and McGuffie's (1990) results are similar. They compared sky cover and earth cover measured from all-sky images, and had much scatter. They found many cases where there were not clouds directly above the sensor although some clouds were reported nearby,

similar to the BLX96 results at small earth cover.

Another factor that could contribute to the differences at smaller earth cover is the method used by the airborne observer to measure earth cover. During most of the flights with clouds, it was usual for earth cover to vary along any single 70 km leg, as the aircraft flew through meso- γ scale regions that were relatively clearer or cloudier than others. For these situations, the observer only reported the earth cover at the start of each leg and again when they noticed a change during the flight. Also at other times the observer was busy with other duties. So, particularly when the earth cover is small, there are portions of the leg that have no earth cover that might not be accurately reported. If some zero values were missed, then the leg average would be too large.

7.5 Conclusions

The primary goal of this work was to determine the accuracy of earth-cover measurements by both ground-based and aircraft-mounted sensors for a range of boundary-layer earth covers. Two different comparisons were made. First, sampled results for both line and swath averages were compared to the prescribed cloud cover from a simulated cloud field. These results suggested that, for short flight legs or averaging times, the observed standard deviation was often larger than the mean earth cover. When longer flight legs or averaging times were used, the earth-cover measurements were within $\pm 5\%$ of the true cover for a wide range of earth cover.

Using the virtual data, a set of empirical equations were presented so that the appropriate leg length could be found for some arbitrary NSR, and to find standard deviation of earth cover from leg length and true earth cover. The accuracy of earth cover inferred from ceilometer or other vertically pointed instruments depends on a number of factors, including wind speed. At high wind speeds these measurements might be suspect because of horizontal roll vortices, at lower wind speeds the measurements are suspect because of random sampling errors.

For shallow boundary-layer cumuli (i.e. cumulus humilis) and high sun angle it was shown that the shading of the ground by the vertical portion of the cloud silhouette caused errors of

about 5%. For true earth coverage between 5 and 30% this vertical silhouette error was small compared to typical observation and sampling errors of about 17% for 5 km long legs, and was about the same size as the observation and sampling errors for 70 km long legs.

Second, estimates of earth cover from an aircraft-mounted pyranometer were compared to estimates from an airborne observer. In general, there was good agreement between the airborne human observer and the pyranometer measured earth cover from BLX96. Tests were conducted that suggest that the two observed distributions came from the same parent distribution. However, it also seems that the human observer tends to estimate a larger earth cover at small values of earth cover. Two suggestions are made that might explain these differences: different sampling techniques between the human and pyranometer, and improper recording of zero earth cover.

Field work should include a structured methodology for the airborne observer to measure earth cover. It is recommended that human estimates should be made at regular intervals during the flight and intercomparisons between the observers should be undertaken. However, this research also shows, that given the accuracy of the pyranometer measured earth cover for long flight legs, that human estimates might not be necessary.

Chapter 8: A New Fair-Weather Cumuli Parameterization

8.1 Introduction

8.1.1 Operational cloud parameterizations

Numerical models of the atmosphere have been a boon to operational meteorologists since the introduction of the first routine numerical weather forecasts in the 1950s (Charney et al. 1950). While the complexity of numerical models has increased greatly since then, these models still represent the atmosphere at discrete grid points (Richardson 1922), rather than as a continuous fluid. Because of the discrete nature of these models, parameterizations are needed to account for processes that occur on spatial scales smaller than the model grid box. Boundary-layer turbulence and the width of cumulus clouds are examples of processes that occur at scales smaller than the typical horizontal grid spacing used in both operational climate and forecast models.

Most convective parameterizations represent the large-scale effects of populations of deep cumuli that form due to large-scale instabilities or forcings in the atmosphere. These deep clouds relieve convective instabilities by moving relatively warm air from near the surface to high in the troposphere, sometimes also producing precipitation, and by creating compensating subsidence around the clouds.

The deep-cumuli parameterizations used in operational models can be broken into two main groups: those based on a cloud model, and those based on adjustment theory. Parameterizations that use cloud models can be further broken into two camps: those that use a simple entraining-detraining cloud model, and those that use a stochastic cloud model. Parameterizations based on entraining-detraining clouds often use a mass-flux approximation to describe the cloud-layer fluxes (Malkus 1958; Betts 1975, 1976; Schneider and Lindzen 1976). The premise of the mass-flux approximation is that cloud turrets dominate the transfer of heat, moisture and momentum in the cloud layer extending from cloud base to cloud top. Kuo (1965, 1974) developed a scheme for deep cumuli that uses an entraining cloud model. He used moisture convergence in the lower levels to trigger the formation of clouds. Arakawa and Schubert (1974) introduced a new

parameterization for cumuli. They used different cloud types, each with a different entrainment rate. Tiedtke (1989) developed a mass-flux parameterization for a large range of convective clouds. He defined two different entrainment rates, one for penetrative convection and one for trade-wind cumuli. However, he ignored very shallow clouds. Grell et al. (1991) and Grell (1993) introduced a parameterization similar to that of Arakawa and Schubert (1974), but assumed all deep clouds are the same size. Recently, Lappen and Randall (2001) have developed a parameterization with a coupled cumulus model and a higher-order turbulence closure scheme. Their efforts focus on producing a coupled parameterization so that boundary-layer turbulence and the cumuli are linked in the model.

Other authors have used stochastic cloud models. Raymond and Blyth (1986) describe a parameterization where discrete mixing events between cloudy and clear air occur in random fashion. The cloud is represented by a group of parcels that mix with the environment and move to their level of neutral buoyancy after mixing. Emanuel (1991), developed a parameterization similar to Raymond and Blyth (1986), but he included effects of precipitation and allowed mixtures to move to the level at which the equivalent potential temperature (θ_e) of the mixture is the same as the θ_e of the environment. Hu (1997) refined the work of Raymond and Blyth (1986) and Emanuel (1991) by allowing different numbers of mixtures as well as using Convective Available Potential Energy (CAPE) to control the development of thermals. Kain and Fritsch (1990) introduced a scheme based on stochastic mixing for use in mesoscale numerical models. In their scheme the buoyancy of the mixture determines whether the parcel remains part of the cloud or is detrained and becomes part of the environment. Bechtold et al. (2001) extended the Kain-Fritsch scheme to include both deep and shallow cumuli.

The effects of deep cumuli can also be parameterized using an adjustment scheme. In these schemes the atmosphere is adjusted to some predetermined reference state; either dry or moist adiabatic, over some adjustment time interval. An early adjustment scheme was developed by Manabe et al. (1965). Betts (1986) and Betts and Miller (1986) developed an adjustment scheme

using two reference states based on observations, one for shallow convection and one for deep convection.

Statistical parameterizations, the basis of this chapter, are commonly used in operational models to explicitly predict the total cloud cover, which is critical for calculating the surface energy balance. Using a relative-humidity threshold to predict cloud cover is a simple example. Sommeria and Deardorff (1977) proposed a statistical scheme based on the mean saturation deficit normalized by the standard deviation of the saturation deficit. They assumed a Gaussian distribution and integrated a fraction of that distribution to obtain cloud cover. Mellor (1977) further developed the scheme of Sommeria and Deardorff. Sundqvist (1978) introduced a statistically based scheme where liquid-water content was treated as a prognostic variable in the operational model. Bony and Emanuel (2001) suggest a scheme with a distribution of total water content that can range from Gaussian to a skewed distribution. Other authors (e. g. Slingo 1987; Smith 1990; Xu and Krueger 1991) have proposed methods to estimate cloud cover based on a distribution of relative humidity within a model grid cell. Neggers et al. (2002) developed a scheme similar to the Cumulus Potential (CuP) scheme, which is based on a distribution of parcels. They used a cloud-base height distribution of parcels generated from LES. Xu and Randall (1996) suggested weaknesses in statistical schemes, which were originally proposed for cloud-resolving models, and methods based on relative humidity.

A new statistical scheme to predict cloud cover and cloud-size distributions of shallow cumuli is introduced in this Chapter. It will be calibrated using data from the Barbados Oceanographic and Meteorological Experiment (BOMEX) and BLX96.

8.1.2 Specialized parameterizations for shallow cumuli

In addition to general parameterizations designed for use in operational forecast models, many studies have used specialized cloud parameterizations to examine the behavior of the cloud-topped boundary layer. Malkus (1954, 1958) divided the trade wind boundary layer into cloud

and sub-cloud layers. Betts (1973, 1976) studied boundary-layer cumuli in the tropics. Albrecht (1979) developed a model for trade-wind cumuli using a mass-flux parameterization, a well-mixed sub-cloud layer, and a cloud layer. Albrecht (1981) and Wang and Albrecht (1986, 1990) extended the work of Albrecht (1979) to maritime stratocumuli-topped boundary layers. They used their models to study the breakup of stratocumuli. However, Bretherton (1993) showed that these studies were very sensitive to the chosen values of free parameters. Haiden (1996) has generalized the Albrecht (1981) expressions for cloud cover.

Other research has been conducted to model cumuli onset time. Wilde et al. (1985) developed a model to predict boundary-layer cloud onset time based on the entrainment zone thickness and on the range of z_{LCL} of the boundary layer thermals. Wetzel (1990) suggested a parcel method to determine the boundary-layer cloud cover. He assumed that mixing of parcels with environment air leads to parcels that rise to various heights. However, aircraft observations made by Crum and Stull (1987) indicate that the core of boundary-layer thermals remain unmixed. Haiden (1997) has developed an analytical model to predict the cumulus onset time.

Large Eddy Simulation (LES) has also been used to explore the behavior of boundary-layer cumuli. A group of researchers have been conducting comparison studies using a number of different LES models to study tropical clouds (Siebesma et al. 2001), continental clouds (Brown et al. 2001), and the transition from stratocumuli to cumuli in the trade wind regions (Stevens et al. 2001).

8.2 An overview of cloud entrainment and detrainment rates

The primary disadvantage of an entraining-detraining cloud model is that entrained air is assumed to mix instantly and uniformly across the whole diameter of the cloud, contrary to the findings of Crum and Stull (1987) of an undiluted core. Also entrainment (ε) and detrainment (δ) rates are needed. Unfortunately, there is little theoretical guidance on appropriate ε and δ values. Based on similarity relationships and plume theory, Stommel (1947) suggested that the entrainment rate is a function of cloud size, such that $\varepsilon = (1/m)(dm/dz)$, where m is the cloud mass. Warner

(1970) reported that entraining plume models of clouds, using a relationship like that proposed by Stommel, could not simultaneously predict accurate values of cloud-top height and cloud-liquid water content. Simpson (1971) argues that Warner's results were flawed because he ignored precipitation. These early studies did not include the effects of detrainment on the clouds or the environment.

Other authors have proposed both entrainment and detrainment rates for clouds. Arakawa and Schubert (1974) suggested a different ε for each cloud type. In their parameterization, clouds entrain while rising and detrain in a thin layer at cloud top. Tiedtke (1989) used a constant value of ε and δ ($\varepsilon = \delta = 3 \times 10^{-4} \text{ m}^{-1}$) for shallow cumuli. These values were chosen to be consistent with values determined using the entraining plume model suggested by Simpson (1971). Siebesma and Cuijpers (1995) and Siebesma and Holtslag (1996) found, using LES of the Barbados Oceanographic and Meteorological Experiment (BOMEX), that the values of Tiedtke are an order of magnitude too small. In addition, they found that ε and δ were not equal. They suggest that, within the cloud layer,

$$\begin{aligned}\varepsilon &\approx 1.5 - 2.5 (\times 10^{-3} \text{ m}^{-1}), \text{ and} \\ \delta &\approx 2.5 - 3.0 (\times 10^{-3} \text{ m}^{-1})\end{aligned}\tag{8.1}$$

for shallow cumuli. Siebesma et al. (2001) reported values from thirteen different LES close to the range given by (8.1). However, their results suggest that ε and δ could be functions of height. In this study, values of ε and δ used with the entraining-detraining cloud model were chosen to be consistent with the results of Siebesma et al. (2001) and are assumed to be constant with height, such that $\varepsilon = 1.0 \times 10^{-3} \text{ m}^{-1}$ and $\delta = 3.0 \times 10^{-3} \text{ m}^{-1}$. However, caution is needed because it is not clear that ε and δ are universal values. They could depend on various details of both cloud dynamics and thermodynamics. For example, during BLX96 ε and δ could be different from those during BOMEX because the thermals are larger due to the deeper mixed layer and there is more wind shear in the trade wind boundary layer. The advantage of using the values given by (8.1) in this study is that results found are theoretically more robust than if new estimates of ε and

δ were made using data from BLX96. Further implications of these choices will be examined in section 8.4.

Stochastic models, like those of Raymond and Blyth (1986), Kain and Fritsch (1990) Emanuel (1991), and Hu (1996) do not require explicit values of ε and δ , but the amount of undiluted air within the cloud, also called the undilute eroding rate (Ming and Austin 2002), must be defined. In these models saturated mixtures remain with the cloud, unsaturated mixtures do not. However, they must parameterize or assume the mixing distribution. A stochastic model was not used in this study because it is more difficult to predict a cloud lifetime when the time scale for mixing is undefined.

8.3 A new scheme: The cumulus potential model

A new statistical scheme, based on the potential of boundary-layer parcels to form clouds, is developed in this section. This Cumulus Potential (CuP) scheme is one way of coupling the clear and cloudy portions of the boundary layer. This scheme has several key features: (1) cloud cover is determined by properties of the convective boundary layer, (2) cloud-base mass flux is determined from the properties of the convective boundary layer, (3) a range of cloud-top heights, cloud-base heights, and cloud thicknesses are predicted, and (4) a unique layer is predicted that consists of both clear and cloudy updrafts.

The CuP parameterization consists of two independent modules. One represents boundary-layer physics, the other represents clouds. The boundary-layer physics are represented using JFDs of θ vs. r . These JFDs provide a compact way to represent the net effects of boundary-layer turbulence. Methods used to describe and parameterize these JFDs can be found in Chapters 5 and 6. The CuP parameterization is similar to the parameterizations proposed by Sommeria and Deardorff (1977) and Mellor (1977) who also used JFDs to predict cloud cover, but there are some important differences. The CuP parameterization uses tilted JFDs to determine if a parcel in the boundary layer will rise and form a cloud, while the method of Sommeria and Deardorff (1977) used nontilted JFDs of the saturation deficit in the cloud layer to determine cloud

cover. Two types of cloud models have been tested with the CuP scheme: one is an adiabatic cloud model where cloud properties are predicted assuming an adiabatic ascent, and one is an entraining-detraining cloud model where mixing occurs with the environment as the cloud rises.

Essentially, the CuP scheme examines each parcel in the boundary layer over a heterogeneous surface, determines if that parcel will rise, and then, if the parcel does rise, determines if that parcel will rise high enough to form a cloud, as illustrated in Figure 8.1. Those parcels that are warmer than the environment will rise, and the warmest parcels should rise the highest. However, if a warm parcel is also dry, it still may not reach its z_{LCL} , so it will remain a clear-air updraft. A cooler parcel, but one that is still warmer than the environment, might not rise as high, but might be more moist so that it rises to its individual z_{LCL} . The water vapor in the parcel will condense and a cloud will form. The parcel will continue to rise as a cloudy parcel. As shown in Figure 8.1, there is a range of both cloud-base heights and cloud-top heights. There is also a range where some rising parcels are cloudy and some parcels are clear. The variation of cloud-base heights over heterogeneous land surfaces are an every-day occurrence as observed by general-aviation pilots flying near cloud base (Stull, personal communication), even though the same cloud fields as observed by human observers on the ground appear to have a uniform, single cloud-base altitude.

The virtual potential temperature (θ_v) and moisture of these boundary-layer parcels can be combined to form a JFD. Each bin of the JFD represents a parcel, or group of parcels, with a unique θ_v and moisture. That JFD can be compared to the mean environmental profile of θ_v (Figure 8.2). The mean profile of θ_v divides the JFD into as many as three sectors. The first sector (labeled 1 in Figure 8.2) consists of parcels that are less buoyant than the average mixed-layer environment. These parcels do not rise due to their own buoyancy. The second sector (labeled 2 in Figure 8.2) are parcels that are warmer than the environment, and would rise. However, they are also relatively dry. If these parcels are allowed to rise to their Level of Neutral Buoyancy (LNB), they will stop rising before reaching their z_{LCL} . Thus, parcels in this sector

remain clear-air updrafts. Parcels in the third sector (labeled 3 in Figure 8.2) are those parcels that are warmer than the environment and are also relatively moist. These parcels will rise, reach their z_{LCL} , the water vapor in the parcel will condense and the parcel will continue to rise as a cloudy parcel. The relative amount of air parcels in this third sector gives the fraction of boundary-layer parcels that form clouds, and is related to both the cloud cover and the cloud-base mass flux.

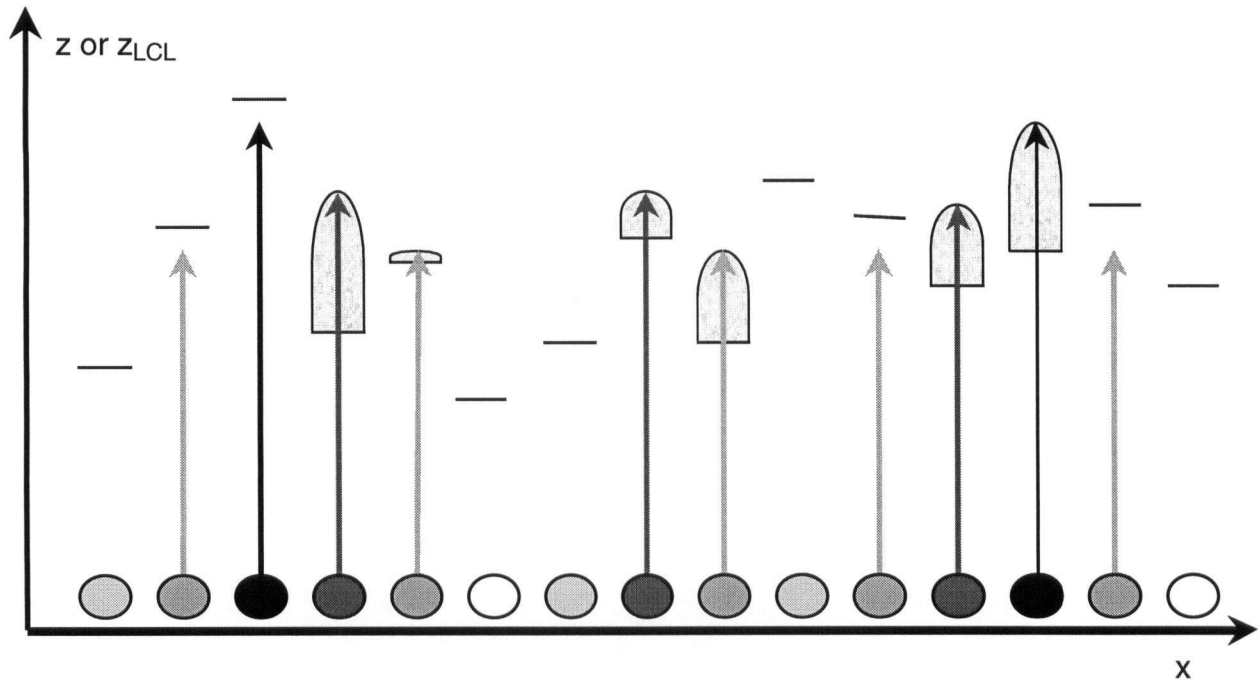


Figure 8.1. Sketch of a group of near-surface boundary-layer parcels over a heterogeneous surface. The shading of each parcel represents its virtual temperature (darker are warmer). Dashes aloft represent the z_{LCL} for each parcel. The arrows indicate how high each parcel will rise. Those parcels that rise above their z_{LCL} are marked with a cloud. Some parcels are too cool to rise at all.

On very windy days, mechanically (shear) generated turbulence can force some of the negatively buoyant parcels from sector one to rise. These cooler air parcels often have a wide range of humidities resulting in clouds with low, irregular cloud bases. These clouds are called “cumulus fractus” clouds (i.e. “scud” clouds) and will not be studied here.

The CuP model, as described above, compares JFDs of θ_v vs. z_{LCL} to the profile of θ_v to predict cloud cover and cloud-height distributions. However, the JFD parameterizations

introduced in Chapter 6, predicts JFDs of θ vs. r , not θ_v vs. z_{LCL} . While z_{LCL} is the most convenient moisture variable to use when describing the CuP scheme, r is easier to apply in the numerics of the scheme. More importantly, it was convenient to frame the JFD parameterization in terms of θ and r because these two variables are directly related to the surface energy balance. JFDs of θ vs. r can be converted into JFDs of θ_v vs. r_{LCL} (r at z_{LCL}), or values of θ_v can be calculated within the CuP scheme using values of θ and r .

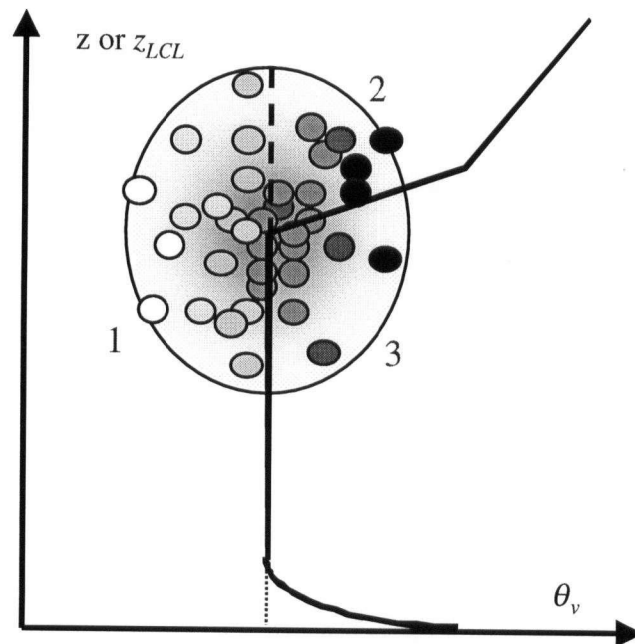


Figure 8.2. Observed θ_v and z_{LCL} for individual parcels (small circles) along with the mean environmental profile (heavy solid line). The heavy broken line extends the mixed layer θ_v over a larger range of heights and is for reference. The meaning of the three sectors is described in the text.

8.3.1 *Cloud-base and cloud-top height*

Figure 8.2 can be modified to demonstrate the differences between the two cloud models proposed here, and how cloud-base and cloud-top heights are determined in the CuP scheme (Figure 8.3). Two different parcels are highlighted, one in sector 2 (Figure 8.3a), one in sector 3 (Figure 8.3b). First, do not forget that the JFDs in Figure 8.3 represents air parcels that physically

are in the surface layer (near the ground). Both of these parcels start to rise from the surface layer. The height to which the parcel will rise depends on the cloud model and the method used to stop the parcel, either the level of neutral buoyancy, or the level at which all the CAPE was dissipated. If the level of neutral buoyancy is used to stop the parcel from sector 2, then no cloud forms. If that parcel is allowed to rise until its CAPE is dissipated, a cloud forms. When the parcel in sector 3 starts to rise, it becomes saturated, and continues to rise as a cloud regardless of the method used to stop the parcel.

When adiabatic or entraining-detraining parcels are allowed to rise to their LNB, cloud cover is very small and the clouds are very thin. When CAPE is used to stop adiabatic cloudy parcels, there are several cases where the modeled clouds reach the top of the soundings measured during BLX96, which were higher than the observed clouds. Special, extended soundings were created by combining soundings flown during BLX96 and soundings produced from the initialization of the Rapid Update Cycle (RUC) model. The RUC initializations did not occur at the same times as BLX96 soundings, so the RUC profiles were linearly interpolated in time. Although interpolation of mixed-layer profiles is difficult because of the change of the inversion height with time, linear interpolation of the free atmosphere is more reliable given the quiescent conditions during BLX96. These non-entraining parcels still did not reach their LNB in the RUC model domain, which was approximately 15 km high. Therefore, only results from the entraining-detraining cloud model will be shown.

Cloud-top height predicted by the entraining-detraining cloud model is also a function of both the entrainment (ϵ) and detrainment (δ) rates as well as the method used to stop the clouds. The values of ϵ and δ were chosen to be consistent with Siebesma and Cuijpers (1995) and Siebesma et al. (2001) ($\epsilon = 1.0 \times 10^{-3} \text{ m}^{-1}$ and $\delta = 3.0 \times 10^{-3} \text{ m}^{-1}$) and are discussed in section 8.4. The differences in the heights predicted by adiabatic and the entraining-detraining cloud models are shown in Figure 8.3.

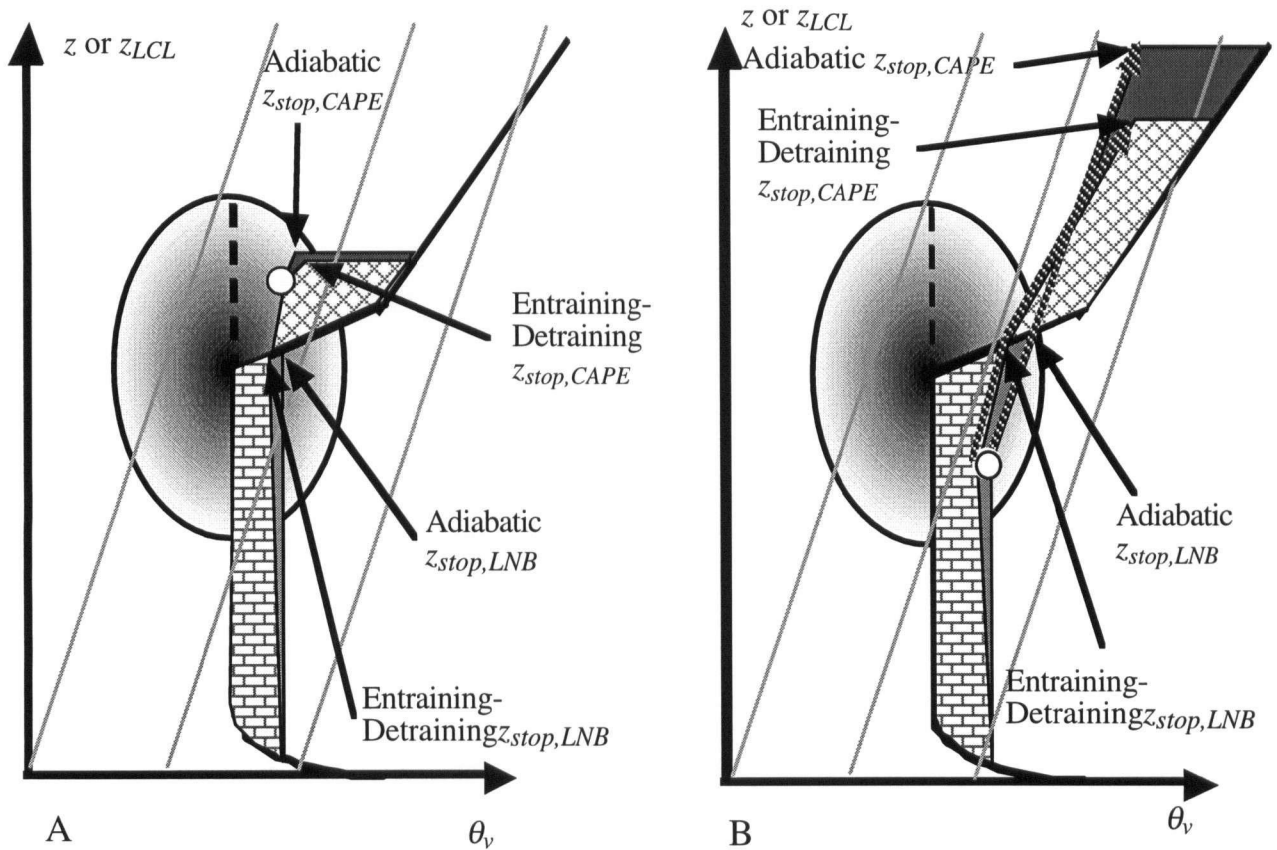


Figure 8.3. Plot similar to 8.2, but with only (A) a single parcel from sector 2 and (B) a single parcel from sector 3. Solid fill indicates CAPE or the dissipation of CAPE for adiabatic ascent, patterns indicates CAPE or the dissipation of CAPE for entraining-detraining ascent. The thin lines are moist adiabats, thick striped lines in (B) show cloudy ascent.

8.3.2. Cloud-cover fraction

The arguments of the previous subsections tell us about the birth rate of new clouds triggered by active thermals. However, once a cloud exists, it might have a lifetime independent of the thermal lifetime. These lingering clouds add to the cloud cover.

The portion of air parcels within sectors 2 and 3 of the JFD predicts the fraction of the near-surface boundary layer air that is rising over some time interval. The traditional boundary-layer time scale, $t_* = z_i/w_*$, gives an estimate of the relevant time scale for the birth of fair weather cumuli. A cloud birth rate can be computed from the fraction of parcels in sector 3 (α_3) divided by

t_*

$$\alpha_{cloud} = \int_0^t \frac{\alpha_3}{t_*} dt - \int_\tau^t \frac{\alpha_3}{t_*} dt, \quad (8.2)$$

where α_{cloud} is the cloud-cover fraction at some time, t , and τ is the cloud lifetime. In this simple model the cloud is assumed to form, exist for some time τ , and then disappear. This assumption also implies that the cloud birth rate and death rate are the same, so that α_3 can be used to define both. Equation (8.2) can also be written as a differential, assuming that the the cloud death rate is a function of α_{cloud} ,

$$\frac{d\alpha_{cloud}}{dt} = \frac{\alpha_3}{t_*} - \frac{\alpha_{cloud}}{\tau}, \quad (8.3)$$

If α_3 is not a function of time, or changes slowly relative to the cloud lifetimes, then (8.3) solved, yielding $\alpha_{cloud} = \alpha_3 \tau / t_*$.

This formulation is similar to that used by Albrecht (1981) and improved by Haiden (1996). In their models they assume some active cloud lifetime, where the clouds are growing and a decay time during which clouds passively mix with their environment. They define a decay time scale, which, as pointed out by Haiden, can be related to ε and δ . Compared to the relatively deep boundary-layer trade cumuli used in Albrecht's (1981) study, clouds observed during BLX96 were shallow, so that the liquid water contents were likely small, and the clouds decayed quickly. Therefore, for these shallow clouds it will be assumed that, $\tau \approx t_*$, and $\alpha_{cloud} = \alpha_3$. This gives a cloud lifetime on the order of 15 to 20 minutes for the BLX96 case study days.

More realistic estimates of τ require information about the cloud updraft, the cloud updraft velocity (w_{cloud}), ε , and δ . Simpson and Wiggert (1969) developed an equation that included the effects of pressure perturbations on the rising cloud. However, their expression involved several empirical constants that may not be universal. Grant and Brown (1999) suggest a new velocity scale for use with boundary-layer cumuli that is similar to the Deardorff velocity scale

$$w_{*,cloud} = \left(\frac{g}{\bar{\theta}_v} \delta \bar{\theta}_v m_b z_{cloud} \right)^{1/3}, \quad (8.4)$$

where g is the acceleration due to gravity, $\bar{\theta}_v$ is the layer average value θ_v , $\delta \bar{\theta}_v$ is the average

cloud buoyancy excess, and m_b is the cloud-base mass flux (normalized by density). This expression is difficult to apply to BLX96 data because negative values of CAPE are allowed. Gregory (2001) has also devised an expression for w_{cloud} , similar to that of Grant and Brown's (1999), but he allowed ε and δ to change as a function of height. However, Gregory's expression, like that of Simpson and Wiggert (1969), required empirical constants.

8.3.3. Cloud-base mass flux

Once the cloud cover at any time is determined, that fraction can be used to calculate the cloud-base mass flux (Malkus 1958; Betts 1975, 1976), which is defined to be

$$M_c = \rho_{air} w_{cloud} \alpha_{cloud} \quad (8.5)$$

where M_c is the mass flux, ρ_{air} is the density of air and w_{cloud} is the updraft velocity of the cloud. The value of ρ_{air} can be calculated from either observations or could be predicted by a model. The value of w_{cloud} could be predicted from CAPE, or w_* . No measurements of cloud-base mass flux were made during BLX96, so the accuracy of (8.5) will not be evaluated.

8.3.4 Cumuli onset time

Cumuli onset time can also be predicted by the CuP model. Cloud onset time is simply the first time of the day when α_3 becomes nonzero. Early in the day, the boundary layer is very shallow, so that none of the parcels rise to their z_{LCL} . As the day progresses, the boundary layer deepens so that clouds are more likely to form. The boundary layer may also dry or moisten with time, so that the formation of clouds can be either encouraged or discouraged. This definition is similar to that proposed by Wetzell (1990) and Haiden (1997), but with the improvement that an actual, or parameterized (Chapter 5) JFD can be used. However, each research flight started in the late morning after the cumuli had formed, so the BLX96 data can not be used to estimate the cloud onset time.

8.4 Calibration of Entrainment and Detrainment Rates Against BOMEX

The data collected during BLX96 is not ideal for evaluating values of ε and δ because of

the lack of observations in the cloud layer. LES results based on observations from phase three (22 to 23 June 1969) of the Barbados Oceanographic and Meteorological Experiment (BOMEX) (Holland and Rasmusson 1973) provide an opportunity to evaluate values of ε and δ . The observed mean profiles (Figure 8.4), measured surface fluxes, along with LES estimates of entrainment zone fluxes were obtained from Siebesma et al. (2001). These variables were used to create a JFD using the parameterizations introduced in Chapter 6 (Figure 8.5). Because BOMEX was over the ocean, the surface was relatively homogeneous, the spread of θ and r was narrow (Figure 8.5). The mean profiles of θ_v , and r , and surface fluxes during BOMEX were approximately steady-state, so only one value of cloud cover is obtained for this comparison study. Values of the variables needed to drive the CuP scheme for the BOMEX comparison can be found in Appendix G.

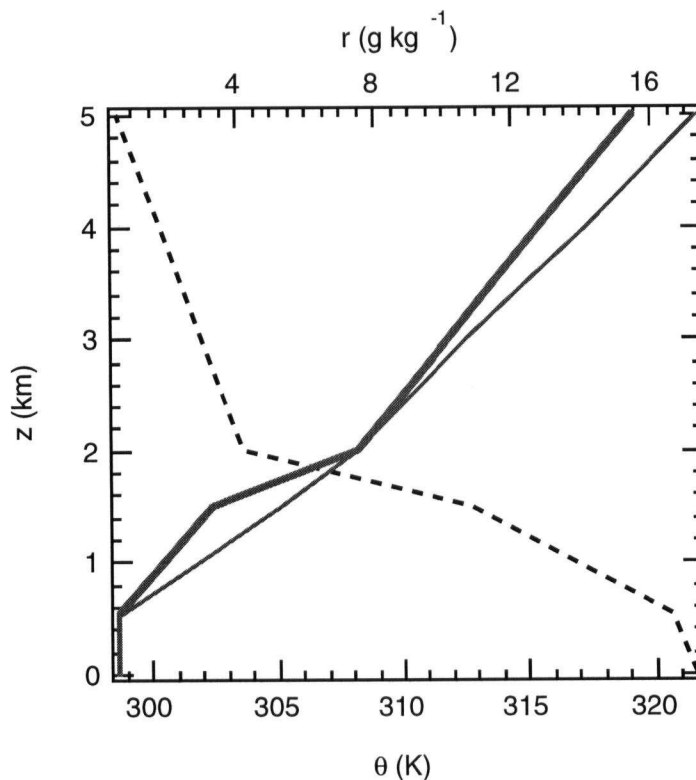


Figure 8.4 Profiles of θ (heavy solid line) and r (broken line) observed during BOMEX. The thin solid line is a moist adiabat.

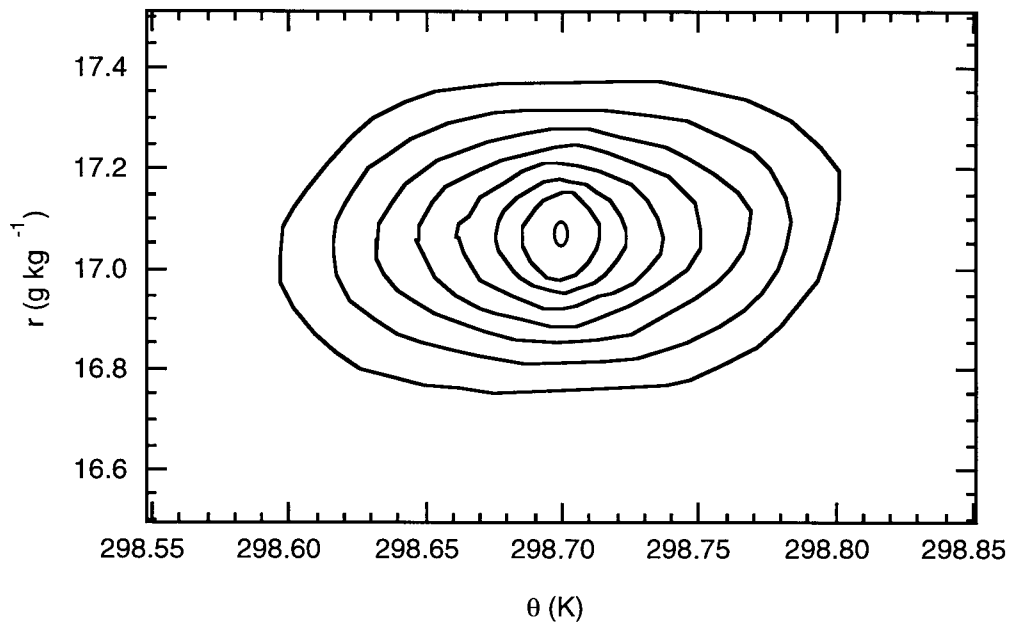


Figure 8.5 Parameterized JFD for the BOMEX case. The first contour marks a normalized frequency of 0.02, and the contour interval is 0.02.

While the predictions of cloud-base and cloud-top heights by the CuP parameterization and the LES are similar there are large differences in predicted cloud cover at each height (Figure 8.6). To be classified as belonging to cloud core, the LES grid point value had to have liquid water and positive buoyancy. The total cloud amount reported by LES includes those grid points that have liquid water and either positive or negative buoyancy. Even the LES total cloud amount is much smaller than the CuP results at all heights with clouds. However, the average observed cloud amount reported by Delnore (1972), based on bridge reports from the research ships, was six tenths, much larger than the 12% predicted by LES. This amount was for the entire phase 3 of BOMEX (20 June to 1 August), so individual days might have had more or less cloud cover. Nitta (1975) shows a surface weather map for 12 UTC 22 June 1969 with overcast conditions at the center of the BOMEX ship array cover ranging from nine-tenths to one-tenth east of the BOMEX ships. Some possible reasons for the differences between the LES and the CuP scheme are discussed in section 8.6.2.

Although there were few cloud observations made during BOMEX, CuP model results can be compared to LES results presented by Siebesma et al. (2001) and the values of ϵ and δ used in the CuP scheme can be evaluated. The LES reports two different values of cloud amount, cloud core amount and total cloud amount. The cloud base-height predicted by the CuP scheme agrees well with the LES predictions (Figure 8.6). There is also good agreement for the highest cloud tops predicted by the CuP scheme, which stops the highest clouds near an altitude of 1.9 km, and the LES, which stops most of the clouds near an altitude of 2 km. The good agreement between the LES cloud heights and the CuP cloud heights suggests that the choice of ϵ and δ used in the CuP scheme is appropriate ($\epsilon = 1.0 \times 10^{-3} \text{ m}^{-1}$ and $\delta = 3.0 \times 10^{-3} \text{ m}^{-1}$). However, von Salzen and McFarlane (2002) point out that cloud tops on 22 and 23 June were likely higher than reported by LES.

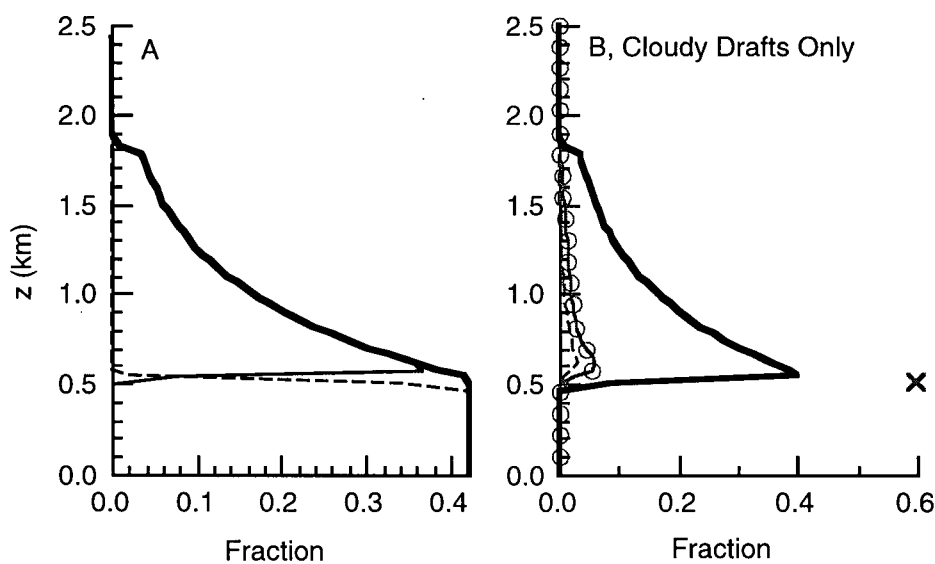


Figure 8.6 (A) Total updraft fraction (thick line), cloudy updraft fraction (thin line) and clear updraft fraction (dashed line) predicted by the CuP model for BOMEX. (B) Cloud fraction predicted by the CuP model (thick line), LES cloud core (dashed line), LES total cloud (line with circles) of Siebesma et al. (2001) and average BOMEX cloud cover (X) reported by Delnore (1972).

8.4.1 Evaluation of entrainment and detrainment rates

The values of ε and δ are important for two reasons: mixing effects the thermodynamic properties of the clouds, which determine how high a cloud will rise, and they also control the removal of mass from the clouds. The effect of ε and δ on the thermodynamic properties of the clouds is highlighted in Figure (8.7). In this case δ was held to a constant value of $3.0 \times 10^{-3} \text{ m}^{-1}$, while ε was allowed to range from $1.0 \times 10^{-7} \text{ m}^{-1}$ to $2.0 \times 10^{-3} \text{ m}^{-1}$. Given a larger value of ε , clouds should lie closer to the mean profile. In the layer reaching from 0.5 to 1.5 km this is the case. Above 1.5 km, larger values ε give cloud values of θ_v that are actually further away from the mean profile. Similar behavior is not seen in the plot of r . This behavior in θ_v occurs because θ_v is not conserved in the cloudy environment. However, equivalent potential temperature (θ_e) is, and an examination of θ_e shows that it is pulled towards the environment value of θ_e and is conserved in the rising cloud for the case where $\varepsilon = 1.0 \times 10^{-7} \text{ m}^{-1}$ (not shown).

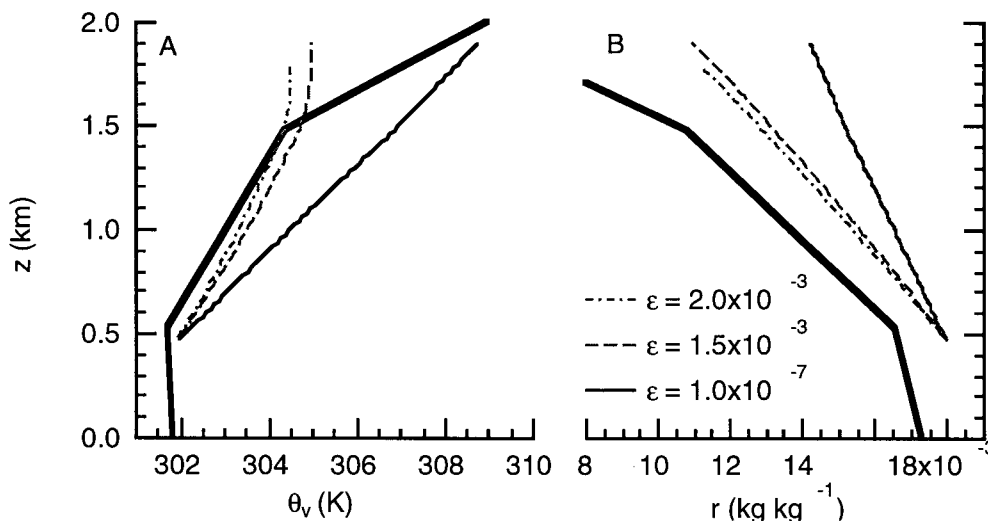


Figure 8.7. Plot of (A) θ_v vs. height and (B) r vs. height (B) for BOMEX (heavy lines). In each case, thin lines show θ_v or r for a sample parcel given $\varepsilon = 2.0 \times 10^{-3} \text{ m}^{-1}$ (dot-dashed), $\varepsilon = 1.5 \times 10^{-3} \text{ m}^{-1}$ (dashed), and $\varepsilon = 1.0 \times 10^{-7} \text{ m}^{-1}$ (thin solid line).

If δ is greater than ε then the cloud cover will decrease with height because mass is being removed from the clouds. In contrast, mass was not removed from the boundary-layer thermals. This might appear inconsistent, but as shown in Chapter 4, the fractional coverage due to updrafts and downdrafts is approximately constant through most of the mixed layer. One reason for this is that air detrained from the thermal is still buoyant relative to the mixed layer and should continue to rise with the thermal, but is likely to be negatively buoyant relative to the cloud layer.

8.5 Alternate methods of predicting cloud cover

In addition to cloud-cover estimates made using the CuP scheme, we will show for comparison estimates made using three other schemes: (1) the relative-humidity based scheme used in the ECHAM4 global climate model (Roeckner et al. 1996), (2) the statistical scheme suggested by Sommeria and Deardorff (1977), and (3) the scheme suggested by Albrecht (1981) for trade-cumuli.

The parameterization used by Roeckner et al. (1996) for cloud cover is

$$\alpha_{cloud} = 1 - \sqrt{1 - \frac{RH - RH_{cr}}{1 - RH_{cr}}} \quad (8.6)$$

where RH is the relative humidity, and RH_{cr} is a critical value of RH used to determine if air in the grid box is saturated and is a function of height

$$RH_{cr} = RH_{0,top} + (RH_{0,sfc} - RH_{0,top}) \exp\left[1 - (p_s/p)^n\right], \quad (8.7)$$

where p_s is the surface pressure, p is the pressure, n was determined to be 4, and $RH_{0,top} = 0.6$, $RH_{0,sfc} = 0.99$ and represent the upper and lower critical values of RH . The values of $RH_{0,top}$ and $RH_{0,sfc}$ represent the value of RH needed for cloud cover. For example, at the surface, the exponential function in (8.7) becomes 1, and $RH_{cr} = RH_{0,sfc}$, so that RH must be greater than 0.99 for there to be cloud cover. Higher in the atmosphere, the second term becomes small, and a RH greater than only 0.6 is needed for some cloud cover.

Sommeria and Deardorff (1977) postulated that cloud cover can be inferred using JFDs of

the normalized saturation deficit, which they defined as

$$Q = \bar{s} / \sigma_s, \quad (8.8)$$

where $s = r_{total} - r_s(T)$, r_{total} is the total water mixing ratio, and σ_s is the standard deviation associated with the distribution of s . The value of σ_s was assumed to be 0.8 g kg^{-1} , as suggested by Siebesma et al. (2001). Assuming a Gaussian distribution to s , (8.8) can be integrated to give an estimate of the cloud cover

$$\alpha_{cloud} = \frac{1}{2} \left[1 + \text{erf} \left(\frac{Q}{\sqrt{2}} \right) \right]. \quad (8.9)$$

Albrecht (1981) suggests an expression for cloud cover based on the active lifetime and the decay time for clouds in the maritime boundary layer. He suggests

$$\alpha_{cloud} = \frac{\tau'}{\tau_0} \left(\frac{r_{total} - r_{s,env}}{r_{total} - r_{env}} \right), \quad (8.10)$$

where $r_{s,env}$ is r_s of the environment, r_{env} is the r of the environment, τ' is the decay time constant, and τ_0 is the time constant for the active phase of the clouds. Albrecht argues that $\tau' \approx \tau_0$.

8.6 Results of the CuP Model for BLX96

The CuP scheme was used to generate estimates of cloud-top, cloud-base height and cloud cover for all BLX96 case study days, with the exception of the last legs flown on 16 July. As described in Chapter 2, these legs were not included because of suspect values of the moisture flux measured during the last near-surface leg. Cloud estimates could be made for each horizontal leg, for which a measured JFD existed but a sounding did not, or for each sounding, for which a JFD would have to be determined. Interpolation of boundary-layer soundings is complicated by the jump at the top of the mixed layer, and the potential for non-linear growth of the boundary layer. It was determined that interpolating the JFDs to the proper time using the parameterizations developed in Chapter 6, rather than attempting to interpolate the soundings, would yield the best results.

The soundings used with the CuP scheme were linear fits by eye to the averaged soundings measured during BLX96 (Chapter 2). The fits were constructed so that each sounding could have several layers over which observations changed in a nearly linear fashion. Parameterized JFDs were constructed for a height of $0.5z_i$, and at a time corresponding to the sounding times. These JFDs were generated using the mixing-diagram parameterization described in Chapter 6, using (6.6) to find the slope of the surface axis, the observed entrainment zone jumps to find the slope of the entrainment-zone axis, and (6.13a) and (6.13b) to predict the spread along each axis. The height $0.5z_i$ was chosen for height of the JFDs because the scatter in the standard deviations was small, and the thermals, some of which rise to form clouds, are readily apparent at that altitude. The clear-air parcels were also allowed to entrain air from $0.5z_i$ to the altitude at which they stopped or became clouds, at which point the cloud model was applied (section 8.3.1).

8.6.1 Cloud-top and cloud-base height

There is good agreement between the observed cloud-base height and the cloud-base height predicted by the CuP scheme (Figure 8.8). The range of cloud-base heights predicted on any given day is not large, ranging from 40 m to 240 m during BLX96. The level of agreement found for cloud-base height is not surprising; Stull and Eloranta (1985) found that the value of z_{LCL} calculated from surface layer air did a good job predicting the cloud-base height of boundary-layer cumuli as precisely observed using lidar. The agreement between the observed cloud-top height and the CuP-scheme predicted mode cloud-top height is not as good. The methodology used to measure the cloud-top height during BLX96 could be responsible for this result. Cloud-top height was logged two different ways: by the airborne scientists during the slant soundings, and from the forward looking video camera on the King Air. Both of these methods focus on the maximum observed cloud-top height, rather than the mean or mode cloud-top height. There is better agreement between the maximum cloud-top height predicted by the CuP scheme and the observed cloud-top height (Figure 8.8). An alternative explanation is that ϵ is too large, however the

relatively good agreement between the CuP maximum cloud top and the observed cloud top suggests this is not the case.

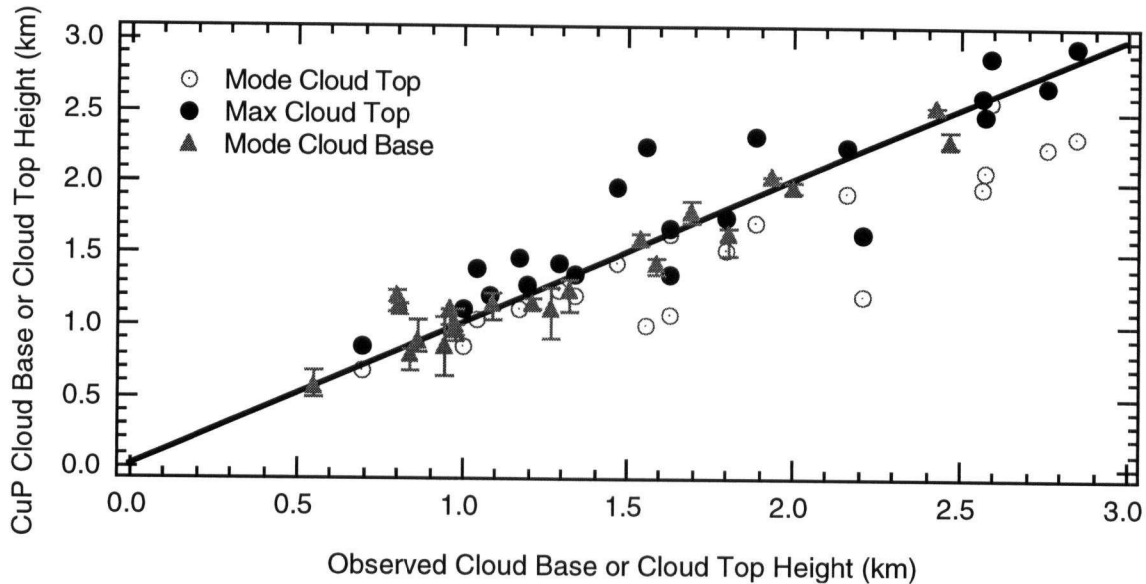


Figure 8.8 Plot of the CuP predicted mode cloud-base height vs. observed cloud-base height (triangles), with the CuP predicted range shown by the vertical error bars, CuP predicted mode cloud-top height vs. observed cloud-top height (open circles), and CuP predicted maximum cloud-top height vs. observed cloud-top height (filled circles). The solid line is the 1:1 line.

For comparison, cloud-base and cloud-top height were also calculated using the alternate methods introduced earlier in this chapter. Estimates of cloud heights were more complicated for these methods because cloud depth is not explicitly predicted. For each of the alternate methods, cloud-base height was defined to be the height at which the clouds first form and cloud-top height was defined to be the height at which clouds ceased to exist. The CuP model seemed to do the best job predicting the cloud-base height (Figure 8.9). The methods of Roeckner et al. (1996) and Sommeria and Deardorff (1977) seemed to underestimate the cloud-base height. This behavior could be due to very small cloud amounts at small heights. The method of Albrecht (1981) seems to overestimate the cloud-base height. For cloud-top height the CuP model also seems to the the

best job predicting the cloud-top height (Figure 8.10). There is more scatter in the cloud-top results of Roeckner et al., Sommeria and Deardorff, and Albrecht than for CuP cloud-top heights.

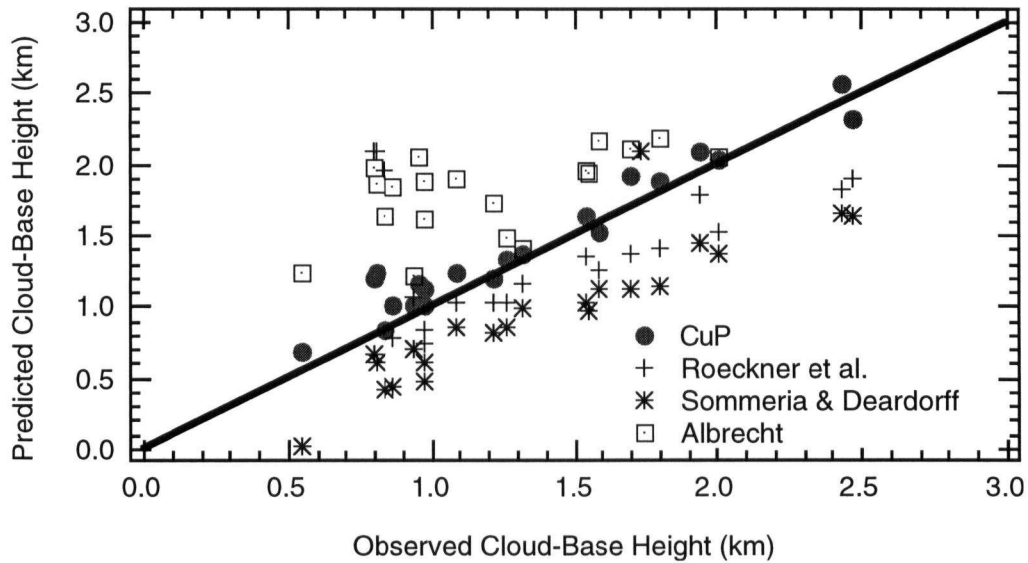


Figure 8.9 Plot of CuP (filled circles), Roeckner et al. (crosses), Sommeria and Deardorff (asterisks), and Albrecht (squares) predicted cloud-base height. vs. observed cloud-base height. The solid line is the 1:1 line

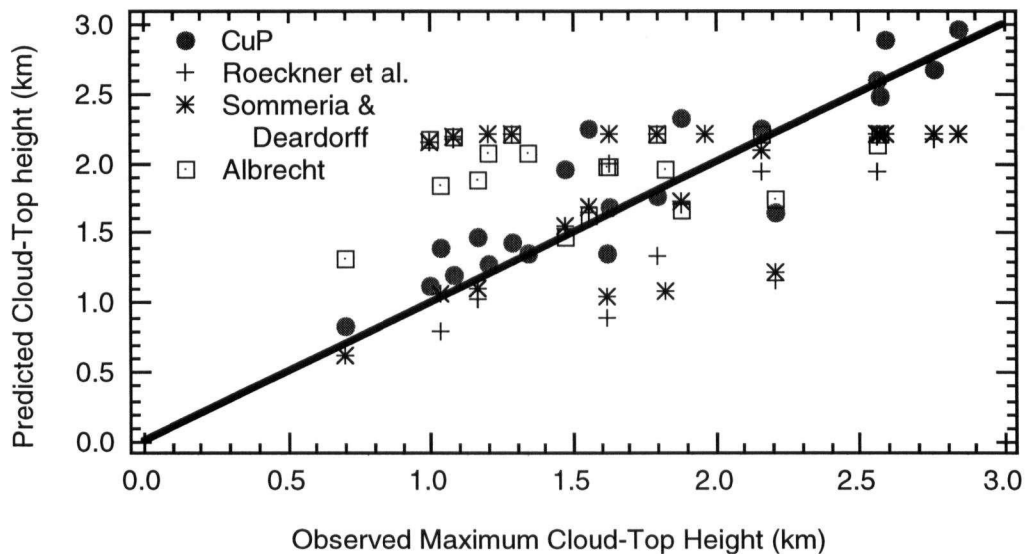


Figure 8.10 Plot of CuP (filled circles), Roeckner et al. (crosses), Sommeria and Deardorff (asterisks), and Albrecht (squares) predicted cloud-top height vs. observed maximum cloud-top height. The solid line is the 1:1 line.

One advantage of the CuP parameterization is that distributions of cloud-top height and cloud-base height are predicted. Unfortunately, detailed observations of cloud populations were not made during BLX96. Figure 8.11 shows an example of the CuP predicted cloud distributions on 28 July. At the time of the first sounding (11:40 LST), the moistest boundary-layer parcels reach their z_{LCL} near an altitude of 0.54 km, and most of the rising parcels are saturated at a height of 0.66 km. The tallest clouds reach as high as 0.78 km, but most cloudy parcels stop before reaching an altitude of 0.68 km. By the time of the second sounding (13:30 LST) the mixed layer has dried (parcels begin to reach their z_{LCL} near an altitude of 0.86 km). The tallest clouds at 13:30 LST reach as high as 1.38 km. Between 13:30 LST and 15:15 LST the boundary layer deepens, as shown by the tops of the clear thermals. The mixed layer also dries, at 15:15 LST the lowest clouds occur at an altitude of 1.1 km. The tallest clouds at 15:15 LST reach to 1.46 km, although most only reach 1.3 km. Throughout the day, the fraction of parcels that are rising remains constant, near 0.3. This indicates that although the JFD changes with time between each leg, the changes are such that the total fraction of rising parcels remains the same.

The cloud-base and cloud-top altitude predicted by the CuP model and the alternate methods can be compared to the observed cloud-base and cloud-top altitude. An example from 27 July is shown in Figure 8.12. The results from 11:30 LST are not shown because of the small amount of cloud cover. Figure 8.12 highlights the underestimation of the cloud-base height by the methods of Roeckner et al. (1996) and Sommeria and Deardorff (1977). The method of Albrecht (1981) predicts a cloud-base height and a cloud-top height that are much higher than those observed. The CuP scheme seems to do the best job predicting both the cloud-base height and cloud-top height.

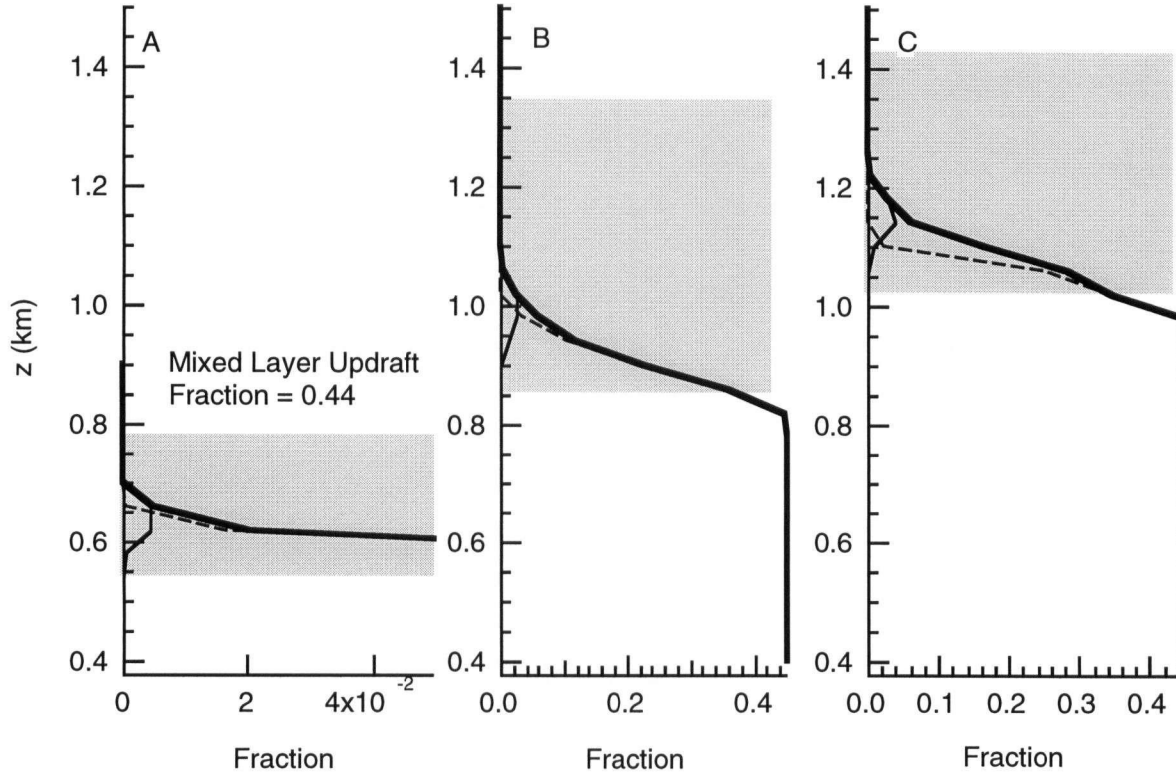


Figure 8.11 Total, cloudy and clear draft fraction vs. height for 27 July, (A) 11:30 LST, (B) 13:30 LST and (C) 15:15 LST. Shading marks the range of heights with and cloudy updrafts.

8.6.2 Cloud cover

The alternate methods described in section 8.4.1 can be used to estimate the total cloud cover. These methods show considerable scatter and indicate the difficulty predicting cloud-cover amounts (Figure 8.13). The method of Roeckner et al. (1996) shows the most scatter of the alternate methods. In general, the methods of Albrecht (1981) and Sommeria and Deardorff (1977) seem to underestimate the cloud cover.

Overall the agreement between the CuP predicted cloud cover and observations is good but there is much scatter (Figure 8.14). Many of the error bars on the observations (determined using the methods of Chapter 7) cross the 1:1 line, and over 90% of the predictions are within $\pm 10\%$ of

the observations. In addition, the errors appear to be similar in magnitude to the differences between the radiometer and the airborne scientist described in Chapter 7.

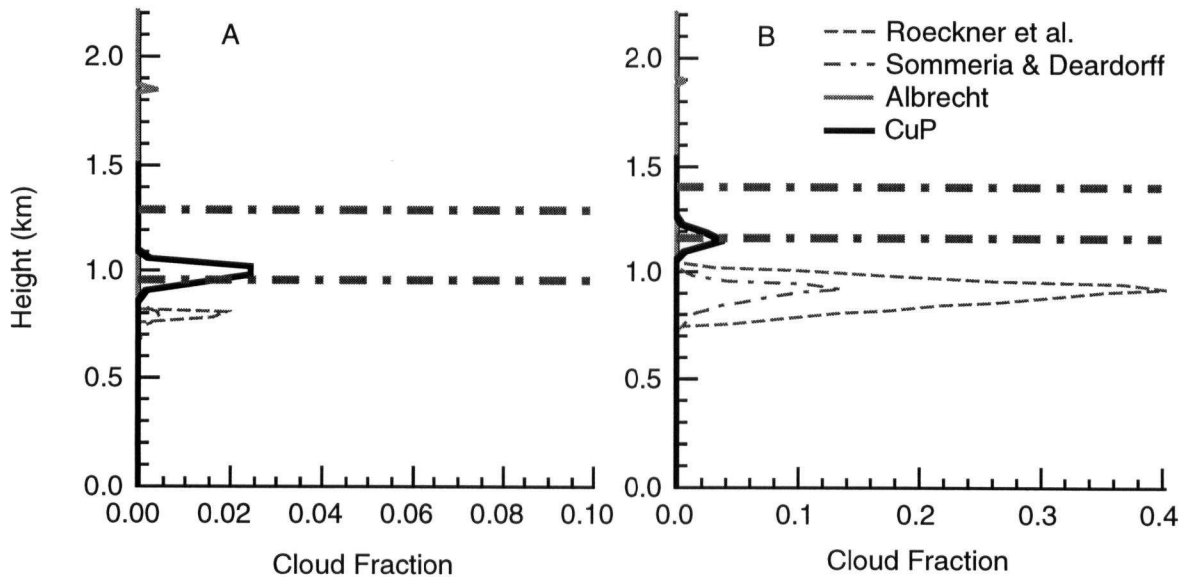


Figure 8.12. Cloudy draft fraction vs. height for 27 July, (A) 13:30 LST and (B) 15:15 LST predicted by the CuP (heavy black line), Roeckner et al. (thin dashed line), Sommeria and Deardorff (thin dot-dashed line) and Albrecht (heavy grey line). Observed cloud-base height and cloud-top height are shown by the heavy dot-dashed line.

In order to evaluate the skill of all four methods, the root-mean-square error (RMSE) can be computed. The CuP scheme and Albrecht's (1981) scheme had the lowest RMSE of the schemes tested, 0.08. The statistical scheme of Sommeria and Deardorff (1977) and the relative humidity scheme of Roeckner et al. (1996) had RMSEs of 0.11 and 0.10, respectively. The average RMSE computed from the three alternate methods was used to construct the vertical error bars in Figure (8.14).

There were a number of instances where the CuP scheme does not do a good job predicting the cloud cover. Using data from BLX96, there were some times that the CuP scheme suggests that there should be very small amounts of cloud cover, while the airborne scientist reported

amounts as large as 12%. In these cases only parcels from the extreme tails of the JFD reach their z_{LCL} before reaching the level at which their CAPE is dissipated. These cloud-cover errors could be due to shortcomings in the JFD parameterization. Either the θ or r range predicted by the parameterization could be too small, so that there are too few parcels in the tails of the distributions, or the mean θ and r of the JFD could be in error. In each case the mean of the JFD was determined from the mixed-layer mean values of θ and r . On most days, r decreased as a function of height, so the JFD centered at the mixed layer mean r could be too dry, leading to a cloud cover that is too small. Errors could also be due to errors in the linear soundings, which could increase or decrease the consumption of CAPE. An additional source of error is the choice of both ε and δ

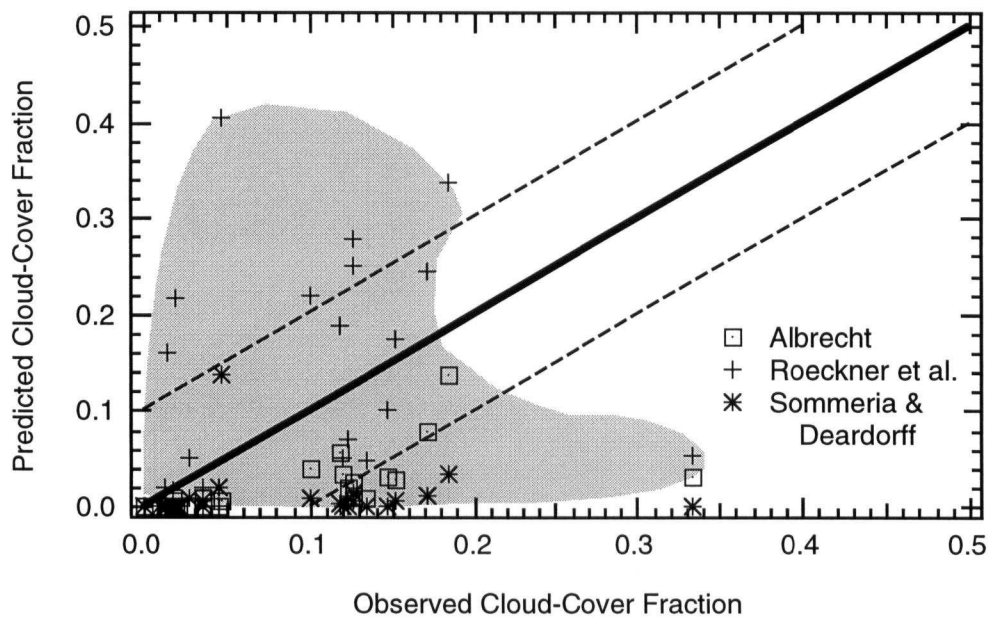


Figure 8.13 Predicted cloud-cover fraction for all BLX96 case study days using the methods of Albrecht (1981) (squares), Roeckner et al. (1996) (crosses), and Sommeria and Deardorff (1977) (asterisks) vs. observed cloud-cover fraction. Shading shows the envelope of results. The heavy solid line is the 1:1 line, the dashed lines are $\pm 10\%$ from the 1:1 line.

Other errors, particularly those where the CuP model overpredicted the cloud cover, could be related to shortcomings in the CuP parameterization, which does not include all of the relevant physical processes. For example, the CuP scheme neglects pressure gradient forces and subsidence. Both of these processes could lead to inaccuracies in the CuP predicted cloud cover.

The CuP scheme can also be used for binary prediction, simply determining if there were clouds or no clouds. Using this criterion, the CuP scheme successfully predicted cloud or no cloud cover approximately 90% of the time.

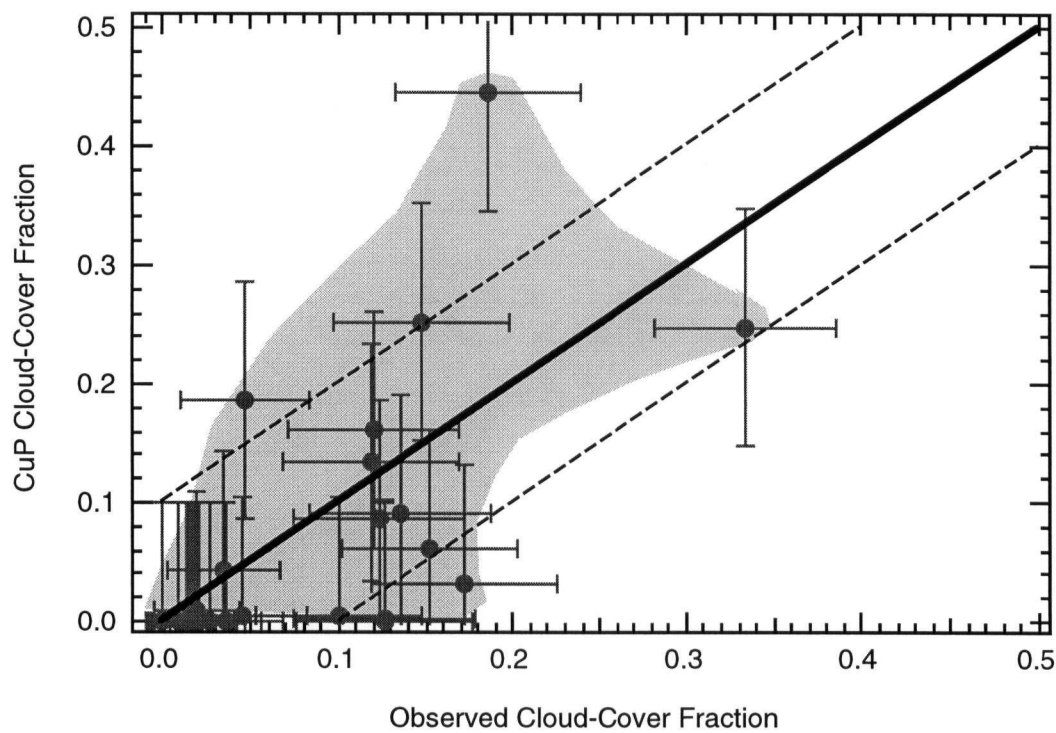


Figure 8.14 CuP predicted cloud-cover fraction vs. observed cloud-cover fraction for all BLX96 case study days. Horizontal error bars indicate likely errors in cloud-cover fraction observations, vertical error bars are calculated from the average RMSE of the alternate cloud parameterizations. Shading shows the envelope of CuP results. The heavy solid line is the 1:1 line, the dashed lines are $\pm 10\%$ from the 1:1 line.

8.7 Conclusions

A simple parameterization to predict the cloud-cover fraction and the depth distributions of boundary-layer cumuli has been introduced. This new parameterization represents a way to couple boundary-layer cumuli to boundary-layer turbulence. One important component of this parameterization is the use of JFDs of θ vs. r to represent turbulence in the boundary layer. These JFDs are converted to JFDs of θ_v vs. r_{CL} and are compared to the profile of θ_v to yield estimates of cloud-base height, cloud-top height, and cloud cover. In addition, the CuP parameterization predicts cloud-base mass flux. The mass-flux estimate could be used to drive other, more-physically-based cloud models that require some estimate of the mass flux as input.

The CuP scheme did a good job predicting cloud-base height and cloud-top height using data collected during BLX96 and using data from LES of BOMEX. The agreement between the observed and predicted cloud cover is not as good. However, the CuP scheme did a better job predicting cloud cover than two of three alternative methods and did a better job predicting cloud-base height and cloud-top height than all three alternative methods.

While the CuP parameterization shows promise, there are some aspects that warrant more investigation. The parameterization should be tested at more geographic locations, particularly over the ocean. More work is needed to better understand the lifetimes of boundary-layer cumuli, and processes, such as pressure gradient forces, that influence how high boundary-layer thermals can rise. The CuP scheme should be compared against more advanced cloud models, such as one of the stochastic cloud models, or could be combined with a stochastic model to give a realistic distribution of parcel properties. Finally, the parameterization should be applied in a single column model of the atmosphere, perhaps using BOMEX or BLX96. In this application the clouds predicted by the CuP parameterization would be allowed to interact with their environment and could change the environmental profiles of θ and r .

Cloud size distributions generated by the CuP scheme could also be compared to size distributions that have already been presented in the literature, such as the observational work by

Plank (1969), Lopez (1977), Hozumi et al. (1982), Wielicki and Welch (1986), Cahalan and Joseph (1989), Kuo et al. (1993), and Benner and Curry (1998) and cumuli size distributions from LES (Neggers et al. 2001).

Chapter 9: Conclusions and Future Work

9.1 Summary of goals, methods, and findings

The main purpose of this dissertation was to introduce a parameterization, named the Cumulus Potential (CuP) scheme, to predict fair-weather cumuli in numerical climate and weather-forecast models. This parameterization utilizes the interaction between boundary-layer turbulence and clouds using two separate modules: one module of the parameterization represents boundary-layer turbulence effects are represented by JFDs of θ vs. r , a second module is used to predicted the cloud cover, cloud-base height, and cloud-top height. This scheme, has several key features: (1) cloud cover is determined from boundary-layer JFDs of θ vs. r , (2) cloud-base mass flux is calculated from the mixed-layer JFD, (3) clear and cloudy thermals are allowed to exist at the same altitude as is observed in nature, and (4) a range of cloud-base heights, cloud-top heights, and cloud thicknesses are predicted over a heterogeneous land surface.

A new field project, named Boundary Layer Experiment 1996 (BLX96) (Chapter 2), was conducted to investigate the behavior of the JFDs, and for verification of the CuP scheme. Data was collected at a number of heights, ranging from close to the surface to $0.8 z_i$. Some of the traditional mixed-layer scales failed to adequately describe BLX96 processes, particularly the moisture scale, due to entrainment at the top of the boundary layer. A new scale was derived in Chapter 3, based on fluxes at the surface and at the entrainment zone, that can be applied to both the moisture variance and other statistics. In Chapter 4, the fraction of the BLX96 boundary layer covered by coherent drafts was shown to be a function of the criteria used to define the drafts, and profiles of updraft and downdraft moisture excesses or deficits were analyzed.

Sample JFDs computed from BLX96 data were shown in Chapter 5 to have some features in common with the JFDs observed by Schrieber et al. (1996). However, the tilt of the JFDs was found to be a function of height for BLX96. In parameterizing these JFDs, two previous methods were found to be deficient: one based on statistical techniques (Wyngaard and Moeng 1992), and one based on physical processes at the surface (Schrieber et al. 1996). So two new methods were

developed and tested: one based on the superposition of three sub-JFDs, and another based on mixing diagrams. Using the sub-JFD method, it was found that the tilt of the JFD was a function of the updraft and downdraft properties. Using the mixing-diagram method, the tilt of the JFDs was a function of the thermodynamic properties of the entrainment zone and the surface. The sub-JFD method was found to be superior to the other three parameterizations for the BLX96 data, but it is very cumbersome because of the large number of variables needed. The mixing-diagram method worked as well as the statistical method, and has the advantage of being physically based and is less sensitive to the correlation between θ and r . This latter method was used to generate parameterized JFDs for the CuP parameterization tests.

Before using this CuP scheme to estimate the cloud cover, an investigation of the likely cloud-cover measurement errors was reported in Chapter 7. In this experiment, a virtual aircraft was flown under a virtual cloud field. This work showed that the cloud-cover measurement errors were about $\pm 5\%$ during BLX96. It was shown that the effects of cloud shadows on the cloud measurements during BLX96 were likely to be small given the thin clouds and the small solar zenith angles.

To independently calibrate the lateral entrainment and detrainment parameters, data from BOMEX was used in the CuP scheme to show that Siebesma's et al. (2001) values were appropriate. Good agreement was found between the LES and CuP cloud-base heights. The agreement between the LES and CuP predicted maximum cloud-top height was good, but the CuP estimates of intermediate cloud-top heights were sensitive to the entrainment and detrainment rates used in the cloud model.

Using these BOMEX-calibrated entrainment and detrainment values for BLX96, the CuP scheme did a good job predicting observed cloud-base height and the cloud-top height using JFDs based on the mixing-diagram parameterization using (6.4) to find the slope of the surface axis, the observed entrainment zone jumps to find the slope of the entrainment-zone axis, and (6.13a) and (6.13b) to predict the spread along each axis. These CuP predictions were superior to three

alternate cloud-cover parameterizations: a scheme based on relative humidity (Roeckner et al. 1996), the statistical scheme suggested by Sommeria and Deardorff (1977), and a scheme designed for boundary-layer clouds (Albrecht 1981). The agreement between the CuP-predicted cloud cover and the observed cloud cover was not as good as the predictions of cloud heights, but was better than cloud-cover predictions from all other methods tested.

9.2 Future work

9.2.1 JFDs

Based on observations from BLX96, it appears that JFDs of θ vs. r might not follow a joint Gaussian distribution. There has been some discussion in the literature about the nature of distributions of variables in the boundary layer. Lenschow (1970) suggested that observations of θ in the boundary layer are normally distributed, while Manton (1977) suggested that temperature is not normally distributed. Later work (e.g. Lenschow and Stephens 1980; Deardorff and Willis 1985; Cuijpers and Holtslag 1998; Wang and Stevens 2000) supported the contention by Manton (1977) that distributions of variables in the boundary layer are not normally distributed. During BLX96, as well as other field campaigns, JFDs of θ vs. r were skewed. This behavior is caused by the nature of the updrafts and downdrafts. The updrafts tend to be much warmer and moister than the environment, while the downdrafts are only slightly cooler and dryer than the environment. However, physical processes that lead to non-normal values of kurtosis are not as clear.

JFDs measured in the boundary layer can be viewed as a mixing diagram (Chapter 5). The distribution is made of parcels that are mixtures of mixed-layer, surface-layer and entrainment-zone air. The observed mixtures are the sum of many different turbulent mixing events over a range of length and time scales. It is difficult to define a single discrete mixing event in the turbulent boundary layer, but the boundary-layer depth and time scales should be the dominant scales. The observed distribution should approach a Gaussian distribution because it is the sum of many

independent mixing events.

A preliminary numerical exercise was conducted where a simple Monte Carlo experiment was used to test this hypothesis (Figure 9.1A). In this test it was assumed that mixing can be represented by a large number of parcels with a range of θ , and that the system is closed so that no parcels are added or removed. It was also assumed that any parcel has an equal probability of mixing with any other parcel. The parcels are allowed to mix a number of times and the resulting mixtures are placed into bins. Indeed, the distribution of these mixtures was Gaussian, as would be expected by the central limit theorem. After many mixing events, the distribution approached one single value as the model becomes perfectly mixed. A Gaussian distribution did a good job representing the simulated distribution until the distribution became narrower than the prescribed bin size.

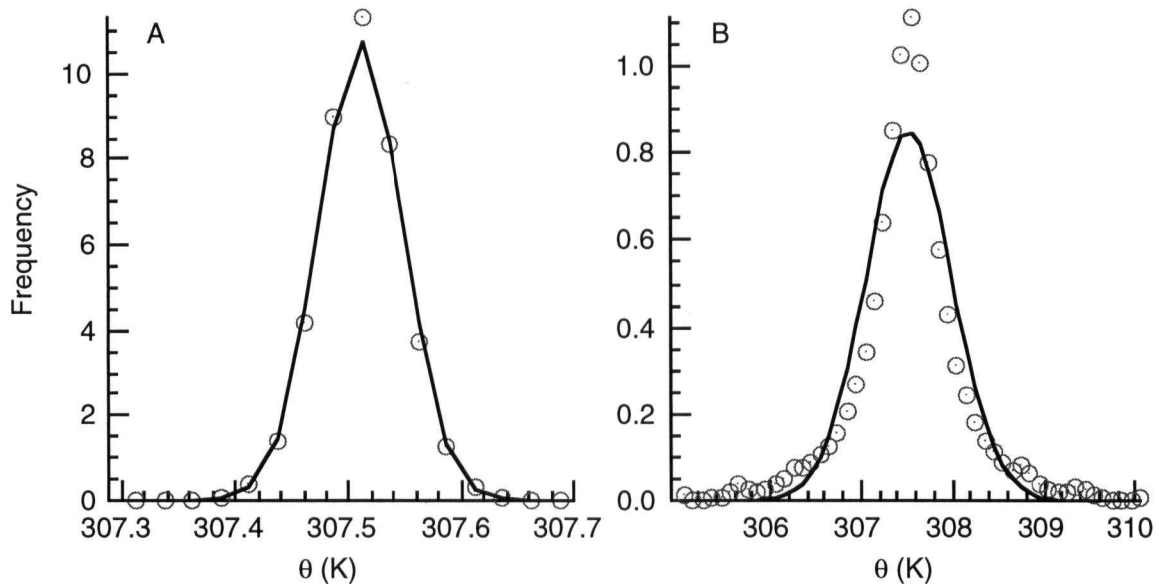


Figure 9.1 Sample θ distributions after mixing (symbols) and Gaussian distributions fit using the mean and variance of θ calculated from the distribution for: (A) no mass added and (B) mass added to the distribution.

However, as shown in Chapter 5, distributions observed during BLX96 may not be Gaussian. A number of physical processes might lead to distributions in the convective boundary layer that are not Gaussian. Unlike the Monte Carlo experiment described above, the convective

boundary layer is not a closed system. Fluxes at the top and bottom of the layer imply that new parcels are added through the top of the layer, and that parcels are modified at the bottom. In addition, the boundary conditions at the Earth's surface and at the top of the mixed layer change as a function of time. Therefore, parcels are not only being added to the system, but the properties of these parcels changes with time. Additional processes that could lead to non-Gaussian distributions are: advection of air with different properties, surface heterogeneity, or mesoscale variability.

The Monte Carlo experiment described above was reconfigured to account for the addition of new parcels by entrainment and the removal of parcels by advection from the layer (Figure 9.1B). After each mixing episode, some mixtures, selected at random, were replaced with parcels that had θ identical to the tails of the distribution (representing parcels rising from the surface and sinking from the entrainment zone). In nature, the number of parcels added or removed would be related to the dynamics of the mixed layer. For the simple test described here, 10% of the parcels were replaced with new parcels. In this case, the tails of the simulated distribution were larger than the tails of a Gaussian distribution (that was fit using the mean and standard deviation of the simulated distribution). The simulated distribution also had a stronger central tendency than the Gaussian distribution, similar to observations made during BLX96. While the initial results were encouraging, more tests are needed.

In addition to the work on the non-Gaussian nature of the JFDs, further tests of the JFD parameterization should be completed for a number of different geographic locations. JFDs measured during BLX96 can also be compared to JFDs produced by LES. This test would provide a check of both the accuracy of LES, and could provide further insight into the shape of the JFDs.

9.2.2 *CuP scheme*

Tests of the ability of the CuP scheme to predict cloud-onset time should also be

conducted. Unfortunately, BLX96 research flights cannot be used because they occurred after clouds had started to form each day. Radiosondes are launched at ARM CART every three hours, but this time resolution is inadequate to determine the cloud-onset time. Other data streams, such as the 915 MHz wind profiler equipped with radio acoustic sounding system (RASS), Raman Lidar, or Atmospheric Emitted Radiance Interferometer (AERI) at the central facility could be used to provide profiles of θ_v , as well as the mean mixed layer value of θ_v and r .

Boundary-layer scales would also be needed to construct parameterized JFDs to test the CuP cloud-onset time. Unfortunately, the similarity relationships determined in Chapter 6 cannot be used because the entrainment-zone fluxes are not known. Simple relationships relating the surface and entrainment-zone fluxes might not be valid when the boundary layer is rapidly changing (Hägeli et al. 2000). In addition, the entrainment-zone moisture flux might not be a constant value of the surface moisture flux. Therefore, new parameterizations for the entrainment zone fluxes are needed or relationships, such as those proposed by Lenschow et al. (1980)

$$\frac{\sigma_\theta^2}{\theta_*} = \frac{\sigma_r^2}{r_*} = 1.8 \left(\frac{z}{z_i} \right)^{-2/3}, \quad (9.1)$$

that do not depend on the entrainment-zone fluxes, could be used to define σ_θ and σ_r .

The CuP parameterization can also be improved, and verification efforts should continue. The CuP scheme should be coupled with a single-column model of the atmosphere. For these tests the CuP scheme would be reconfigured so that it can interact with the environment, perhaps by coupling the CuP parameterization with Transilient Turbulence Theory (Stull 1984). Such tests could be based on BLX96, as well as cases from: BOMEX (Siebesma et al. 2001), continental convection (Brown et al. 2001), the small cumulus mixing experiment, and the trade-wind boundary layer (Stevens et al. 2001). Efforts should be made to more realistically model the cloud lifetime. The CuP scheme could also be coupled with a buoyancy sorting model, rather than the entraining-detraining model used here. These buoyancy sorting models, such as the one proposed by Emanuel (1991), use the cloud-base mass flux to close their parameterization.

References

- Albrecht, B. A., 1979: A model of the thermodynamic structure of trade-wind boundary-layer. Part II: Applications. *J. Atmos. Sci.* **36**, 90-98.
- Albrecht, B., A., 1981: Parameterization of trade-cumulus cloud amounts. *J. Atmos. Sci.*, **38**, 97-105.
- Appleman, H. S., 1962: A comparison of simultaneous aircraft and surface cloud observations. *J. Appl. Meteor.*, **1**, 548-551.
- André, J. -C., J. -P. Goutorbe, and A. Perrin, 1986: HAPEX-MOBILHY, a hydrological atmospheric pilot experiment for the study of water budget and evaporation flux at the climatic scale. *Bull. Am. Meteor. Soc.*, **67**, 138-144.
- Arakawa, A., and W. H. Schubert, 1974: Interaction of cumulus cloud ensemble with the large scale environment, part I. *J. Atmos. Sci.* **31**, 674-701.
- Aviolat, F., T. Cornu, and D. Cattani, 1998: Automatic clouds observation improved by an artificial neural network. *J. Atmos. and Ocean. Tech.*, **15**, 114-126.
- Ball, F. K., 1960: Control of inversion height by surface heating. *Quart. J. Roy. Meteor. Soc.*, **86**, 483-494.
- Bechtold, P., E. Bazile, F. Guichard, P. Mascart, and E. Richard, 2001: A mass-flux convection scheme for regional and global models. *Quart. J. Roy. Meteor. Soc.*, **127**, 869-886.
- Berg, L. K., 1997: A simple scheme to predict boundary-layer cumulus. M.Sc. Thesis. Atmospheric Science Programme, Geography Dept., UBC.
- Berg, L. K., R. B. Stull, E. Santoso, and J. P. Hacker, 1997: Boundary Layer Experiment — 1996, Airborne Scientist Flight Log. Boundary Layer Technical Report 97-1. [Available from Roland Stull, Atmospheric Science Programme, Dept. of Earth and Ocean Sciences, UBC. 6339 Stores Rd. Vancouver, BC V6T-1Z4, Canada].
- Berg, L. K., and R. B. Stull, 2002: Accuracy of point and line measures of boundary layer cloud amount. *J. Appl. Meteor.*, **41**, 640-650.

- Benner, T. C., and J. A. Curry, 1998: Characteristics of small tropical cumulus clouds and their impact on the environment. *J. Geophys. Res.*, **103**, 28753-28767.
- Betts, A. K., 1973: Non-precipitating cumulus convection and its parameterization. *Quart. J. Roy. Meteor. Soc.*, **99**, 178-196.
- Betts, A. K., 1975: Parametric interpretation of trade-wind cumulus budget studies. *J. Atmos. Sci.* **32**, 1934-1945.
- Betts, A. K., 1976: Modeling subcloud layer structure and interaction with a shallow cumulus layer. *J. Atmos. Sci.*, **33**, 2363-2382.
- Betts, A. K., 1982: Saturation point analysis of moist convective overturning. *J. Atmos. Sci.*, **39**, 1484-1505.
- Betts, A. K., 1984: Boundary layer thermodynamics of a high plains severe storm. *Mon. Wea. Rev.*, **112**, 2199-2211.
- Betts, A. K., 1985: Mixing line analysis of clouds and cloudy boundary layers. *J. Atmos. Sci.*, **42**, 2751-2763.
- Betts, A. K., 1986: A new convective adjustment scheme. Part I: Observational and theoretical basis. *Quart. J. Roy. Meteor. Soc.*, **112**, 677-691.
- Betts, A. K., 1992: FIFE atmospheric boundary layer budget methods. *J. Geophys. Res.*, **97**, 18523-18531.
- Betts, A. K., and M. J. Miller, 1986: A new convective adjustment scheme. Part II: Single column tests using GATE wave, BOMEX, ATEX and arctic air-mass data sets. *Quart. J. Roy. Meteor. Soc.*, **112**, 693-709.
- Betts, A. K., and B. A. Albrecht, 1987: Conserved variable analysis of the convective boundary layer thermodynamic structure over tropical oceans. *J. Atmos. Sci.*, **44**, 83-99.
- Bony S., K. A. Emanuel, 2001: A parameterization of the cloudiness associated with cumulus convection; Evaluation using TOGA COARE data. *J. Atmos. Sci.*, **58**, 3158-3183.

- Bretherton, C. S., 1987: A theory for nonprecipitating moist convection between two parallel plates. Part I: Thermodynamics and “linear” solutions. *J. Atmos. Sci.*, **44**, 1809-1827.
- Bretherton, C. S., 1988: A theory for nonprecipitating convection between two parallel plates. Part II: Nonlinear theory and cloud field organization. *J. Atmos. Sci.*, **45**, 2391-2415.
- Bretherton, C. S., 1993: Understanding Albrecht’s model of trade cumulus cloud fields. *J. Atmos. Sci.*, **50**, 2264-2283.
- Bretherton, C. S., E. Klinker, A.K. Betts, J.A. Coakley Jr., 1995: Comparison of ceilometer, satellite, and synoptic measurements of boundary-layer cloudiness and the ECMWF diagnostic cloud parameterization scheme during ASTEX. *J. Atmos. Sci.*, **52**, 2736–2751.
- Brown, A. R., R. T. Cederwall, A. Chlond, P. G. Duynkerke, J.-C. Golaz, M. Khairoutdinov, D. C. Lewellen, A. P. Lock, M. K. MacVean, C.-H. Moeng, R. A. J. Neggers, A. P. Siebesma, B. Stevens., 2002: Large-eddy simulation of the diurnal cycle of shallow cumulus convection over land. *Quart. J. Roy. Meteor. Soc.*(Submitted).
- Businger, J. A., J. C. Wyngaard, Y. Izumi, and E. F. Bradley, 1971: Flux profile relationships in the atmospheric surface layer. *J. Atmos. Sci.*, **28**, 181-189.
- Businger, J. A., and A. M. Yaglom, 1971: Introduction to Obukhov’s paper on ‘Turbulence in an atmosphere with a non-uniform temperature’. *Bound.-Layer Meteor.*, **2**, 3-6.
- Cahalan, R. F., and J. H. Joseph, 1989: Fractal statistics of cloud fields. *Mon. Wea. Rev.*, **117**, 261-272.
- Charney, J. G., R. Fjortoft, and J. von Neuman, 1950: Numerical integration of the barotropic vorticity equation. *Tellus*, **2**, 237-254.
- Coulman, C. E., 1978: Boundary layer evolution and nocturnal inversion dispersal—Part II. *Bound.-Layer Meteor.*, **14**, 493-513.
- Crum, T. D., and R. B. Stull, 1987: Field measurements of the amount of surface layer air versus height in the entrainment zone. *J. Atmos. Sci.*, **44**, 2743-2753.

- Cuijpers, J. W. M., and A. A. M. Holtslag, 1998: Impact of skewness and nonlocal effects on scalar and buoyancy fluxes in convective boundary layers. *J. Atmos. Sci.*, **55**, 151-162.
- Culf, A., 1994: Equilibrium evaporation beneath a growing convective boundary layer. *Bound. -Layer Meteor.*, **70**, 37-49.
- Deardorff, J. W., 1970a: Preliminary results from numerical integration of the unstable planetary boundary layer. *J. Atmos. Sci.*, **27**, 1209-1211.
- Deardorff, J. W., 1970b: Convective velocity and temperature scales for the unstable planetary boundary layer and Rayleigh convection. *J. Atmos. Sci.*, **27**, 1211-1212.
- Deardorff, J. W., 1972: Numerical investigation of neutral and unstable planetary boundary layers. *J. Atmos. Sci.*, **30**, 1070-1076.
- Deardorff, J. W., 1974: Three-dimensional numerical study of turbulence. *Bound. -Layer Meteor.*, **7**, 199-226.
- Deardorff, J. W., and Willis, G. E., 1985: Further results from a laboratory model of the convective planetary boundary layer. *Bound. -Layer Meteor.*, **32**, 205-236.
- Delnore, V. E., 1972: The diurnal variation of the temperature structure and some aspects of heat transfer at the BOMEX fixed stations. *J. Phys. Ocean.*, **3**, 239-247.
- Dyer, A. J., 1974: A review of flux-profile relations. *Bound.-Layer Meteor.*, **1**, 363-372.
- Ek, M., and L. Mahrt, 1991: A formulation for boundary-layer cloud cover. *Ann. Geophysicae*, **9**, 716-724.
- Ellingson, R. G., 1982: On the effects of cumulus dimensions on longwave irradiance and heating rate calculations. *J. Atmos. Sci.*, **39**, 886-896.
- Emanuel, K. A., 1991: A scheme for representing cumulus convection in large-scale models. *J. Atmos. Sci.*, **48**, 2313-2335.
- Etling D., and Brown, R. A., 1993: Roll vortices in the planetary boundary-layer - a review. *B.-Layer Meteor.*, **65**, 215-248.

- Fairall, C. W., A. B. White, J. B. Edson, J. E. Hare, 1997: Integrated shipboard measurements of the marine boundary layer. *J. Atmos. and Ocean. Tech.*, **14**, 338-359.
- Fedorovich, E., R. Kaiser, M. Rau., and E. Plate, 1996: Wind tunnel study of turbulent flow structure in the convective boundary layer capped by a temperature inversion. *J. Atmos. Sci*, **53**, 1273-1289.
- Feijt, A., and A. van Lammeren, 1996: Ground-based and satellite observations of cloud fields in the Netherlands. *Mon. Wea. Rev.*, **124**, 1914-1923.
- Frisch, A. S., and J. A. Businger, 1973: A study on the convective elements in the atmospheric surface layer. *Bound.-Layer Meteor.*, **3**, 301-328.
- Meteor., 3, 301-328Fulton, R. A., J. P. Breidenbach, D.-J. Seo, D. A. Miller, T. O'Bannon, 1998: The WSR-88D rainfall algorithm. *Wea. Forecasting*, **13**, 377-395.
- Grant, A. L. M., and A. R. Brown, 1999: A similarity hypothesis for shallow-cumulus transports. *Quart. J. Roy. Meteor. Soc.*, **125**, 1913-1936.
- Greenhut, G. K. and S. J. S. Khalsa, 1982: Updraft and downdraft events in the atmospheric boundary layer over the equatorial Pacific Ocean. *J. Atmos. Sci*, **39**, 1803-1818.
- Greenhut, G. K. and S. J. S. Khalsa, 1987: Convective elements in the marine atmospheric boundary layer. Part I: Conditional sampling statistics. *J. Climate Appl. Meteor.*, **26**, 813-822.
- Gregory, D. 2001: Estimation of entrainment rate in simple models of convective clouds. *Quart. J. Roy. Meteor. Soc.* **127**, 53-72.
- Grell, G. A., 1993: Prognostic evaluation of assumptions used by cumulus parameterizations. *Mon. Wea. Rev.*, **121**, 764-787.
- Grell, G. A., Y.-H. Kuo, and R. J. Pasch, 1991: Semiprognostic tests of cumulus parameterization schemes in the middle latitudes. *Mon. Wea. Rev.*, **119**, 5-31.
- Grimsdell, A. W., and W. M. Angevine, 1998: Convective boundary layer height measurement with wind profilers and comparison to cloud base. *J. Atmos. and Ocean. Tech.*, **15**,

1331-1338.

- Grossman, R. L., 1984: Bivariate conditional sampling of moisture flux over a tropical ocean. *J. Atmos. Sci.*, **41**, 3238-3252.
- Guillemet, B., H. Isaka, and P. Mascart, 1983: Molecular dissipation of turbulent fluctuations in the convective mixed layer. Part I: Height variations of dissipation rates. *Bound. -Layer Meteor.*, **27**, 141-162.
- Hägeli, P., D. G. Steyn, and B. Strawbridge, 2000: Spatial and temporal variability of mixed-layer depth and entrainment zone thickness. *Bound. -Layer Meteor.*, **97**, 47-71.
- Haiden, T., 1996: Generalization of Albrecht's cumulus cloud amount parameterization. *J. Atmos. Sci.*, **53**, 3164-3167.
- Haiden, T., 1997: An analytical study of cumulus onset. *Quart. J. Roy. Meteor. Soc.*, **123**, 1945-1960.
- Hanson, H. P., 1984: On mixed layer modeling of the stratocumulus-topped marine boundary layer. *J. Atmos. Sci.*, **41**, 1226-1234.
- Henderson-Sellers, A., and K. McGuffie, 1990: Are cloud amounts estimated from satellite sensor and conventional surface-based observations related? *Int. J. Remote Sensing*, **11**, 543-550.
- Hibberd, M. F., and B. L. Sawford, 1994: A saline laboratory model of the planetary convective boundary layer. *Bound. -Layer Meteor.*, **67**, 229-250.
- Holland, J. Z., and E. M. Rasmusson, 1973: Measurements of atmospheric mass, energy and momentum budgets over a 500-kilometer square of tropical ocean. *Mon. Wea. Rev.*, **101**, 44-55.
- Holland, J. Z., 1973: A statistical method for analyzing wave shapes and phase relationships of fluctuating geophysical variables. *J. Phys. Oceanography*, **3**, 139-155.
- Hoyt, D. V., 1977: Percent of possible sunshine and the total cloud cover. *Mon. Wea. Rev.*, **105**, 648-652.

- Hozumi, K., T. Harimaya, and C. Magono, 1982: The size distribution of cumulus clouds as a function of cloud amount. *J. Meteor. Soc. Japan*, **60**, 691-699
- Hu, Q., 1997: A cumulus parameterization based on a cloud model of intermittently rising thermals. *J. Atmos. Sci.*, **45**, 2292-2307.
- Joseph, J. and R. F. Cahalan, 1990: Nearest neighbor spacing of fair weather cumulus clouds. *J. Appl. Meteor.*, **29**, 793-805.
- Kaimal, J. C., J. C. Wyngaard, D. A. Haugen, O. R. Cote, Y. Izumi, S. J. Caughey and J. C. Readings, 1976: Turbulence structure in the convective boundary layer. *J. Atmos. Sci.*, **33**, 2152-2169.
- Kain, J. S., and J. M. Fritsch, 1990: A one-dimensional entraining/detraining plume model and its application in convective parameterization. *J. Atmos. Sci.*, **47**, 2784-2802.
- Khalsa, S. J. S., and G. K. Greenhut, 1985: Conditional sampling of updrafts and downdrafts in the marine atmospheric boundary layer. *J. Atmos. Sci.*, **42**, 2550-2562.
- Kuo, H.-L., 1965: On formation and intensification of tropical cyclones through latent release by cumulus convection. *J. Atmos. Sci.*, **22**, 40-63.
- Kuo, H.-L., 1974: Further studies of the parameterization of the influence of cumulus convection on large-scale flow. *J. Atmos. Sci.*, **31**, 1232-1240.
- Kuo, K. -S., R. M. Welch, R. C. Weger, M. A. Engelstad, and S. K. Sengupta, 1993: The three-dimensional structure of cumulus cloud over the ocean, I: Structural analysis. *J. Geophys. Res.*, **98**, 20685-20711.
- Lappen, C.-L., and D. A. Randall, 2001: Toward a unified parameterization of the boundary layer and moist convection. Part I: A new type of mass-flux model. *J. Atmos. Sci.*, **58**, 2021-2036.
- Lazarus, S. M., S. K. Krueger, G. G. Mace, 2000: A Cloud Climatology of the Southern Great Plains ARM CART. *J. of Climate*. **13**, 1762-1775.
- Lenschow, D. H., 1970: Airplane measurements of the planetary boundary layer structure. *J.*

- Appl. Meteor.*, **9**, 874-884.
- Lenschow, D. H., and P. L. Stephens, 1980: The role of thermals in the convective boundary layer. *Bound.-Layer Meteor.*, **19**, 509-532.
- Lenschow, D. H., J. C. Wyngaard, and W. T. Pennell, 1980: Mean-field and second-moment budgets in a baroclinic, convective boundary layer. *J. Atmos. Sci.*, **37**, 1313-1326.
- Lenschow, D. H., J. Mann, and L. Kristensen, 1994: How long is long enough when measuring fluxes and other turbulence statistics? *J. Atmos. and Ocean. Tech.*, **11**, 661-673.
- Lopez, R. E., 1977: The lognormal distribution of cumulus cloud populations. *Mon. Wea. Rev.*, **105**, 865-872.
- Mahrt, L., and J. Paumier, 1982: Cloud-top entrainment instability observed in AMTEX. *J. Atmos. Sci.*, **39**, 622-634.
- Mahrt, L., and J. Paumier, 1984: Heat transport in the atmospheric boundary layer. *J. Atmos. Sci.*, **41**, 3061-3075.
- Malick, J. D., J. H. Allen, and S. Zakanycz, 1979: Calibrated analytical modeling of cloud-free intervals. *Proceedings of the Society of Photo-Optical Instrumentation Engineers*, **195**, 142-147.
- Malkus, J. S., 1954: Some results of a trade-cumulus cloud investigation. *J. Meteor.*, **11**, 220-237.
- Malkus, J. S., 1958: On the structure of the trade wind moist layer. *Papers in Physical Oceanography and Meteorology. Massachusetts Institute of Technology and Woods Hole Oceanographic Institution*. **13**, No 2.
- Manabe, S., J. Smagorinsky, and R. F. Strickler, 1965: Simulated climatology of a general circulation model with a hydrologic cycle. *Mon. Wea. Rev.*, **93**, 769-798.
- Manton, J. R., 1975: Penetrative convection due to a field of thermals. *J. Atmos. Sci.*, **32**, 2272-2277.
- Manton, M. J., 1977: On the structure of convection. *Bound.-Layer Meteor.*, **12**, 491-503.
- Mellor, G. L., 1977: The gaussian cloud model relations. *J. Atmos. Sci.*, **34**, 356-358

- Ming, Z., and P. H. Austin, 2002: Episodic mixing and buoyancy-sorting representations of shallow convection: A diagnostic study. *Submitted to J. Atmos. Sci.*
- Moeng, C.-H., and J. C. Wyngaard, 1984: Statistics of conservative scalars in the convective boundary layer. *J. Atmos. Sci.*, **41**, 3161-3169.
- Monin, A. S., and A. M. Obukhov, 1954: Basic laws of turbulent mixing in the atmosphere near the ground. *Tr. Akad. Nauk., SSSR Geophys. Inst, No. 24 (151), 1963-1987*
- National Oceanic and Atmospheric Administration, Federal Aviation Administration, U.S. Navy, and U.S. Dept. of the Air Force, 1998: *ASOS user's guide*. 70 pp. [Available online from [http://www.nws.noaa.gov/asos/.](http://www.nws.noaa.gov/asos/)]
- Neggers, R. A. J., H. J. J. Jonker, and A. P. Siebesma, 2001: Size statistics of cumulus cloud populations in large-eddy simulations. *Submitted to J. Atmos. Sci.*
- Neggers, R. A. J., A. P. Siebesma, and H. J. J. Jonker, 2002: A multiparcel model for shallow cumulus convection. *J. Atmos. Sci.*, **59**, 1655-1668.
- Nicholls, S. and M. A. LeMone, 1980: The fair weather boundary layer in GATE: The relationship of subcloud fluxes and structure to the distribution and enhancement of cumulus clouds. *J. Atmos. Sci.*, **37**, 2051-2067.
- Nitta, T., 1975: Observational determination of cloud mass flux distributions. *J. Atmos. Sci.*, **32**, 73-91.
- Obukhov, A. M., 1971: Turbulence in an atmosphere with a non-uniform temperature. *Bound.-Layer Meteor.*, **2**, 7-29.
- Paluch, I. R., 1979: Entrainment mechanism in Colorado cumuli. *J. Atmos. Sci.*, **36**, 2467-2478.
- Pennell, W. T., and M. A. LeMone, 1974: An experimental study of turbulence structure in the fair-weather trade wind boundary layer. *J. Atmos. Sci.*, **31**, 1308-1323.
- Plank, V. G., 1969: The size distribution of cumulus clouds in representative Florida populations. *J. Appl. Meteor.*, **8**, 46-67.

- Poellot, M. R., and S. K. Cox, 1977: Computer simulation of irradiance measurements from aircraft. *J. Appl. Meteor.*, **16**, 167-171.
- Press, W. H., S. A. Teukolsky, W. T. Vetterling, and B. P. Flannery, 1992: *Numerical Recipes in C: The Art of Scientific Computing*. Cambridge University Press. 994 pp.
- Rabin, R. M., S. Stadler, P. J. Wetzell, D. J. Stensrud, M. Gregory, 1990: Observed effects of landscape variability on convective clouds. *Bull. Amer. Meteor. Soc.*, **71**, 272-280.
- Ramirez, J. A., and R. L. Bras, 1990: Clustered or regular cumulus cloud fields: The statistical character of observed and simulated cloud fields. *J. Geophys. Res.*, **95**, 2035-2045.
- Randall, D. A., G. J. Huffman, 1980: A stochastic model of cumulus clumping. *J. Atmos. Sci.*, **37**, 2068-2078.
- Randall, D. A., Q. Shao, C.-H. Moeng, 1992: A second-order bulk boundary-layer model. *J. Atmos. Sci.*, **49**, 1903-1923.
- Raymond, D. J., and A. M. Blyth, 1986: A stochastic mixing model for nonprecipitating cumulus clouds. *J. Atmos. Sci.*, **43**, 2708-2718.
- Roeckner, E., L. Bengtsson, M. Christoph, M. Claussen, L. Dumenil, M. Esch, M. Giorgetta, U. Schlese, and U. Schulzweida, 1996: The atmospheric general circulation model echam-4: Model description and simulation of present-day climate. Technical Report 218, Max-Planck-Institut für Meteorologie.
- Richardson, R. F., 1922: *Weather Prediction by Numerical Process*. Cambridge University Press, reprinted by Dover, 1965, 236 pp.
- Santoso, E., and R. B. Stull, 1998: Wind and temperature profiles in the radix layer, the bottom fifth of the convective boundary layer. *J. Appl. Meteor.*, **37**, 545-558.
- Santoso, E., and R. B. Stull, 1999: Use of synthetic data to test flight patterns for a boundary-layer field experiment. *J. Atmos. and Ocean Tech.* **16**, 1157-1171.
- Santoso, E., R. Stull, 2001: Similarity equations for wind and temperature profiles in the radix layer, at the bottom of the convective boundary layer. *J. Atmos. Sci.*, **58**, 1446-1464.

- Sengupta, S. K., R. M. Welch, M. S. Navar, T. A. Berendes, and D. W. Chen, 1990: Cumulus cloud field morphology and spatial patterns derived from high spatial resolution Landsat imagery. *J. Appl. Meteor.*, **29**, 1245-1266.
- Schneider, E. K., and R. S. Lindzen, 1976: A discussion of the parameterization of momentum exchange by cumulus convection. *J. Geophys. Res.*, **81**, 3158-3160.
- Schrieber, K, R. Stull, and Q. Zhang, 1996: Distributions of surface-layer buoyancy versus lifting condensation level over a heterogeneous land surface. *J. Atmos. Sci.*, **53**, 1086-1107.
- Schumann, U., and C.-H. Moeng, 1991: Plume fluxes in the clear and cloudy convective boundary layers. *J. Atmos. Sci.*, **48**, 1746-1757.
- Siebesma, A. P., and J. W. M. Cuijpers, 1995: Evaluation of parametric assumptions for shallow cumulus convection. *J. Atmos. Sci.*, **52**, 650-666.
- Siebesma, A. P., and A. A. M. Holtslag, 1996: Model impacts of entrainment and detrainment rates in shallow cumulus convection. *J. Atmos. Sci.*, **53**, 2354-2364.
- Siebesma, A. P., C. S. Bretherton, A. Brown, A. Chlond, J. Cuxart, P. G. Duynkerke, H. Jiang, M. Khairoutdinov, D. Lewellen, C.-H. Moeng, E. Sanchez, B. Stevens, and D. E. Stevens, 2001: A large-eddy simulation intercomparison study of shallow cumulus convection. *Quart. J. Roy. Meteor. Soc.* (submitted)
- Slingo, J. M., 1987: The development and verification of a cloud prediction scheme for the ECMWF model. *Quart. J. Roy. Meteor. Soc.*, **113**, 899-927.
- Sommeria, G., and J. W. Deardorff, 1977: Subgrid-scale condensation in models of non-precipitating clouds. *J. Atmos. Sci.*, **34**, 344-355.
- Sorbjan, Z., 1986: On similarity in the atmospheric boundary layer. *Bound.-Layer Meteor.*, **34**, 377-397.
- Sorbjan, Z., 1990: Similarity scales and universal profiles of statistical moments in the convective boundary layer. *J. Appl. Meteor.*, **29**, 762-775.

- Sorbjan, Z., 1991: Evaluation of local similarity function in the convective boundary layer. *J. Appl. Meteor.*, **31**, 1565-1583.
- Sorbjan, Z., 1999: Similarity of scalar fields in the convective boundary layer. *J. Atmos. Sci.*, **56**, 2212-2221.
- Simpson, J., 1971: On cumulus entrainment and one-dimensional models. *J. Atmos. Sci.*, **28**, 449-455.
- Simpson, J., and V. Wiggert, 1969: Models of precipitating cumulus towers. *Mon. Wea. Rev.*, **97**, 471-489.
- Smith, R. N. B., 1990: A scheme for predicting layer clouds and their water content in a GCM. *Quart. J. Roy. Meteor. Soc.*, **116**, 435-460.
- Stevens, B., A. S. Ackerman, B. C. Albrecht, A. R. Brown, A. Chlond, J. Cuxart, P. G. Duynkerke, D. C. Lewellen, M. K. MacVean, E. Sanchez, A. P. Siebesma, and D. E. Stevens, 2001: Simulations of trade-wind cumuli under a strong inversion. *J. Atmos. Sci.*, **58**, 1870-1891.
- Stokes, G. M., and S. E. Schwartz, 1994: The Atmospheric Radiation Measurement (ARM) Program: Programmatic background and design of the cloud and radiation testbed. *Bull. Amer. Meteor. Soc.*, **75**, 1201-1221.
- Stommel, H., 1947: Entrainment of air into a cumulus cloud. *J. Meteor.*, **4**, 91-94.
- Stull, R. B., 1984: Transient Turbulence Theory. Part I: Concept of eddy mixing across finite differences. *J. Atmos. Sci.*, **41**, 50-57.
- Stull, R. B., 1988: *An Introduction to Boundary-Layer Meteorology*. Kluwer Academic Publishers. 666 pp.
- Stull, R. B., 1990: *Similarity Relationship Handbook*. Tech Note Number BLRT-90-1. [Available from Prof. R. Stull, Atmospheric Science Programme, Department of Earth and Ocean Sciences, The University of British Columbia, 6339 Stores Rd. Vancouver, BC, V6T 1Z2, Canada].

- Stull, R. B., 1994: A convective transport theory for surface fluxes. *J. Atmos. Sci.*, **51**, 3-22
- Stull, R. B., and E. Eloranta 1985: A case study of the accuracy of routine, fair-weather cloud-base reports. *National Weather Digest*, **10**, 19-24.
- Stull, R., E. Santoso, L. Berg, J. Hacker, 1997: Boundary Layer Experiment 1996 (BLX96). *Bull. Amer. Meteor. Soc.*, **78**, 1149-1158.
- Sundqvist, H., 1978: A parameterization scheme for non-convective condensation including prediction of cloud water content. *Quart. J. Roy. Meteor. Soc.*, **104**, 677-690.
- Tiedtke, M., 1989: A comprehensive mass flux scheme for cumulus parameterization in large-scale models. *Mon. Wea. Rev.*, **117**, 1779-1799.
- von Salzen, K. and N. A. McFarlane, 2002: Parameterization of bulk effects of lateral and cloud-top entrainment in transient shallow cumulus clouds. *J. Atmos. Sci.*, **59**, 1405-1430.
- Wang, S., and B. A. Albrecht, 1986: Stratocumulus model with an internal circulation. *J. Atmos. Sci.*, **43**, 2374-2391.
- Wang, S., and B. A. Albrecht, 1990: A mean gradient of the convective boundary layer. *J. Atmos. Sci.*, **47**, 126-138.
- Wang, S., and B. Stevens, 2000: Top-hat representation of turbulence statistics in cloud-topped boundary layers: A large eddy simulation study. *J. Atmos. Sci.*, **57**, 423-441.
- Warner, J., 1970: On steady-state one-dimensional models of cumulus convection. *Atmos. Sci.*, **27**, 1035-1040.
- Weckwerth, T. M., J. W. Wilson, R. M. Wakimoto, and N. Andrew Crook, 1997: Horizontal convective rolls: Determining the environmental conditions supporting their existence and characteristics. *Mon. Wea. Rev.*, **125**, 505-526.
- Weger, R. C., J. Lee, T. Zhu, and R. M. Welch, 1992: Clustering, randomness and regularity in cloud fields: 1. Theoretical considerations. *J. Geophys. Res.*, **97**, 20,519-20,536.

- Weil, J. C., and T. W. Horst, 1992: Footprint estimates for the atmospheric flux measurements in the convective boundary layer. *Precipitation Scavenging and Atmospheric-Surface Exchange*. Vol 2. E. Schwartz and W. G. N. Slinn Eds. Hemispheric Publishing. 717-728.
- Wetzel, P. J., 1990: A simple parcel method for prediction of cumulus onset and area-averaged cloud amount over heterogeneous land surfaces. *J. Appl. Meteor.*, **29**, 516-523.
- White, A. B., C. W. Fairall and J. B. Snider, 1995: Surface-based remote sensing of marine boundary-layer cloud properties. *J. Atmos. Sci.*, **52**, 2827-2838.
- Wielicki, B. A., and R. M. Welch, 1986: Cumulus cloud properties derived using landsat satellite data. *J. Clim. and Appl. Meteor.*, **25**, 261-276.
- Wilde, N. P., R. B. Stull, and W. Eloranta, 1985: The LCL zone and cumulus onset. *J. Clim. Appl. Meteor.*, **24**, 640-657.
- Williams, A. G., and J. M. Hacker, 1992: The composite shape and structure of coherent eddies in the convective mixed layer. *Bound.-Layer Meteor.*, **61**, 213-245.
- Willis, G. E., and J. W. Deardorff, 1974: A laboratory model of the unstable planetary boundary layer. *J. Atmos. Sci.*, **31**, 1297-1307.
- Wyngaard, J. C., 1973: On surface-layer turbulence, in D. A. Haugen (ed.), Workshop on Micrometeorology. AMS, Boston, Mass.
- Wyngaard, J. C., O. R. Cote, and Y. Izumi, 1971: Local free convection, similarity, and the budgets of shear stress and heat flux. *J. Atmos. Sci.*, **28**, 1171-1182.
- Wyngaard, W. T. Pennell, D. H. Lenschow, and M. A. LeMone, 1978: The temperature-humidity covariance budget in the convective boundary layer. *J. Atmos. Sci.*, **35**, 47-58.
- Wyngaard, J. C., and R. A. Brost, 1984: Top-down and bottom-up diffusion of a scalar in the convective boundary layer. *J. Atmos. Sci.*, **41**, 102-112.
- Wyngaard, J. C., and C.-H. Moeng, 1992: Parameterizing turbulent diffusion through the joint probability density. *Bound.-Layer Meteor.*, **60**, 1-13.

- Xu, K.-M., and S. K. Krueger, 1991: Evaluation of cloudiness parameterizations using a cumulus ensemble model. *Mon. Wea. Rev.*, **119**, 342-367.
- Xu, K.-M., and D. A. Randall, 1996: Evaluation of statistically based cloudiness parameterizations used in climate models. *J. Atmos. Sci.*, **53**, 3103-3119.
- Young, G. S., 1988: Turbulence structure of the convective boundary layer. Part II: Phoenix 78 aircraft observations of thermals and their environment. *J. Atmos. Sci.*, **45**, 727-735.
- Young, M. J., 1967: Variability in estimating total cloud cover from satellite pictures. *J. Appl. Meteor.*, **6**, 573-579.
- Zhu, T., J. Lee, R. C. Weger, and R. M. Welch, 1992: Clustering, randomness, and regularity in cloud fields: 2. Cumulus cloud fields. *J. Geophys. Res.*, **97**, 20,537-20,558.
- Zilitinkevich, S., 1994: A generalized scaling for convective shear flows. *Bound.-Layer Meteor.*, **70**, 51-78.
- Zuev, V. E., R. B. Zhuravleva, and G. A. Titov, 1987: Modeling of outgoing longwave radiation in the presence of broken clouds. *J. Geophys. Res.*, **92**, 5533-5539.

Appendix A: General Statistics for BLX96

Table A1. Observed date, time, z_i , $\overline{w\theta}$ and \overline{wr} for all BLX96 case study days.

Date	Leg	Time (LST)	Time (UTC)	z (m)	z_i (m)	$\overline{w\theta}$ (K m s ⁻¹)	\overline{wr} (g kg ⁻¹ m s ⁻¹)
15-Jul	1	10.2	16.2	70	1090	0.0767	0.0126
	2	11.4	17.4	930	1510	-0.00209	0.294
	3	11.6	17.6	460	1590	0.103	0.154
	4	11.9	17.9	60	1670	0.103	0.0503
	5	13.2	19.2	690	2080	0.0509	0.146
	6	13.4	19.4	200	2160	0.093	0.119
	7	13.7	19.7	60	2230	0.0868	0.0349
16-Jul	1	10.8	16.8	50	910	0.0427	0.0136
	2	11.9	17.9	850	1140	-0.00877	0.145
	3	12.2	18.2	360	1190	0.0406	0.124
	4	12.4	18.4	40	1290	0.0513	0.0179
	5	13.7	19.7	510	1440	0.0412	0.161
	6	13.9	19.9	250	1480	0.0253	0.104
	7	14.1	20.1	50	1510	0.0369	-0.00538
22-Jul	1	11.2	17.2	60	1110	0.142	0.0641
	2	12.1	18.1	940	1170	0.00714	0.104
	3	12.4	18.4	460	1210	0.0926	0.0663
	4	12.7	18.7	60	1260	0.152	0.0384
	5	13.9	19.9	680	1560	0.0607	0.0813
	6	14.1	20.1	190	1650	0.137	0.0746
	7	14.4	20.4	60	1750	0.164	0.0467

Table A1 continued.

Date	Leg	Time (LST)	Time (UTC)	z (m)	z_i (m)	$\overline{w\theta}$ (K m s ⁻¹)	\overline{wr} (g kg ⁻¹ m s ⁻¹)
23-Jul	1	11.8	17.8	40	950	0.0864	0.0732
	2	12.9	18.9	40	1060	0.0905	0.0681
	3	14.1	20.1	560	1290	0.0381	0.12
	4	14.3	20.3	230	1350	0.073	0.0808
	5	14.6	20.6	40	1430	0.0689	0.0563
25-Jul	1	11.1	17.1	60	1360	0.11	0.0607
	2	12.3	18.3	920	1970	0.0452	0.121
	3	12.6	18.6	470	2070	0.0996	0.0673
	4	12.8	18.8	60	2170	0.129	0.0651
	5	14.1	20.1	690	2450	0.0898	0.0556
	6	14.3	20.3	210	2480	0.093	0.063
	7	14.6	20.6	60	2490	0.0818	0.0427
27-Jul	1	11.0	17.0	30	530	0.0519	0.0491
	2	12.2	18.2	470	750	0.00334	0.0794
	3	12.5	18.5	230	800	0.036	0.0929
	4	12.7	18.7	30	850	0.0617	0.0795
	5	13.9	19.9	470	1050	0.0127	0.138
	6	14.2	20.2	220	1090	0.0493	0.153
	7	14.5	20.5	30	1130	0.0442	0.0805

Table A1. continued.

Date	Leg	Time (LST)	Time (UTC)	z (m)	z_i (m)	$\overline{w\theta}$ (K m s ⁻¹)	\overline{wr} (g kg ⁻¹ m s ⁻¹)
28-Jul	1	11.3	17.3	70	460	0.0367	0.0736
	2	12.5	18.5	830	1360	-0.0112	0.182
	3	12.8	18.8	440	1500	0.0178	0.139
	4	13.1	19.1	60	1610	0.0355	0.105
	5	14.3	20.3	610	1800	0.0247	0.162
	6	14.6	20.6	190	1780	0.0334	0.129
	7	14.9	20.9	70	1730	0.0263	0.086
31-Jul	1	11.2	17.2	70	1440	0.114	0.0417
	2	12.4	18.4	940	1570	0.0403	0.048
	3	12.7	18.7	480	1630	0.0755	0.0531
	4	13.0	19.0	70	1700	0.137	0.0544
	5	14.2	20.2	700	2100	0.0577	0.0287
	6	14.5	20.5	200	2230	0.12	0.0549
	7	14.7	20.7	70	2370	0.101	0.0535
2-Aug	1	11.0	17.0	60	690	0.042	0.0688
	2	12.2	18.2	760	940	-0.023735	0.119
	3	12.5	18.5	520	980	0.00915	0.142
	4	12.7	18.7	60	1020	0.0379	0.0944
	5	14.0	20.0	750	1110	0.00366	0.0597
	6	14.2	20.2	260	1120	0.0152	0.082
	7	14.5	20.5	70	1120	0.0343	0.0785

Table A1 continued.

Date	Leg	Time (LST)	Time (UTC)	z (m)	z_i (m)	$\overline{w\theta}$ (K m s ⁻¹)	\overline{wr} (g kg ⁻¹ m s ⁻¹)
13-Aug	1	11.1	17.1	30	1030	0.0488	0.0351
	2	11.8	17.8	130	1150	0.0515	0.0587
	3	12.1	18.1	220	1200	0.0549	0.0596
	4	12.3	18.3	480	1230	0.0379	0.0614
	5	12.6	18.6	700	1260	0.0373	0.0896
	6	12.9	18.9	50	1290	0.0601	0.0386
	7	14.7	20.7	40	1310	0.0623	0.0454

Appendix B: BLX96 Sample Data

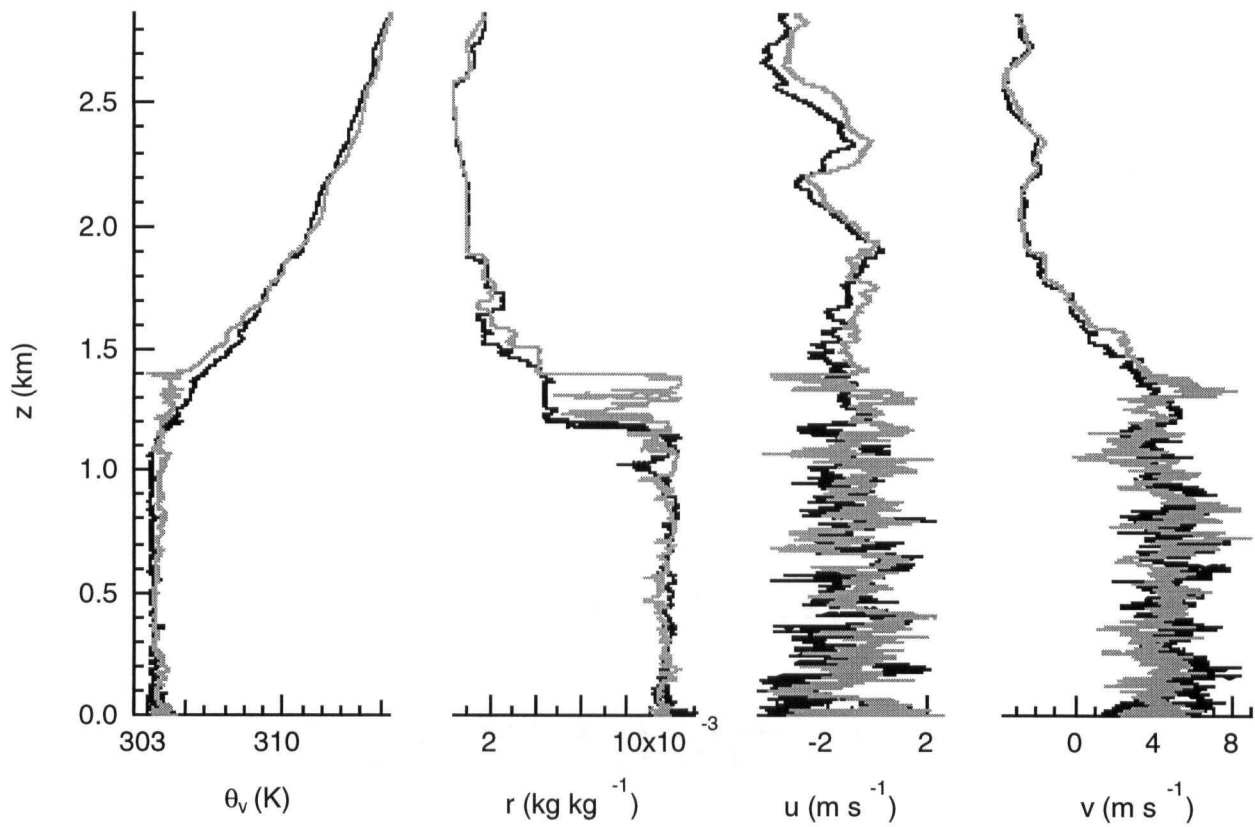


Figure B.1. Plot of θ_v , r , u and v vs. height for the second set of slant soundings (13:15 LST) on 13 August 1996.

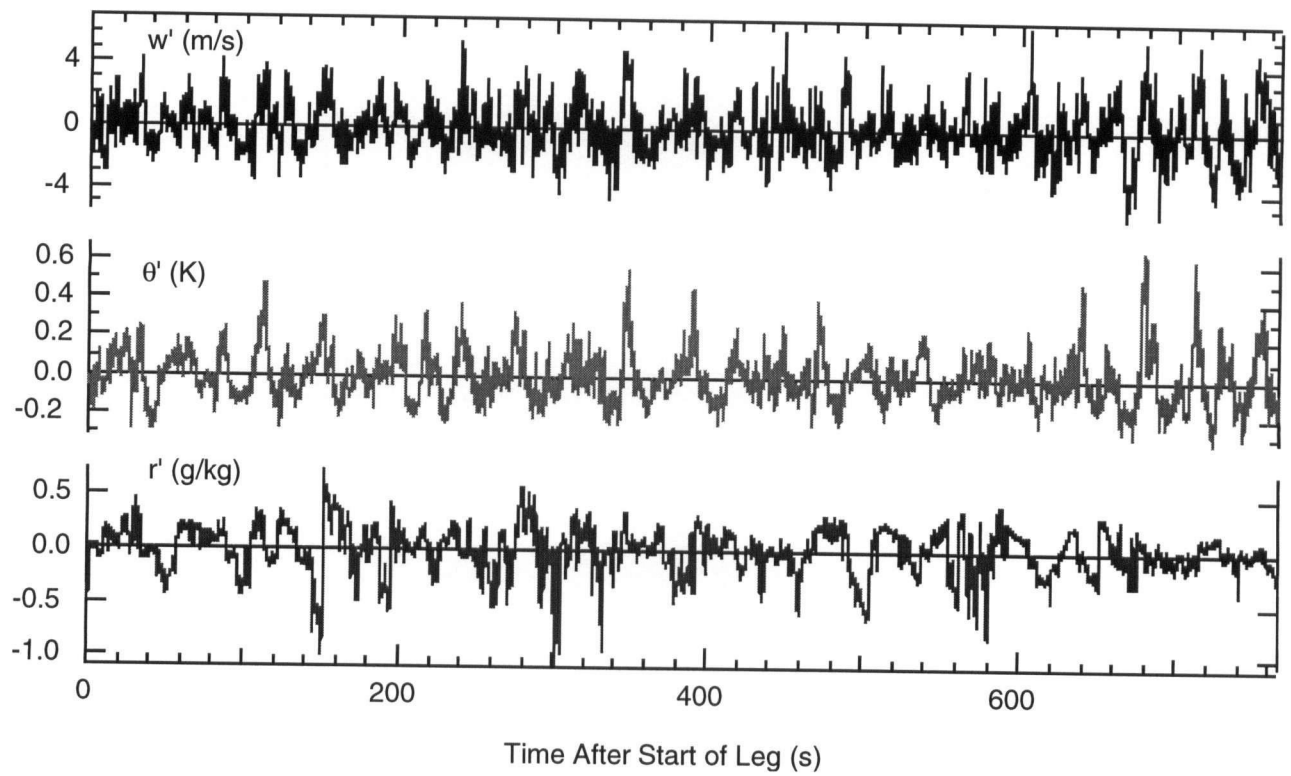


Figure B.2. Plot of (top) w' , (middle) θ' , and (bottom) r' vs. time after start of the leg for a mid-level leg ($0.2 z_i$) on 25 July.

Appendix C: Slopes used in the B - θ_F method

Schrieber et al. (1996) derived equations for θ' and r' , the perturbation values from the means, as [their (4) and (5)]:

$$\theta' = \frac{B\theta_F}{1+B}, \text{ and} \quad (C1)$$

$$r' = \frac{\gamma\theta_F}{1+B}, \quad (C2)$$

where γ is the psychrometric constant and θ_F is the solar forcing (defined in Chapter 5). They modified these equations to give slopes in terms of θ_v and z_{LCL} . However, (C1) and (C2) can be combined to give the slopes in terms of θ and r . Like the work of Schrieber et al., lines of constant B can be found by dividing (C2) by (C1)

$$r'/\theta' = \gamma/B. \quad (C3)$$

Lines of constant solar forcing can also be found from (C1) and (C2). First, (C2) is solved in terms of B . This value is substituted into (C1) leaving

$$r' = -\gamma\theta' + \gamma\theta_F, \quad (C4)$$

which is the equation for the θ_F lines. In θ vs. r space all lines of constant solar forcing have the same slope, $-\gamma$. This result is different than lines of constant solar forcing in θ_v vs. z_{LCL} space, which are a function of the reference state. Figure C.1 shows an example of (C3) and (C4) plotted in θ vs. r space. Figure C.1 appears to be a mirror image of Schrieber et al.'s Figure 2 because large values of z_{LCL} correspond to small values of r .

The slope of the maximum-likelihood best-fit B and θ_F axes had the same sign for all BLX96 flight legs. Inspection of Schrieber et al.'s results from HAPEX showed that they too, found both slopes had the same sign. A priori, we would not expect this to be the case, we would expect that the slopes of the B (γ_B) and θ_F (γ_{θ_F}) axes to be independent. Figure C.1 indicates that for all positive values of B and θ_F , the slopes should have different signs.

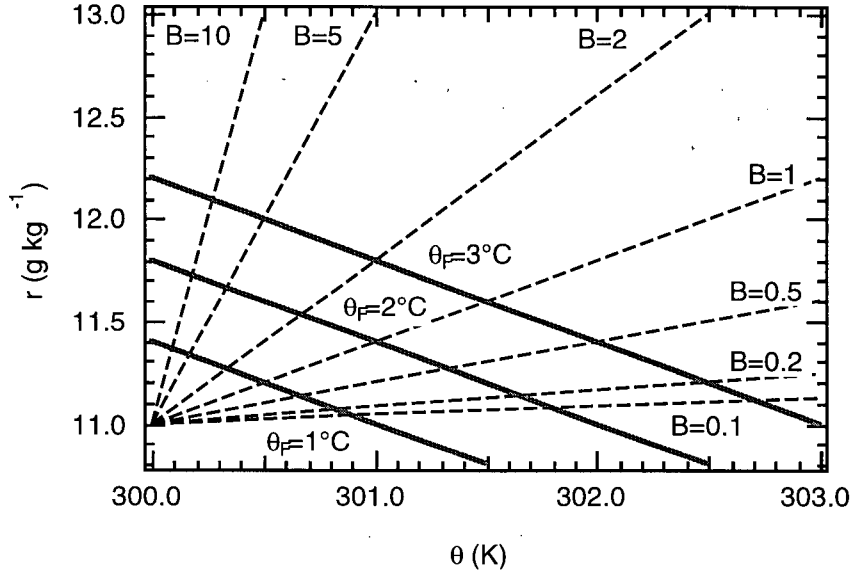


Figure C.1. After Schrieber et al. (1996), showing B (dashed lines) and θ_F (solid lines) axes for a range of B and θ_F for a reference state defined as $\theta = 300$ K and $r = 11$ g kg⁻¹.

Closer inspection of their (18a) gives some insight into this problem. This equation gives

γ_B

$$\gamma_B = \gamma_{\theta_F} \left\{ 1 - \frac{2 \left[\overline{\gamma_{\theta_F}^2 r''^2} - 2 \overline{\gamma_{\theta_F} r'' \theta''} + \overline{\theta''^2} \right]}{\left[2 \overline{\gamma_{\theta_F}^2 r''^2} - 3 \overline{\gamma_{\theta_F} r'' \theta''} + \overline{\theta''^2} \right]} \right\}, \quad (C5)$$

where θ'' and r'' are the temperature and humidity deviations from the mean. Equation (C5) shows that γ_B would have the same sign as γ_{θ_F} as long as the difference in the curly brackets is positive. For this to be the case

$$\frac{2 \left[\overline{\gamma_{\theta_F}^2 r''^2} - 2 \overline{\gamma_{\theta_F} r'' \theta''} + \overline{\theta''^2} \right]}{\left[2 \overline{\gamma_{\theta_F}^2 r''^2} - 3 \overline{\gamma_{\theta_F} r'' \theta''} + \overline{\theta''^2} \right]} < 1. \quad (C6)$$

The inequality (C6) can be solved, revealing the necessary condition for the slopes to have the same sign

$$\overline{\theta''^2} < \overline{\gamma_{\theta_F} r'' \theta''}. \quad (C7)$$

The value of $\overline{\theta''^2}$ is positive by definition. The value of $\overline{r'' \theta''}$ can be positive or negative. Equation (C4) indicates that γ_{θ_F} can only be negative (and is nearly constant), while the fits

determined from the maximum-likelihood method often yields a positive value of γ_{θ_F} which varies greatly from leg to leg. These large positive values of γ_{θ_F} mean that (C7) is likely to be true. For the BLX96 data, and the HAPEX data, the inequality (C7) is true, so that the two predicted slopes have the same sign.

Appendix D: Integration of c vs. m distributions in θ vs. r space

Schrieber et al. (1996) suggested a method of transforming a distribution of two variables into a new coordinate space. Values of θ and r can be converted to c and m , the coordinates in this new space, using (5.10), which is repeated here for clarity

$$c = \gamma_{ez} \frac{\theta - \gamma_{sfc} r}{\gamma_{ez} - \gamma_{sfc}}, \text{ and } m = \frac{\theta - \gamma_{ez} r}{\gamma_{sfc} - \gamma_{ez}}, \quad (\text{D1})$$

where γ_{sfc} is the slope of the line passing through the mean of the JFD and surface properties, and γ_{ez} is the slope of the line passing through the mean of the JFD and entrainment-zone properties. The values of c and m are projections of locations on the surface and entrainment-zone properties axes onto the original axes (Figure D.1). Hence, both c and m have physical units. A time series of θ and r can be converted to c and m using (D1) and a new Gaussian JFD can be calculated

$$G(m, c) = \frac{1}{2\pi\sigma_m\sigma_c} \exp\left\{-\frac{1}{2}\left[\left(\frac{m}{\sigma_m}\right)^2 + \left(\frac{c}{\sigma_c}\right)^2\right]\right\}, \quad (\text{D2})$$

where σ_m and σ_c are the converted standard deviations. However, a JFD in c and m space is difficult to compare directly to a JFD in θ and r because the transform (D1) is not area conserving. In other words, if a JFD defined by (D2) is plotted in θ vs. r space, using the inverse of (D1), the normalization factor in (D2), $1/(2\pi\sigma_m\sigma_c)$, must be modified. This is highlighted in Figure D.2, where we see how an arbitrary area in θ vs. r space is mapped into c vs. m space.

This new normalization factor can be derived. The first step is to find the length of each side of an arbitrary grid box in c and m space

$$\begin{aligned} \lambda_{top} &= \left[(m_1 - m_2)^2 + (c_1 - c_2)^2 \right]^{1/2} \\ \lambda_{side} &= \left[(m_1 - m_4)^2 + (c_1 - c_4)^2 \right]^{1/2}, \end{aligned} \quad (\text{D3})$$

where λ_{top} and λ_{side} are the length of the top and side the parallelogram in c vs. m space. For the case where surface and entrainment zone axes are orthogonal the area transformation is simply

$$\lambda_{top}\lambda_{side}. \quad (\text{D4})$$

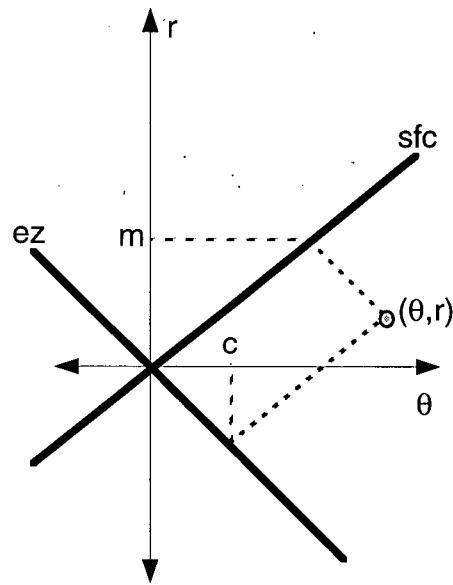


Figure D.1. Sketch showing the coordinate transform (D1) converting a point (θ, r) to (c, m) . The heavy solid lines are the surface (sfc) and entrainment zone (ez) axes.

Special consideration is needed for the case where the surface and entrainment-zone axes are not orthogonal. In this case (D4) does not give the correct correction. We will adjust the value of λ_{side} to account for this. The key variable in this case is the distance between the top and bottom of the parallelogram. The point (c_1, m_1) will be used as a reference point, and the location of a point on the bottom of the parallelogram that lies on a line through (c_1, m_1) and is perpendicular to the bottom will be found. This point will be called (c_p, m_p) . Two new quantities are needed to find this point, one is the slope of the line perpendicular to the bottom of the parallelogram, which is defined as

$$\frac{c_1 - c_p}{m_1 - m_p} = - \left(\frac{m_4 - m_3}{c_4 - c_3} \right) F, \quad (D5)$$

where F is a correction factor equal to $1 \text{ K}^2 (\text{g kg}^{-1})^{-2}$ that corrects the units. For convenience we can define the term in brackets to be A . The other is the slope of bottom of the parallelogram, which can be written as

$$\frac{c_4 - c_p}{m_4 - m_p} = \frac{c_4 - c_3}{m_4 - m_3}. \quad (D6)$$

We can solve (D6) for m_p

$$m_p = m_4 - A(c_4 - c_p). \quad (D7)$$

This result can be used in (D5) to find the location of the desired point, c_p

$$c_p = \frac{c_1 + AF(m_1 - m_4) + A^2Fc_4}{A^2F + 1} \quad (D8)$$

The results from (D8) can be used in (D6) to find the value of m_p . Given the values of c_p and m_p , the value for λ_{perp} [the length of a line through the points (c_1, m_1) and (c_p, m_p)] can be found

$$\lambda_{perp} = \left[(m_1 - m_p)^2 + (c_1 - c_p)^2 \right]^{1/2} \quad (D9)$$

The arbitrary area, in c vs. m space, is simply $\lambda_{top}\lambda_{perp}$ and the distribution can be defined as

$$G(m, c) = \frac{\lambda_{top}\lambda_{perp}}{2\pi\sigma_m\sigma_c} \exp\left\{-\frac{1}{2}\left[\left(\frac{m}{\sigma_m}\right)^2 + \left(\frac{c}{\sigma_c}\right)^2\right]\right\}, \quad (D10)$$

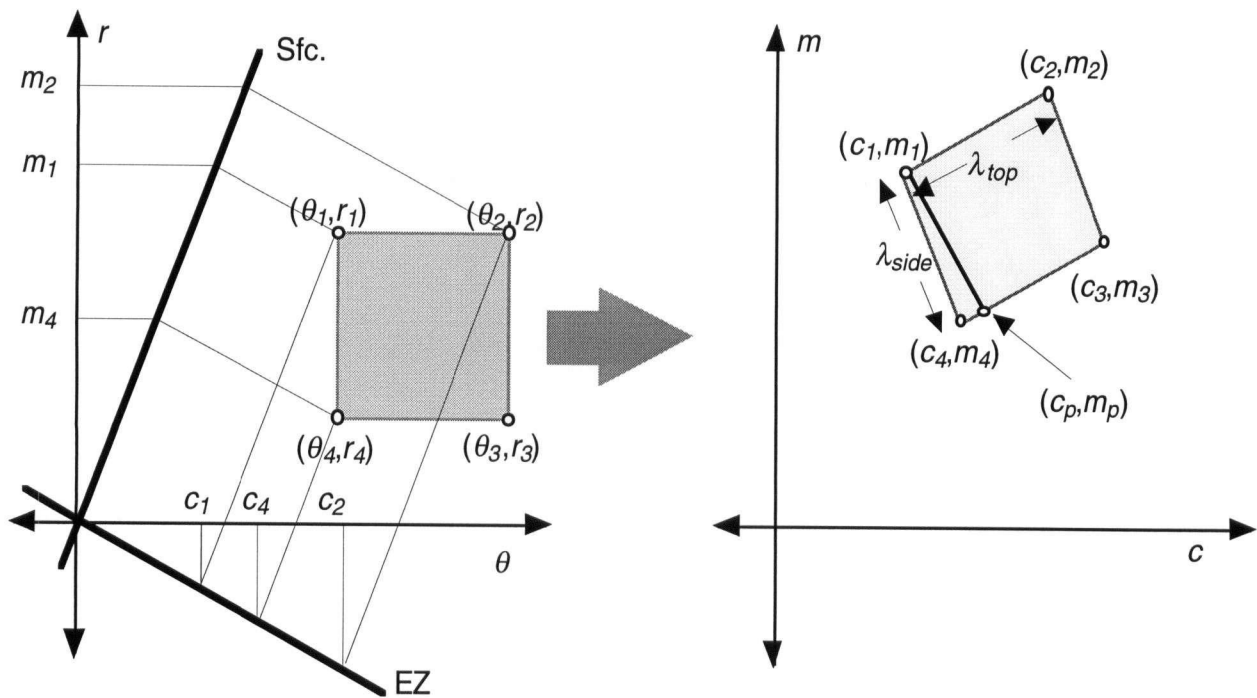


Figure D2. Sketch showing some arbitrary shaded area in θ vs. r space, indicated by the points (θ_1, r_1) , (θ_2, r_2) , (θ_3, r_3) and (θ_4, r_4) . The transform (D1) is applied and the area is defined by the coordinates (c_1, m_1) , (c_2, m_2) , (c_3, m_3) , and (c_4, m_4) . The point (c_p, m_p) represents the point where a line through (c_1, m_1) and perpendicular to the bottom of the parallelogram intercepts the bottom.

Appendix E: Correlation introduced by coordinate transformation

In chapter 5 a coordinate transformation was introduced to help explain the tilt of the JFDs in θ vs. r space. The coordinate transformation defined by (5.11) was

$$c = \gamma_{ez} \frac{\theta - \gamma_{sfc} r}{\gamma_{ez} - \gamma_{sfc}} \text{ and } m = \frac{\theta - \gamma_{ez} r}{\gamma_{sfc} - \gamma_{ez}}, \quad (5.11)$$

where γ_{sfc} is the slope of the surface axis, γ_{ez} is the slope of the entrainment zone axis, c has units of temperature and is a projection of the point onto the θ axis, and m has units of mixing ratio and is the projection of the point onto the r axis (see Figure D.1).

It seems that the JFDs, when converted into c and m space have a higher correlation than they did in θ vs. r space. The correlation between c and m can be defined as

$$\rho_{c,m} = \frac{\sum_{i=0}^N c_i m_i}{\left(\sqrt{\sum_{i=0}^N c_i^2} \sqrt{\sum_{i=0}^N m_i^2} \right)}, \quad (E1)$$

where N is the total number of observations. Equation (5.11) can be used to convert the numerator of (E1) to be a function of θ , r and the slopes

$$\rho_{c,m} = \frac{\sum_{i=0}^N \left(\frac{\gamma_{ez}}{\gamma_{ez} - \gamma_{sfc}} \right) (\theta_i - \gamma_{sfc} r_i) \left(\frac{1}{\gamma_{sfc} - \gamma_{ez}} \right) (\theta_i - \gamma_{ez} r_i)}{\left(\sqrt{\sum_{i=0}^N c_i^2} \sqrt{\sum_{i=0}^N m_i^2} \right)}. \quad (E2)$$

Simplification of (E2) yields

$$\rho_{c,m} = \frac{\left(\frac{\gamma_{ez}}{\gamma_{sfc} - \gamma_{ez}} \right) \left(\frac{1}{\gamma_{sfc} - \gamma_{ez}} \right) \sum_{i=0}^N (\theta_i - \gamma_{ez} r_i) (\theta_i - \gamma_{sfc} r_i)}{\left(\sqrt{\sum_{i=0}^N c_i^2} \sqrt{\sum_{i=0}^N m_i^2} \right)}. \quad (E3)$$

Further simplification yields

$$\rho_{c,m} = \frac{\left(\frac{\gamma_{ez}}{\gamma_{sfc} - \gamma_{ez}} \right) \left(\frac{1}{\gamma_{sfc} - \gamma_{ez}} \right) \sum_{i=0}^N \theta_i^2 - (\gamma_{ez} + \gamma_{sfc}) \sum_{i=0}^N r_i \theta_i + \gamma_{sfc} \gamma_{ez} \sum_{i=0}^N r_i^2}{\left(\sqrt{\sum_{i=0}^N c_i^2} \sqrt{\sum_{i=0}^N m_i^2} \right)}. \quad (E4)$$

Equation (E4) can be multiplied by the factor $(1/N)/(1/N)$ so the the sums can be converted to the variance or covariance of the variables.

$$\rho_{c,m} = \left(\frac{\gamma_{ez}}{\gamma_{sfc} - \gamma_{ez}} \right) \left(\frac{1}{\gamma_{sfc} - \gamma_{ez}} \right) \frac{\sigma_{\theta}^2 - (\gamma_{ez} + \gamma_{sfc}) \overline{\theta r} + \gamma_{sfc} \gamma_{ez} \sigma_r^2}{\sigma_c \sigma_m}, \quad (\text{E5})$$

Equation (E5) allows us to compare the contribution to the correlation of the covariance of θ and r in the c vs. m coordinate space [the middle term in (E5)] the contribution due only to the tilting [the first and last terms of (E5)].

Appendix F: BLX96 Cloud Field Statistics

Table F1. Observed date, time, solar zenith angle, cloud base height, cloud top height, and boundary-layer cloud type (either Cu humilis¹ or Cu mediocris) for all BLX96 cloudy days.

Date	Leg	Time (LST)	Time (UTC)	Solar Zenith Angle (°)	Cloud Base Height (m)	Cloud Top Height (m)	Boundary-Layer Cloud Type
15-Jul	1	10.2	16.2	32.7	1550	1830	Cu humilis
	2	11.4	17.4	20.7	1650	2340	Cu humilis
	3	11.6	17.6	18.7	1680	2450	Cu med./Cu hum.
	4	11.9	17.9	17.0	1700	2570	Cu med./Cu hum.
	5	13.2	19.2	18.2	1872	2700	Cu humilis
	6	13.4	19.4	20.1	1910	2730	Cu humilis
	7	13.7	19.7	22.3	1940	2760	Cu humilis
16-Jul	1	10.8	16.8	26.2	970	1626	Cu humilis
	2	11.9	17.9	15.5	1140	2040	Cu humilis
	3	12.2	18.2	14.5	1180	2120	Cu humilis
	4	12.4	18.4	14.1	1210	2210	Cu humilis
	5	13.7	19.7	21.2	1200	1930	Cu humilis
	6	13.9	19.9	23.7	1190	1870	Cu humilis
	7	14.1	20.1	26.1	1190	1820	Cu humilis
23-Jul	1	11.8	17.8	19.1	800	1200	Cu humilis
	2	12.9	18.9	17.0	800	1080	Cu humilis
	3	14.1	20.1	26.1	1350	1580	Cu humilis
	4	14.3	20.3	28.9	1470	1680	Cu humilis
	5	14.6	20.6	31.9	1590	1800	Cu humilis

¹Cumulus humilis are clouds where the diameter is more than twice the cloud depth

Table F1 continued.

Date	Leg	Time (LST)	Time (UTC)	Solar Zenith Angle (°)	Cloud Base Height (m)	Cloud Top Height (m)	Boundary-Layer Cloud Type
25-Jul	1	11.1	17.1	24.7	1730	1970	Cu humilis
	2	12.3	18.3	17.4	2250	2590	Cu humilis
	3	12.6	18.6	17.4	2360	2720	Cu humilis
	4	12.8	18.8	18.1	2470	2840	Cu humilis
	5	14.1	20.1	27.8	2440	2660	Cu humilis
	6	14.3	20.3	30.4	2440	2630	Cu humilis
	7	14.6	20.6	33.3	2430	2590	Cu humilis
27-Jul	1	11.0	17.0	26.6	550	700	Cu humilis
	2	12.2	18.2	17.8	770	930	Cu med./Cu hum.
	3	12.5	18.5	17.3	820	990	Cu humilis
	4	12.7	18.7	17.4	870	1040	Cu med./Cu hum.
	5	13.9	19.9	25.3	940	1130	Cu humilis
	6	14.2	20.2	28.0	960	1150	Cu humilis
	7	14.5	20.5	31.0	980	1170	Cu humilis
28-Jul	1	11.3	17.3	22.1	940	1560	Cu med./Cu hum.
	2	12.5	18.5	16.5	1160	1780	Cu med./Cu hum.
	3	12.8	18.8	17.2	1220	1840	Cu med./Cu hum.
	4	13.1	19.1	18.6	1270	1890	Cu med./Cu hum.
	5	14.3	20.3	29.8	1310	1600	Cu med./Cu hum.
	6	14.6	20.6	33.1	1310	1530	Cu humilis
	7	14.9	20.9	36.3	1320	1470	Cu humilis

Table F1 continued.

Date	Leg	Time (LST)	Time (UTC)	Solar Zenith Angle (°)	Cloud Base Height (m)	Cloud Top Height (m)	Boundary-Layer Cloud Type
31-Jul	1	11.2	17.2	24.6	1540	1630	Cu humilis
	2	12.4	18.4	18.7	1720	1990	Cu humilis
	3	12.7	18.7	19.1	1760	2080	Cu humilis
	4	13.0	19.0	20.2	1800	2160	Cu humilis
	5	14.2	20.2	29.6	1940	2440	Cu humilis
	6	14.5	20.5	32.6	1970	2500	Cu humilis
	7	14.7	20.7	35.6	2000	2570	Cu humilis
2-Aug	1	11.0	17.0	26.1	840	1000	Cu humilis
	2	12.2	18.2	18.0	920	1230	Cu humilis
	3	12.5	18.5	17.7	940	1280	Cu humilis
	4	12.7	18.7	18.1	960	1340	Cu humilis
	5	14.0	20.0	26.7	1050	1310	Cu humilis
	6	14.2	20.2	29.5	1070	1300	Cu humilis
	7	14.5	20.5	32.7	1090	1290	Cu humilis

Appendix G: Conditions used for BOMEX case

Holland and Rasmusson (1973) and Nitta and Esbensen (1974) have conducted a large scale budget study for phase 3 of the Barbados Oceanographic and Meteorological Experiment (BOMEX) (22 June to 30 June 1969) over the ocean at 15°W lat and 55°N long. From 22 to 26 June the area was covered with non-precipitating cumuli. For this case mean profiles from ship R.V. Oceanographer is used (table G1). Pressure as a function of height was found using an iterative procedure based on the hypsometric equation.

$$\Delta z = \frac{R_d \bar{T}_v}{g} \ln \left(\frac{p_1}{p_2} \right), \quad (\text{G1})$$

where R_d is the gas constant for dry air, g is the acceleration due to gravity, \bar{T}_v is the layer average virtual temperature, p_2 is the pressure at the top of the layer, and p_1 is the pressure at the bottom of the layer. The reported profile used in this study was for θ_v not T_v , but they are related by $\theta_v = T_v (p_o/p)^{R_d/C_p}$ where C_p is the specific heat of air. These two equations can be combined to give

$$p_2 = p_1 \exp \left[- \frac{g \Delta z}{R_d \bar{\theta}_v} \left(\frac{2p_o}{p_1 + p_2} \right)^{-R_d/C_p} \right]. \quad (\text{G2})$$

Equation (G2) converges in about 5 iterations. From (G2) and the observed surface pressure of 101.5 kPa, the pressure profile can be determined.

Other key variables are listed in Table G2. Surface fluxes were measured near the BOMEX ship. Entrainment-zone fluxes were obtained from the GCSS LES model intercomparison (Siebesma et al. 2001). The value of r_* was defined using the methods suggested in Chapter 3.

Table G1. Mean environment profiles of p , θ_v and r .

z (km)	p (kPa)	θ_v (K)	r (g kg ⁻¹)
0.0	101.5	301.9	17.3
0.52	95.72553491	301.7	16.6
1.48	84.79807592	304.4	10.8
2.00	79.72985103	309.0	4.2
3.00	71.80892125	312.4	3.0
4.00	64.19105184	315.8	1.8
5.00	57.30428087	319.3	0.6

Table G2. Miscellaneous values used for the CuP simulation the BOMEX case. A subscript sfc indicates a surface value, a subscript ez indicates an entrainment zone value.

Variable	Value
z_i	520 m
$\overline{w\theta}_{sfc}$	8×10^{-3} K m s ⁻¹
$\overline{w\theta}_{ez}$	-1.6×10^{-3} K m s ⁻¹
\overline{wr}_{sfc}	5.2×10^{-2} g kg ⁻¹ m s ⁻¹
\overline{wr}_{ez}	4.2×10^{-2} g kg ⁻¹ m s ⁻¹
$\overline{w\theta_v}_{sfc}$	1.8×10^{-2} K m s ⁻¹
w_*	0.67 m s ⁻¹
θ_*	0.012 K
r_*	0.070 g kg ⁻¹
t_*	780 s